이학박사 학위논문

Artificial Nanoparticle–Polymer Superlattices

나노입자와 고분자로 구성된 인공 초격자에 대한 연구

2016 년 8 월

서울대학교 대학원

화학부 고분자화학전공

후스만 한나

Abstract

Artificial Nanoparticle-Polymer Superlattices

Hannah Huesmann
Polymer Chemistry, Department of Chemistry
The Graduate School
Seoul National University

Hybrid superlattices (SLs) consisting of soft polymers with low refractive index polymers and hard oxide nanoparticles with high refractive are highly suitable materials for the application in 1D phononic and photonic crystals.
In this theses the synthesis of titania and barium titanate nanospheres as building blocks for such SLs is described, including the influence of solvents and ligands on the particles synthesis. In the case of titania nanoparticles the morphology could be changed from spheres to cubes and the assembly of these nanocubes into mesocrystals is presented. In the case of barium titanate the addition of different amounts of ligand into the reaction mixture, to control the morphology, is investigated and first experiments on the assembly of ferroelectric barium titanate rods in an electric field are conducted.
Further different SLs are built-up and characterized using scanning electron microscopy, UV-Vis- and Brillouin spectroscopy to monitor the morphology, to identify the photonic band gaps and to invest the phonon propagation respectively. In this work, the focus is set on the fabrication of the SLs using the facile method of spin coating. Special emphasis was put on the conditions needed to obtain highly homogenous multilayered SLs in the nanometer range from poly(methyl methacrylate) (PMMA) as soft low refractive index materials, and titania, barium titanate and silica nanoparticles as hard, high refractive index materials. Beside simple $(AB)_n$ structured SLs, with A being PMMA and B being oxide nanoparticles, more complex structured SLs are invested. For example a tandem SL built-up from two different $(AB)_n$-type

lattices and SLs with a higher periodicity like $(ABAC)_n$-type SLs were built-up and characterized. Further the difficulties of spin coating a SL containing colloidal particles as a defect layer in an $(AB)_n$-type SLs and the influence on the phononic band structure is discussed. Finally the substitution of PMMA through stimuli responsive poly(2-vinyl pyridine) (P2VP) was examined and preliminary experiment on the swelling behaviour of P2VP as a layer material showed the potential of P2VP to built water vapour responsive photonic crystals.

The studies conducted in this work help to offer the fundamental knowledge about the propagation of photon and phonon within 1D SLs, focusing on the synthesis of building blocks and the fabrication of SLs. It is expected that this understanding will enormously contribute to the development of acoustic diodes and heat flownmanaging devices in the future.

Keywords : photonic, phononic, superlattices, nanoparticles, polymer, spin coating

Student Number : 2014-30843

Zusammenfassung

Die aus weichen Polymeren mit niedrigem Brechungsindex und aus harten, oxidischen Nanopartikeln mit einem hohem Brechungsindex aufgebauten Hybridübergitter sind vielversprechende Materialien, um eindimensionale photonische und phononische Kristalle aufzubauen.

In dieser Arbeit wird die Synthese von Titandioxid- und Bariumtitanat-Nanopartikeln beschrieben, welche als Bausteine für die Übergitter verwendet werden. Es wird der Einfluss von Lösemitteln und Liganden auf die verschiedenen Synthesen untersucht. Hierbei wird gezeigt, dass die Morphologie der Titandioxid-Nanopartikel von sphärischer bis hin zu würfelartigiger Form geändert werden kann und dass diese Nanowürfel zu Mesokristallen angeordnet werden können. Es wird der Einfluss verschiedener Liganden auf die Synthese der Bariumtitanat-Nanopartikel untersucht, um die Morphologie der Nanopartikel zu beeinflussen. Des Weiteren werden erste Versuche zur Ausrichtung der ferroelektrischen Bariumtitanat-Nanostäbchen im elektrischen Feld beschrieben.

Außerdem werden verschiedene Übergitter aufgebaut und mit Hilfe von Rasterelektronenmikroskopie, UV-Vis- und Brillouin-Spektroskopie werden die Morphologie, die optische Bandlücke und die Phononenleitung in den Übergittern bestimmt. In dieser Arbeit wird der Fokus auf den Aufbau der Übergitter mittels Rotationsbeschichtung gelegt. Es werden die genauen Bedingungen erforscht, um homogene Multischichten aus dem weichen Poly(methylmethacrylat) (PMMA) mit niedrigem Brechungsindex und dem harten Silicium-, Titandioxid und Bariumtitanat mit hohem Brechungsindex im Nanometer Masstab aufzubauen. Neben einfachen Übergittern mit einer $(AB)_n$ Struktur werden auch komplexere Gitter untersucht. So wird zum Beispiel ein sogenanntes Tandem-Gitter, bestehend aus zwei verschiedenen $(AB)_n$-Gittern und verschiedene Gitter mit einer $(ABAC)_n$-Periodizität aufgebaut und charakterisiert. Darüber hinaus werden auch die Schwierigkeiten diskutiert, die mit dem Einbringen kolloidaler Partikel in ein (AB)n-Gittern einhergehen. Abschließend wird die Substitution von PMMA durch das responsive Poly(2-vinylpyridin) (P2VP) beschrieben und erste Versuche zum Schwellverhalten des P2VPs werden durchgeführt. Zusätzlich

wird die Möglichkeit aufzeigt, mit Hilfe von P2VP in Wasserdampf responsive Photonischen Kristallen aufzubauen.

Mit dieser Forschungsarbeit wird dazu beigetragen, die Grundlangen der Photonenund Phononenleitung in eindimensionalen Übergittern zu verstehen, wobei der Fokus auf der Synthese der Bausteine für die Übergitter sowie dem Aufbau der Übergitter liegt. Das bessere Verständnis der Photonen- und Phononenleitung ebnet den Weg für die Entwicklung akustischer Dioden und Materialien zur Kontrolle des Wärmeflusses.

Abstract (in Korean)

나노입자와 고분자로 구성된 인공 초격자에 대한 연구

후스만 한나
화학부 고분자 전공
서울대학교 대학원

낮은 굴절률을 가진 연성의 고분자와 높은 굴절률을 가진 강성의 산화물 나노입자들로 구성된 복합 초격자(superlattice)는 1차원 포논 결정(phononic crystal) 및 광결정(photonic crystal) 응용에 매우 적합한 물질이다.

본 논문에서는 구형의 TiO_2와 $BaTiO_3$ 나노입자 및 이들로 구성된 초격자를 제조하는 연구를 다루었으며 입자 제조시 용매와 리간드가 끼치는 영향도 함께 기술하였다. TiO_2 나노입자의 경우 구형으로부터 육면체형으로 모양을 변화시킬 수 있으며, 이렇게 바뀐 형태를 가지는 나노입자가 서로 모여 중간 결정(mesocrystal)을 형성하는 것을 확인하였다. $BaTiO_3$의 경우 입자의 형태를 제어하기 위해 반응 혼합물에 서로 다른 양의 리간드를 첨가하였고, 전기장 안에서 조립되는 강유전성(ferroelectric) $BaTiO_3$ 막대들에 대해 처음으로 연구하였다.

또한 서로 다른 초격자를 제조하고 이들의 구조, 광 밴드갭, 포논 전파를 각각 주사전자현미경(SEM), 자외선-가시광선 분광법, 브릴루앙(Brillouin) 분광법을 통해 측정하였다. 본 연구에서는 특별히 손쉽게 초격자를 제조하기 위해 스핀 코팅을 이용하였다. 특히 낮은 굴절률의 연성 물질로서 poly(methyl methacrylate) (PMMA)와 높은 굴절률의 강성 물질로서 TiO_2, $BaTiO_3$, 및 SiO_2 나노입자를 활용하여 나노미터 수준에서 매우 균일한 다층 초격자를 제조하기 위한 조건을 중점적으로 탐구하였다. 또한 A를 PMMA, B를 산화물 나노입자라고 했을 때, 단순한 $(AB)_n$ 형태의 구조뿐만 아니라 더욱 복잡한 구조를 가지는 초격자도 제조하였다. 예를 들어 서로 다른 $(AB)_n$ 형태의 초격자들을 적층하여 탠덤(tandem) 초격자를 만들었으며, 보다 더 큰 주기를 가지는 $(ABAC)_n$ 형태의 초격자

역시 제조하여 그 특성을 분석하였다. 그리고 콜로이드 입자는 스핀 코팅으로 격자층을 만들기 어렵기 때문에 $(AB)_n$ 형태의 초격자 내에서 결함층(defect layer)으로 작용하는 것을 확인하였고, 이들이 포논 밴드 구조에 끼치는 영향에 대해서도 고찰하였다. 마지막으로 PMMA 대신 자극 감응성이 있는 poly(2-vinyl pyridine) (P2VP)를 활용하여 초격자를 제조하였고, 층상 구조를 형성하는 P2VP의 팽윤 현상에 대한 실험을 토대로 수증기에 감응하는 광 결정 제조에 P2VP가 활용될 수 있는지 가능성을 확인하였다.

본 연구는 초격자를 구성하는 재료의 합성과 초격자의 제조에 중점을 두었으며, 1차원 초격자 내에서 광자 및 포논의 전파에 관한 기초적인 이해를 제공해 주었다. 이러한 이해는 향후 음향 다이오드의 개발 및 소자 내 열 전달 관리 응용에 크게 기여할 것으로 기대된다.

주요어: 광자성(photonic), 포논성(phononic), 초격자, 나노입자, 고분자, 스핀 코팅

학번: 2014-30843

to my family

Contents

I Introduction **1**

1 Photonic Superlattices **3**

2 Phononic Superlattices **7**

3 Pho(X)onic Superlattices **11**

4 Aims and Objectives **13**

II Building Blocks **15**

5 Synthesis and Application of TiO_2 Nanoparticles **17**
5.1 Abstract 17
5.2 Introduction 17
5.3 Results and Discussion 19
5.4 Experimental Section 27
5.5 Supporting Information 28

6 Synthesis and Application of $BaTiO_3$ Nanoparticles **33**
6.1 Introduction 33
6.2 Typical Synthesis of Barium Titanate Nanospheres 34
6.3 Barium Titanate Nanorods: Synthesis and Orientation in an Electric Field 36
6.4 Summary and Outlook 40
6.5 Experimental Details 41

III Superlattices **43**

7 Fabrication Method of the Superlattices **45**
7.1 Spin Coating Technique 45
7.2 Spin Coating Solutions 47

8 Characterisation **51**
8.1 Optical Characterisation 51
8.2 Mechanical Characterisation 51
8.3 Structure of the Samples 54

9 Pho(X)onic Superlattice **57**
9.1 Abstract 57
9.2 Introduction 57
9.3 Results and Discussion 59
9.4 Conclusion 66
9.5 Materials and Methods 68
9.6 Additional Comments 70

10 PMMA-$BaTiO_3$ Superlattices **73**
10.1 Introduction 73
10.2 Results and Discussion 73
10.3 Summary and Outlook 80
10.4 Experimental Details 80

11 A Tandem Superlattice **81**
11.1 Introduction 81
11.2 Results and Discussion 82
11.3 Summary 86
11.4 Experimental Details 87

12 Superlattices with an $(ABAC)_n$ Periodicity **89**
12.1 Introduction 89
12.2 Results and Discussion 90
12.3 Summary 95
12.4 Experimental Details 95

13 Superlattice with a $cSiO_2$ Defect Layer **97**
13.1 Introduction 97
13.2 Results and Discussion 98
13.3 Summary and Outlook 102
13.4 Experimental Details 103

14 Responsive Layers **105**
14.1 Introduction 105
14.2 Preliminary Experiments 106
14.3 Summary and Outlook 111
14.4 Experimental Details 112

IV Summary & Outlook 113

15 Summary 115

16 Outlook 117

Bibliography 119

List of Figures 132

List of Tables 133

List of acronyms 135

17 Acknowledgement 137

Part I

Introduction

1 Photonic Superlattices

When light interacts with materials there are different kind of interactions depending on the nature of the material. If light hits onto a simple non transparent solids it gets reflected. But if light hits onto a partial transparent materials it gets partial reflected and partial refracted, the refraction depends on the internal properties of the material (dielectric constant or refractive index). If we go one step further and observe the interaction between light and a periodically structured material, which is composed of two partial transparent materials with different dielectric constants, we observe multiple reflection and multiple refraction at the interface between the two building materials. These multiple reflection and refraction yield in an interference of the light and therefore a interference pattern is formed. The last mentioned materials are called photonic crystals (PtC), which are widely spread in nature as well as in technology. They are periodically structured materials from high and low refractive index materials and the periodical structuring can take place in one, two or three dimensions (see figure 1.1).

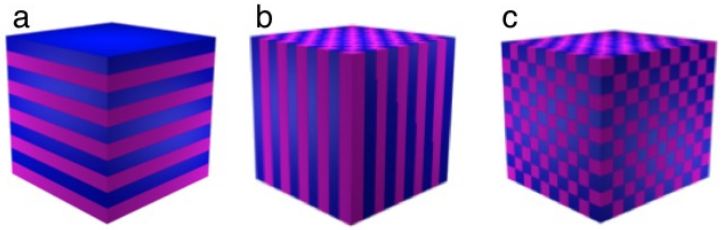

Fig. 1.1: Schematic illustration of a one (a), two (b) and thee (c) dimensional photonic crystals.

With PtC it is possible to control the flow of light depending on their periodicity in one, two or three dimensions. One dimensional PtC are built from planar layers of alternating high and low refractive index materials. One very prominent example is the male species of the *Moroho menelaus* butterflies[1]. An image of the butterfly and its structured wing is shown in figure 1.2. The bright blue colour is caused by a one dimensional structure of alternating layers of cuticule lamellae (high refractive index) and air (low refractive index).

Nature does not only give us examples of one dimensional PtCs but also for two and three dimensional ones. One example for a two dimensional PtCs is present in the Marine poychaete worm *Aphrodita* and *Pherusa,Vukusic2003a* a three dimensional PtCs is located in the S-iridophores of panther chameleons[2].

The PtCs in the marine poychaete worms are built from 2D hexagonal lattice of voids, which forms pseudo-PtC fibres. An image of the worm is shown in figure

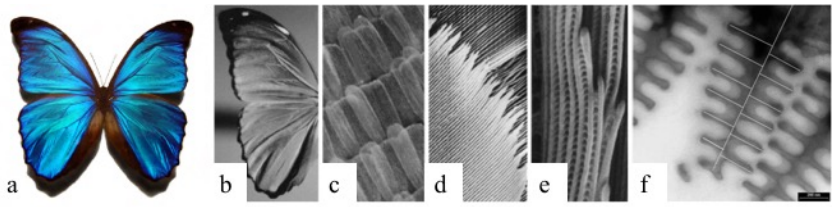

Fig. 1.2: a) And b) photos of the male *Morpho menelaus* butterfly. c) A microscope image of its wing. d) SEM image of an iridescent ground scale. e) Lateral SEM image of a ridge. e) TEM image of the cross section through a *M. Menelaus* iridescent scale.[1]

1.3a). In figure 1.3b a SEM and in figure c)-e) TEM images of the the hexagonal photonic patterning of the worms seta is presented.

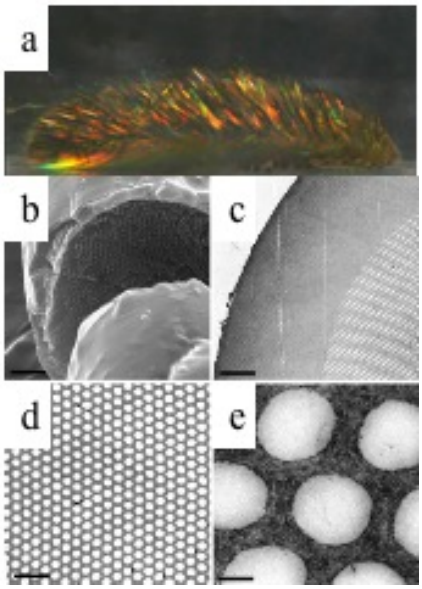

Fig. 1.3: a) Photo of a Marine poychaete worm *Aphrodita*. b) SEM image of setae of the polychaete worm, scale bar 2 µm. c)-e) TEM image of the transverse section though a seta, scale bars: c) 5 µm, d) 1 µm, e) 120 nm.[3]

Recently Theyssier *et al.* published a paper explaining the change of the colours in the male panther chameleons when it goes from its relaxed state (green) to its excited state (yellow/orange).[2] An image of the chameleon is given in figure 1.4 a), on the left side the relaxed green state and right side the exited orange state of the chameleon is presented. A systematic scheme of the chameleon skin with its epidermis, and its S- and D-iridophores is shown in figure 1.4b). They could prove that the colour change is caused by a swelling and deswelling of guanine nanocrystals in the S-iridophores in the epidermis of the panther chameleon. These guanine nanocrystals, shown in figure 1.4 c), can be understood as three-dimensional PtCs. They are well arranged in a fcc packing and a swelling of these crystals causes a change of the lattice constant of the PtC and therefore the position of the photonic band gap is changed and the colour of the animal turns from green to orange.

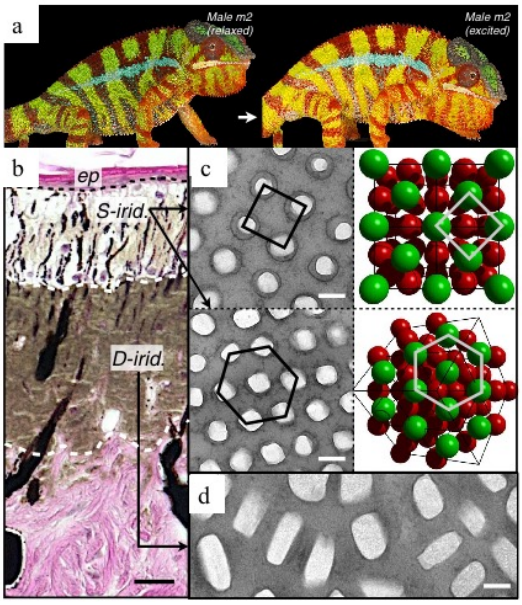

Fig. 1.4: a) Image of the male panther chameleon in its relaxed state (green) and its excited state (orange). b) Cross-sectional image of the epidermis of the chameleon; scale bar 20 µm. c) TEM image of guanine nanocrystals in S-iridophores in the excited state and three-dimensional model of an fcc lattice; scale bar 200 nm. d) TEM image of the guanine nanocrystals in D-iridophores; scale bar 200 nm.[2]

In literature there are many examples for PtC inspired by the structural colours of the nature.[4] For simplicity reasons we will focus on 1D PtC starting from here because they are easy to fabricate, simple to explain and subject of the research done within this thesis.

Researchers all over the world are interested in fabrication of 1D PtC. They can be built from purely inorganic based materials[5] or purely organic materials, mostly polymers[6], as well as from a combination of organic and inorganic materials, so called hybrid PtC[7]. While inorganic or hybrid 1D PtC are usually fabricated by spin coating alternating layers from high and low refractive index materials, polymeric based PtC are made by self-assembly of block copolymers. A very interesting example of an inorganic PtC build from only titania was published recently[8]. They create the refractive index difference by using two different shaped titania nanoparticles. One layer is made from spherical titania nanoparticles which show a low film porosity and the other layer is made from discoidal titania nanoparticles which form highly porous films. This difference in the porosity of the two layers is strong enough to show a refractive index difference between the two layers and therefore create a PtC.

As mentioned above the properties of the PtC are given by the dielectric constant or the refractive index of the materials as well as the lattice parameters of the crystal. The band gap of a photonic crystals is the frequency of the light waves which can not travel through the crystal nor can they get absorbed by the crystal building materials. Thus the position of the band gap is an important parameter for the description of an PtC.

The position of the band gap of 1D PtC can be roughly predicted by the Bragg-Snell law, which is given in equation 1.1. λ_{Max} is the central frequency of the band gap, n_L and n_H are the refractive indices of the low and high refractive index and h_L and h_H are the thickness of the low and high refractive index layers respectively. The Bragg-Snell law presumes that the incidence of the light is normal to the periodicity of the crystal and that the materials are non absorbing.

$$m\lambda_{Max} = 2(n_L \cdot h_L + n_H \cdot h_H) \tag{1.1}$$

As we can see from equation 1.1 the position of the band gap depends on the lattice parameter a ($a=h_L+h_H$) and the refractive index of the materials. To obtain crystals with a band gap in the visible wavelength range we need lattice spacings in the nanometer range.

Two other parameters which define the properties of the PtC are the bandwidth and the reflectivity. The bandwidth is given by equation 1.2:

$$\Delta\omega = \frac{4\omega_{max}}{\pi} \sin^{-1} \frac{|n_L - n_H|}{n_L + n_H} \tag{1.2}$$

With

$$\omega_{max} = \frac{2\pi c}{\lambda_{max}} \tag{1.3}$$

Equation 1.2 shows that if the mismatch between the to refractive indices is big the band gap is wide.

The reflectivity R is given by equation 1.4

$$R = [\frac{n_0 - n_S(\frac{n_L}{n_H})^{2N}}{n_0 + n_S(\frac{n_L}{n_H})^{2N}}]^2 \tag{1.4}$$

Here n_0 is the refractive index of air, n_S is the refractive index of the substrate and N is the numbers of layers in the PtC. With this three parameters we have defined the most important parameters for Bragg reflectors.

Typical application fields of PtC are optical filters[9] as well as optical fibres and waveguides. Further PtC increase the efficiency of LEDs when they are put on a LED as a surface layer[10] and boost the efficiency of lasers.[11,12]

2 Phononic Superlattices

Phononic crystals (PnC) can be understood as mechanical analogs of PtC. They are materials which can manipulate the flow of acoustic waves and similar to PtC they can be one, two or three dimensional wave guides.

PnC were predicted theoretically more than 20 years ago.[13,14] One-dimensional PnC show a periodic modulation of the elastic impedance Z (ρc_L) along the axis perpendicular to the substrate. The phonon propagation in the system can be controlled by the spatial modulation of Z with the most striking feature being the formation of unidirectional phononic band gaps.

The first experimental data of soft 1D PnC were published by Gomopoulos *et al.* in 2010.[15] They fabricated a Bragg stack from poly(methyl methacrylate) (PMMA) and silica (SiO_2) layers by sequential spin coating. Utilising the non-destructive technique of Brillouin spectroscopy, a clear phononic band gap was observed with a central frequency of 12.6 GHz. The results were supported theoretically by finite element analysis (FEA). A more detailed study of phonon propagation in Bragg Stacks was published by Schneider *et al.*[16] A SEM image of this 1D PnC is given in figure 2.1a), the lattice constant is given with 117 nm with 39 nm for the soft PMMA and 78 mm for the hard silica layer. In figure 2.1b) the phonon dispersion relation of this PnC is shown. The central frequency of the phononic band gap is at 12 GHz in the hyper sonic frequency and the width of the band gap is about 2 Hz. There are more details studies about PMMA SiO_2 super lattices, for example the influence of defect layers in the PMMA-SiO_2 SL has been investigated systematically.[17]

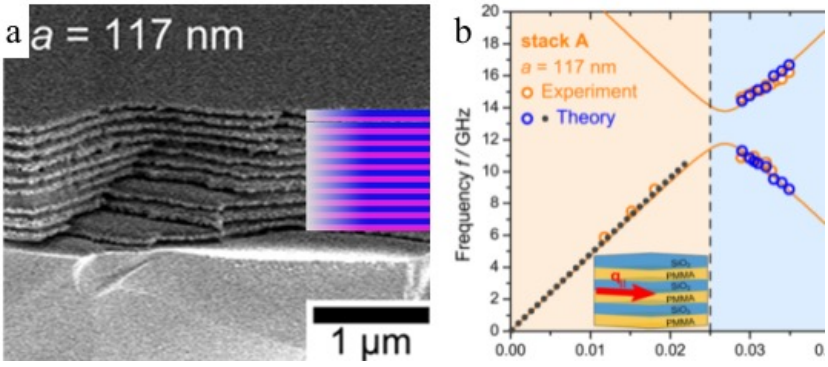

Fig. 2.1: a) SEM image of 1D PnC built from PMMA-SiO_2 SL. b) Phonon dispersion relation of that PnC.[16]

One example for a 2D PnC is the artwork of Eusebio Sempre (see figure 2.2) This artist built a kinematic sculpture from hollow stainless-steel cylinders with a diameter of 2.9 cm. They are periodically arranged on a round platform with

a diameter of 4 m with a cylinder to cylinder distance of 10 cm. His kinematic peace of art shows a Bragg attenuation peak at 1670 Hz. Martinez-Sala *et al.* could demonstrate, that this peak corresponds to the [100] destructive interference peak.[18]

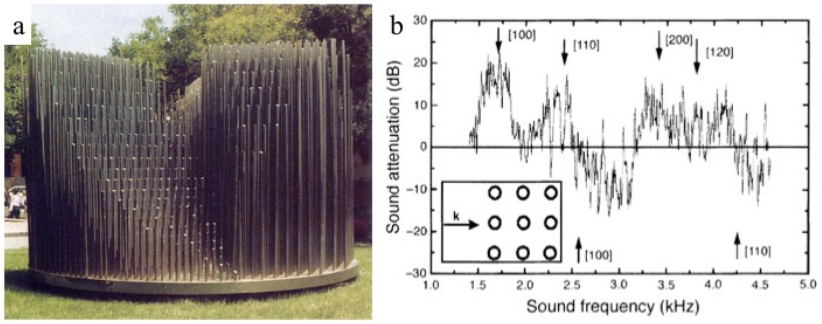

Fig. 2.2: a) Photo of the kinematic sculpture by Eusebio Sempre. b) Sound attenuation vs. sound frequency diagram of the kinematic sculpture.[18]

A very prominent example for a 3D PnC is the one published by Liu *et al.*[19] They build a cube from silicone rubber coated lead beats shown in figure 2.3. The hard core of the beats is 5 mm and the soft shell is 2.5 mm. This building blocks were then arranged in a 8x8x8 cubic crystal with a lattice constant of 1.55 cm. This three dimensional phononic structure exhibits two stop bands. The lower is located at a central frequency of 500 Hz and the higher frequency band gap is at a central frequency of 1600 Hz.[19]

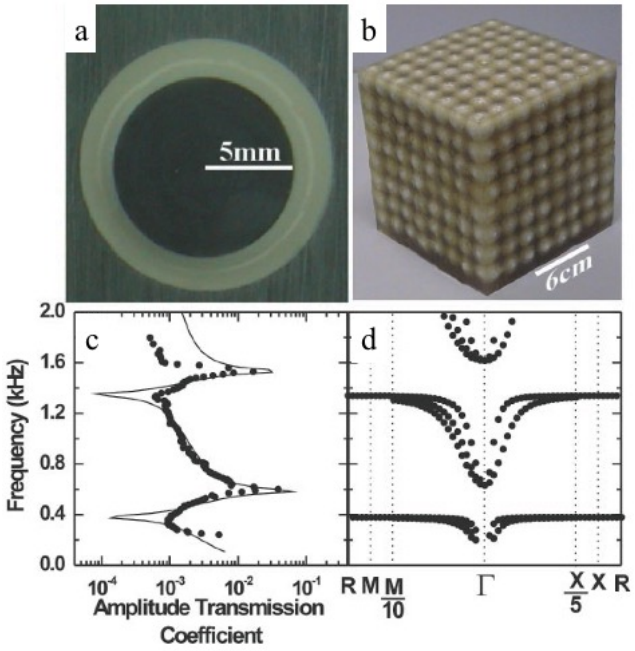

Fig. 2.3: a) Cross-sectional image of a coated lead sphere. b) Sonic crystal formed from assembly of 8x8x8 spheres. c) Calculated (solid line) and measured (circles) amplitude transmission coefficient for the PnC and d) its calculated band structure.[19]

This three examples for PnC already show, that the position of the stop band for acoustic waves can be tuned in a huge frequency range. Depending on the lattice

spacing of their periodic structures as well as on the density contrast between the two used building materials a sound wave range from the infrasonic (Hz) to the hypersonic (10^{12} GHz) can be covered. This makes PnC interesting for application in sound management as well as for thermal management application or sensors.[20]

There are many approaches to realise phononic crystals there are polymer based[20], metal based and hybrid PnC. While polymeric structures have the advantage of scalability, wide tunability, easy functionalization, mechanical flexibility, light weight, relatively low cost and good compatibility with different patterning methods they also show a natural boarder of contrast. Because they are built from organic materials where the refractive index and the elastic moduli can be varied only in a small range. Inorganic based materials have the advantage of wide density and refractive index ranges but these materials are often difficult to process, expensive and non flexible. To use organic-inorganic hybrid materials gives us the possibility to combine the easy processable and tunable polymers with high density and high refractive index inorganic nanoparticles. And therefore hybrid materials open a wide range of possible materials for designing the band structure of phononic materials while further pushing the density contrast.

Similar to photonic crystals or semi conducting crystals PnC are characterised by their band structure. While the electronic analogs are characterised by the electronic band model described through a conducting and a non conducting band in the so called band diagram, the band diagram of phononic crystals is described by their dispersion relation. The dispersion relation is a plot of the angular frequency (ω(k)) vs the wave vector (k).

Depending on the materials which the phononic crystal is made of, the band structure differs. There are mainly two parameters which can be tuned to change the band structure of phononic crystals. One is clearly the lattice spacing, which determines the wavelength of the scattered waves and therefor the wavelength region of the band gap. The angular frequency of the scattered wave is linked to the lattice spacing.

$$\omega \sim \frac{1}{\lambda} \sim \frac{1}{a} \tag{2.1}$$

With λ being the wavelength of the acoustic wave and a being the lattice parameter. The width of the band gap is mainly determined by the acoustic impedance (Z) difference of the two lattice building materials, making the impedance the second big factor that influences the band structure. The acoustic impedance is a function of the sound velocity (c) and the density of the materials (ρ).

$$Z = c\rho \tag{2.2}$$

Z determines the reflectivity (R) of acoustic waves.

$$R = (\frac{Z_2 - Z_1}{Z_2 + Z_1})^2 \tag{2.3}$$

Is the reflectivity smaller than 1 (R<1) the wave propagates through the medium. Is the reflectivity greater than or equal to 1 (R≥1) reflection of the waves accrues. And therefore the band gap opens up. The impedance is not only determined by the intrinsic material properties but by the porosity of the materials as well. This plays an important role especially in PnC built up from nanoparticle films. The packing density of the nanoparticles has a huge influence on the filling ratio of the material and therefore on the volume fraction and the acoustic impedance. In this work we focus on hypersonic PnC. That means The band gap of the presented PnC is in the gigahertz frequency range and therefore a lattice spacing in a dimension of about 100 nm. is required. The method to characterise the band structure in the giga Hertz frequency range is the Brillouin spectroscopy (see chapter Characterization 8).

Future applications for this kind of PnC could be any device where it is needed to control and guide the flow of acoustic waves. We could image sensors for acoustic waves, acoustic diodes as well as devices for heat flow management.[20]

3 Pho(X)onic Superlattices

Pho(X)sonic crystals (PXC) are crystals which can control both the flow of light and acoustic waves. They are a combination of photonic crystals and phononic crystals with the X in pho(X)onic substituting the t and the n of photonic and phononic.[20] Since PtC do not allow certain light frequencies to propagate though them (photonic band gap) the can be considered blind for these frequencies. In a similar fashion PnC block acoustic waves of certain frequencies (phononic band gap) they can therefore considered to be deaf. Pho(X)onic crystals which are defined as having both, a photonic and a phononic band gap are both, blind and deaf for defined frequencies.

So which conditions are necessary to build such structures? As mentioned in the previous chapters PtC can be built from periodic materials with a modulation of the refractive index, while PnC need a periodic modulation of the elastic moduli (or density). Therefore it seems obvious that if there are two materials with a significant refractive index contrast and at the same time a significant mismatch of their elastic moduli it is possible to design structures with a dual, photonic and phononic band gaps. There are some theoretical[21–23] as well as experimental[24,25] approaches to realize such opto-acoustic crystals.

A three dimensional crystal, with both a photonic and a phononic band gap has been reported by Akimov *et al.*[25] They described the photonic and the phononic band structure of close-packed silica spheres (d=359 ±10 nm) on a substrate. They show a photonic band gap at a central frequency of $\lambda_{max} = 765$ nm and two phononic band gaps, one from 4 to 9 GHz and the other one with a central frequency of 12 GHz.

A two dimensional opto-mechanical crystal has been designed by Safavi-Naeini an co-workers in 2010[26] and was later experimentally realised.[27] They could show in an array of snowflakes as a slap-structure (see figure 3.1) open a full phononic

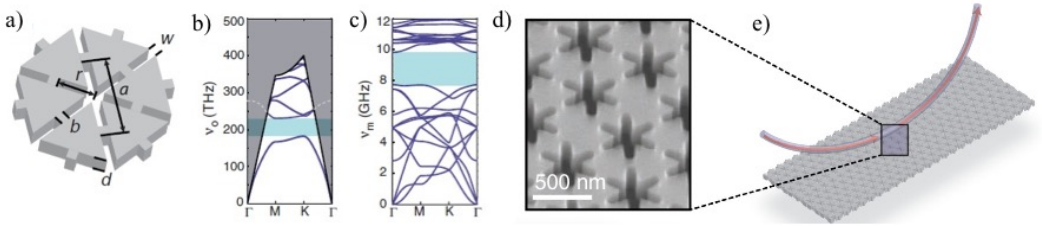

Fig. 3.1: a) Unit cell of the snowflake PnC. b) photonic and c) phononic band structure of a silicon planar snowflake crystal with (d, r, w, a)= (220, 200, 75,500) nm. d) SEM image of the fabricated snowflake crystal structure. e) Schematic image the fiber-taper-coupling method used to characterise the optical properties of the array.

band gap and a pseudo optical band gap. The phononic band gap is located at 6.9-9.3 GHz while the pseudo photonic band gap is located at 185 to 285 THz which corresponds to a wavelength of 1620 to 1275 nm.

1D periodic structure with a pho(X)onic cavity was theoretical modelled by Psarobas and Papanikolaou in 2010.[28] They found that a periodical system built from homogenous SiO_2 and Si layers show a strong non linear acousto-optic effect in a pho(X)onic cavity. A full theoretical and experimental characterization of a PXC is given within this work, a detailed description is given in chapter 9.

4 Aims and Objectives

As mentioned in the previous chapters it is important to gain a deeper understanding of photonic (PtCs) and phononic crystals (PnCs). To understand the motion of photons and phonons is essential for tuning light, sound and heat propagation. To realise and further develop devices like acoustic diodes, acoustic rectifiers, and to improve the medical utility of focused ultrasound it is indispensable to study the interaction between phonons and nanostructured materials. The goal of this thesis is the fabrication and characterisation of new, one dimensional photonic and phononic crystals on the nanoscale.

For the fabrication of nano-scale structured materials first of all nano-scaled building blocks are needed. Since a density contrast is indispensable for PnCs, we decided to combine soft (low density) polymers and hard (high density) inorganic nanoparticles.

Most of the superlattices (SL) within this work are build up from commercially available poly(methyl methacrylate) and oxide nanoparticles. Changing the building blocks of the SL opens the possibility to tune the position and width of the band gap. This allows so-called band gap engineering and thereby influencing the optical and acoustic properties of the material. The positions of the band gaps is not only determined by the materials of the SL, but the lattice spacing as well. If we want to equip SLs with tunability, we can incorporate layers which can be swollen by solvent vapour. These layers can be build up from responsive polymers. RAFT polymerisation allows to synthesize polymers with a well defined molecular weight and low dispersity. On top of this, the polymerisation of active esters opens the possibility to add functionalities to the polymer *via* post polymerisation reactions. Poly(vinyl pyridine) is known to swell in the presence of ethanol or water depending on wether it is quaternized or not. In the presence of water vapour the lattice spacing is increased and therefore the photonic an phononic band structure changes. This could be interesting for the use of such SLs in optical sensors for solvent detection.

As high density materials, oxide nanoparticles are used. Titania with a density of the bulk anatase phase of 3.79 g/cm^3 seems to be a promising candidate, especially because the synthesis of nano-sized titania is well established. Another promising candidate is barium titanate with an extremely high density of 6.08 g/cm^3 for the bulk material. On top of their high density, both oxides show a high refractive index which opens the possibility to not only get PnCs but also to fabricate crystals with a dual phononic and photonic band gap.

Even though many synthesis strategies for titania and barium titanate nanoparticles are known, their application in nanostructured SLs poses new challenges. On

one hand they need to be small enough to fabricate uniform layers in the range of 50 nm, while on the other hand they should have a good solubility for an easy processing while being non-soluble in the solvent of the polymer. Another problem arrises from the porosity of the nanoparticle layers if nano-sized spheres are used. The synthesis of cube shaped nanomaterials is promising for the fabrication of less porous and therefore higher density layers.

Barium titanate nanomaterials are further interesting because of their ferroelectric properties. Nanorods from this material could find interesting applications in ferroelectric liquid crystals, because they should align in an electric field.

Besides changing the building blocks of the superlattices a different stacking order is also investigated. While first a simple $(AB)_n$ lattice is studied, later on $(ABAC)_n$ structures are build to study their photonic properties. Further, the influence of different defect layers and their impact on the band structure is interesting. The integration of colloidal silica particles as a defect layer in a PMMA silica SL is discussed within this work.

The aim of this work is to fabricate new SL. With this work we want to tie on the work of the PMMA-SiO_2 SLs and substitute PMMA with responsive polymers and the SiO_2 with different inorganic nanoparticles as described above. Especially the usage of $BaTiO_3$ nanoparticles seems very interesting because $BaTiO_3$ is one of the materials with the highest density known and therefore gives an enormous contrast to the polymer density. And by heighten the density contrast we hope to widen the phononic band gap.

In the following chapters, the synthesis of titania and barium titanate nanoparticles is presented (Part II: Building blocks) followed by the fabrication of different SLs and insights into these photonic and phononic band gap materials (Part III: Superlattices).

Part II

Building Blocks

In this part a description of the synthesis of high refractive index and hard inorganic layer materials is given. Further, variations of the standard nanoparticle synthesis will be described as well as the application of the resulting nanoparticles.

5 Synthesis and Application of TiO_2 Nanoparticles

Manuscript: Nanoscale surface chemistry directs the tunable assembly of anatase nanocubes into three-dimensional superlattices

5.1 Abstract

An important step in nanocrystal self-assembly is programming the large-area organization of a single type of nanocrystals into distinct superlattices with tunable packing efficiencies. Here we utilize nanoscale surface chemistry to direct the self-assembly of anatase nanocubes into a distinct three-dimensional superlattice. High nanocrystal solubility combined with weak electrostatic attraction was sufficient to assemble the 3,4-dihydroxy-cinnamic acid (DHCA) functionalized nanocubes into large superstructures. The characteristic dimensions of the superlattice are controlled by the particle concentration. The nanocubes assemble into large and highly oriented thin arrays induced by the pH mediated surface charge (pH: 12.5) during the initial phase of drying-mediated self-assembly. The discovery that translational and orientation order of nanocrystal superlattices can be induced by the interplay of thermal energy, steric repulsion and ionic interactions in a nucleation and growth self-assembly process offers new insight on the importance of the initial nucleation stage in the self-assembly process and suggests new routes for controlled self-assembly of nanocrystals.

5.2 Introduction

Self-assembly of micrometer- and nanometer-scale colloidal particles into ordered mesocrystalline structures, whose properties can be tailored by manipulating the size, shape and composition of the nanocrystalline building blocks in a LEGO-like manner has evolved in recent years to a materials concept important for both, fundamental science and technological applications.[29,30] In particular, inter-particle interactions in nanocrystal superlattices can lead to collective properties, which are significantly different from those of the corresponding isolated nanocrystals.[31–33] A fascinating aspect of these superlattices is that their properties may be tailored not only through the size and properties of the individual building blocks, but also by the interactions between them.[34] Therefore nanocrystal superlattices offer unique opportunities to study many collective phenomena of granular materials,[35] such as metal-insulator transitions,[36] resonant energy transfer[32] or plasmon propagation.[37] Therefore,

controlling the spontaneous organization of nanoscale objects is a grand challenge for nanotechnology and materials design.

Existing methods for fabricating nanocrystal superlattices are based on the self assembly of highly monodisperse colloidal nanocrystals through solvent evaporation or by antisolvent destabilization.[32] The self-assembly of nanocrystals is a complex process, involving a multitude of interactions and driving forces (van der Waals, Coulomb or dipolar interactions).[32] Therefore the formation of superlattices with long-range ordering requires precise control over many variables, e.g. the size distribution of nanocrystals, capping ligands, and solvent evaporation kinetics etc.. As a consequence nanocrystals may be stabilized by weak non-covalent or strong covalent forces, and nanocrystal assemblies may be ordered or disordered. Self-assembled nanocrystal superlattices often show poor collective properties (e.g. electrical conductivity) due to the large inter-particle spacing induced by the capping ligands,[38] and post-treatments like ligand exchange,[39–41] aging[42] or sintering[43] are required to enhance mechanical stability[41,43] and electronic coupling[39,40] which in turn can lead to additional structural defects.[44–47] A associated defect analysis has been carried out in detail for larger (approx. 100 nm) colloidal particles.[[47] Less information is available for smaller (<10 nm) particles in mesocrystals, where the energy required for the reorganization of the building blocks easily leads to the formation of defects.[48]

Despite recent advances in self-assembly of nanoparticle superlattices, the constituent materials have been limited to those cases, where uniform nanoparticles are available in sufficiently large quantities. Metal oxides like TiO_2,[43,49–56] which are made by polycondensation reactions, usually show a significant amount of inhomogeneity and disorder. TiO_2 is an attractive material for environmental and energy applications (e.g. water splitting for H_2 evolution,[57] dye-sensitized solar cells,[58] and lithium-ion batteries[59]). Under illumination with ultraviolet (UV) light electron-hole pairs are created, but only a small fraction of the photogenerated charge carriers can be separated to form reactive oxygen species for subsequent surface oxidation/reduction processes.[60] Therefore close packed TiO_2 supercrystals (NCs) were suggested to enhance the photocatalytic activity and performance of dye-sensitized solar cells through efficient electron hopping between adjacent nanocrystals.[61,62] Ordered assemblies of TiO_2 nanocrystals have great promise for applications, but the composition-dependent intrinsic defect structure of the nanocrystals as well as the defect structure of the supercrystal will be critical for their electronic properties.[63] In this work, we investigate the formation of TiO_2 nanocrystals and the assembly of supercrystals after surface functionalization with 3,4-dihydroxy-cinnamic acid (DHCA).

TiO_2 nanocrystals can be synthesized in different ways. The sol-gel approach allows selecting between the rutile, brookite and anatase polymorphs through the solutions pH. The morphology of the resulting nanocrystals (spheres, cubes, rods) may be tuned by varying the precursors or the concentration of additives. Appropriate

surface ligands may provide solubility of the particles in hydrophilic or hydrophobic solvents. In an early contribution Burnside *et al.*[64] reported a sol-gel synthesis of anatase nanoparticles whose morphology could be changed from rod-like (low temperature) to tetragonal or tetrahydral/bipyramidal (high temperature) by varying the reaction temperature. Liu *et al.*[65] reported the synthesis of anatase nanocubes by an anion-assisted synthesis and demonstrated that the anions present during the synthesis can not only tune the shape of anatase nanocrystals but also change the phase from anatase over brookite to rutile. Roy *et al.*[66] demonstrated that by varying the ratio of diethanol amine/tetrabutylammonium hydroxide (TMAOH) the morphology of the anatase nanocrystals can be varied from ellipsoidal over rod- or capsule-like to cube- to sheet-like. A detailed morphological characterization of the TiO_2 nanocrystals as a function of the synthetic parameters combined with a comprehensive structural analysis of the assemblies of TiO_2 nanocubes shows the structure-directing effect of the nanocrystal morphology.

5.3 Results and Discussion

5.3.1 Synthesis

The truncated TiO_2 nanocubes were synthesized by a modified hydrolytic/hydrothermal approach.[64] The white TiO_2 precipitate resulting from controlled hydroxylation of titanium isopropoxide with water was isolated and transferred into a Teflon-lined stainless steel autoclave after being aged for at least 72 h. 3,4-dihydroxycinnamic acid (DHCA) and tetramethyl ammonium hydroxide solution were added in different concentrations (5, 10, 15, 20, 25 %) and different solvents (water and methanol). The autoclave was heated initially to 120 °C for 4.5 h to induce peptisation and subsequently for 6 h to 195 °C to induce particle growth. The resulting nanoparticle dispersion had a claret-red colour due to the charge transfer between the non-innocent DHCA ligand and the TiO_2 nanocrystal[67] and contained nanoparticles in very high concentrations.

The Raman spectrum of the as-prepared TiO_2 nanocrystals (figure 5.6, Supporting Information) is similar to those in the bulk anatase, but the vibrational bands show blueshift and line broadening because of the particle size. Anatase has has six Raman-active modes and three infrared (IR)-active modes, and the Raman bands at 144, 399, 518 and 637 cm^{-1} can be assigned as the E_g, B_{1g}, A_{1g} or B_{1g}, and E_g modes of anatase phase.[68] The strong E_g mode at 144 cm^{-1} is characteristic of the of the anatase structure indicates the presence of long-range order. The expected band of the DHCA ligand binding to the surface Ti atoms[69] can not be found due to their low concentration and therefore their low intensity in comparison to the TiO_2 bands.

The appearance and UV-Vis spectrum of the DHCA functionalized anatase nanocrystals is shown in figure 5.7 (black line). The nanocube solution is transparent between 600 and 800 nm; weak Rayleigh scattering was observed from 400 to 500 nm.

The solution of an anatase sample prepared without DHCA functionalization (UV-Vis spectrum in figure 5.7 red line) was turbid, indicating that DHCA functionalization is needed for the preparation of the transparent colloidal solutions.

Figure 5.8 shows the photoluminescent emission spectrum of the anatase nanocrystals measured with an UV excitation wavelength of 365 nm. The broad emission band centred at 475 nm can be assign to band edge luminescence of the anatase nanoparticles. Photoluminescence in nanostructured anatase originates from electrons trapped at Ti^{4+} sites within the bulk and holes trapped at lattice oxide ions immediately below the surface.[70–72] However, in our case, X-band electron paramagnetic resonance (EPR) spectroscopy studies did not reveal the existence of any oxygen or titanium defects associated to unpaired electrons, which can potentially induce photoluminescence effects in the anatase nanopowders.

The morphology and size of the TiO_2 nanocrystals could be controlled by (i) varying the concentration of tetramethyl ammonium hydroxide (TMAOH), (ii) through the choice of the solvent and (iii) the reaction temperature. Although mostly spherical TiO_2 nanocrystals were obtained for low TMAOH concentrations, exclusively cube-like TiO_2 (anatase) nanocrystals were obtained when the TMAOH concentration was 15 wt% and the reaction temperature was 195 °C. The small but critical change of the additive concentration appears to promote the formation of anatase nanocrystals with a non-spherical, faceted shape. For TMAOH concentrations of 15 wt% cubic nanoparticles (size 15 ±1 nm) were obtained (figure 5.1).

Figure 5.1a shows a schematic representation of an 100 faceted, truncated anatase nanocube. The average edge length of the nanocube is 15 nm (corresponding to a face diagonal length of 12.7 nm (assuming no truncation of the nanocube). Figure 5.1b and c show the anatase nanocubes at two different magnifications with the associated particle size distribution, a HRTEM image (with the corresponding Fourier transform as inset) is provided in figure 5.1d and e. The electron diffraction analysis revealed the TiO_2 to be pure anatase. Electron diffraction data (figure 5.1f) were compatible with the reported data for anatase (I 41/a md (No. 141), a=3.7845 Å, c=9.5143 Å, Z=4, JCPDS 21-1272), as confirmed by x-ray diffraction for a bulk sample. The x-ray diffractogram in figure 5.9 (Supporting Information (SI)) displays broad Bragg maxima indicative of small crystallite sizes. Due to the reflection broadening and the polymorphic behaviour of TiO_2 a quantitative phase analysis was performed by full pattern profile analysis[73,74] to differentiate between all possible phases (rutile (JCPDS 21-1276), brookite (JCPDS No. 29-1360), pseudobrookite (JCPDS 00-041-1432), Magneli-type phases).[75]

In aqueous solution the morphology and size of the anatase nanocrystals could be controlled by varying the TMAOH concentration. Figure 5.2 shows the TEM images of the resulting nanoparticles obtained by varying the TMAOH concentration from 5 to 25 wt%. While spherical particles with a size of about 9 ±2 nm were obtained for low concentrations (5 wt%) (figure 5.2a), the particle morphology changed from fully spherical (100%) to a mixture of spherical, rod-like and cubic particles for

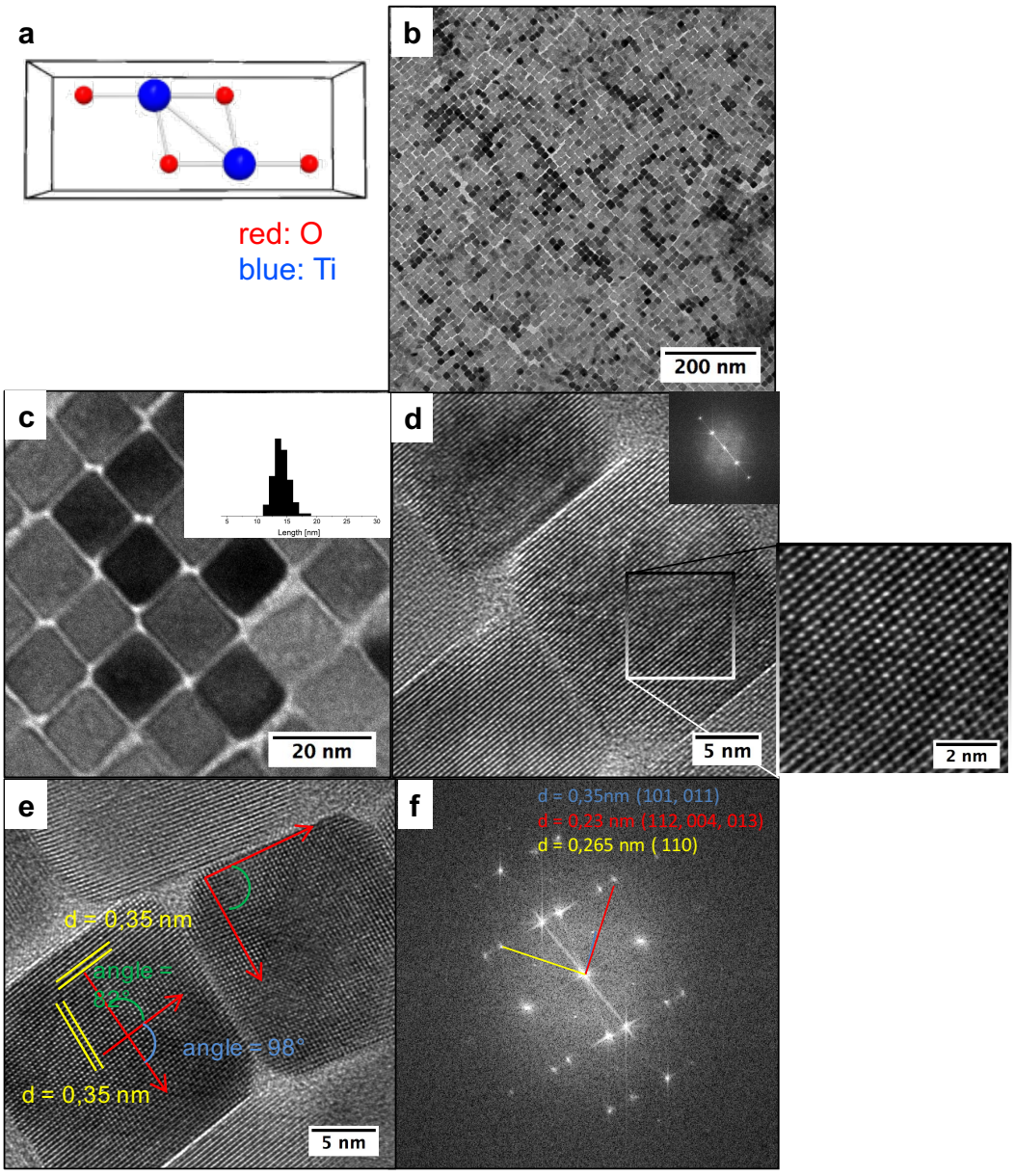

Fig. 5.1: Characterization of the anatase nanocubes. (a) Schematic representation of an 100 faceted, truncated anatase nanocube. (b, c) TEM overview images of a dense nanocube monolayer formed by drying at room temperature. (d) High resolution TEM image with Fourier transform (FFT) (e) d values and angles and (f) corresponding electron diffraction pattern ED pattern. The x-ray diffraction pattern of a bulk sample of the nanocubes can be found in the SI.

TMAOH concentrations of 10 wt% (Figure 2b). The size distribution was broader now, the nanoparticle size ranged from 6 to 29 nm (average 15 ±5 nm). For TMAOH concentrations of 15 wt% cubic nanoparticles (size 15 ±1 nm) were obtained (figure 5.1, vide supra). Further increasing of the TMAOH concentration to 20 wt% (figure 5.2c) delivered particles with well-defined morphology, and the percentage of cubic particles decreased again. TMAOH concentrations of 25 wt% and higher had no significant impact on the particle morphology and lead only to a slightly broader size distribution (figure 5.2c,d, 14 ±2 nm and 15 ±3 nm for concentrations 20 wt% and 25 wt%, respectively).

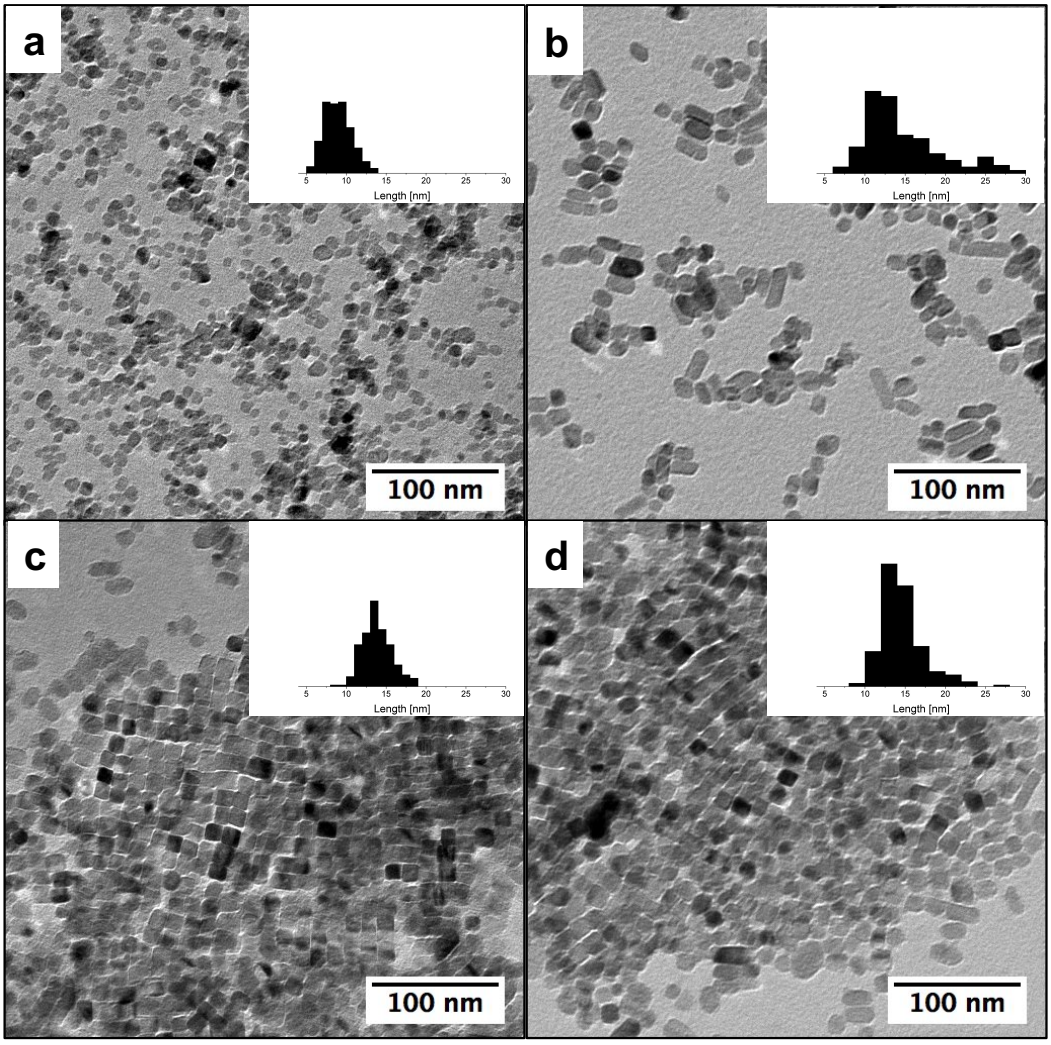

Fig. 5.2: TiO_2 particles synthesized at a TMAOH concentration of a) 5 %; b) 10 %; c) 20 %; d) 25 % (inserts: size distribution).

Variation of the autoclave temperature (at a constant TMAOH concentration of 15 wt%) from 170 °C over 195 °C to 220 °C induced pronounced changes of the particle morphology. In the lower temperature range at 170 °C a mixture of spherical, cube- and rod-like particles with a broad size distribution ranging from 6 nm up to 40 nm was formed (Figure 5.3a), whereas uniform nanocubes were formed at 195 °C

(figure 5.3b). At an autoclave temperature of 220 °C nanocubes were formed as well, but the size distribution was significantly broader (15 ±4 nm, Figure 5.3c).

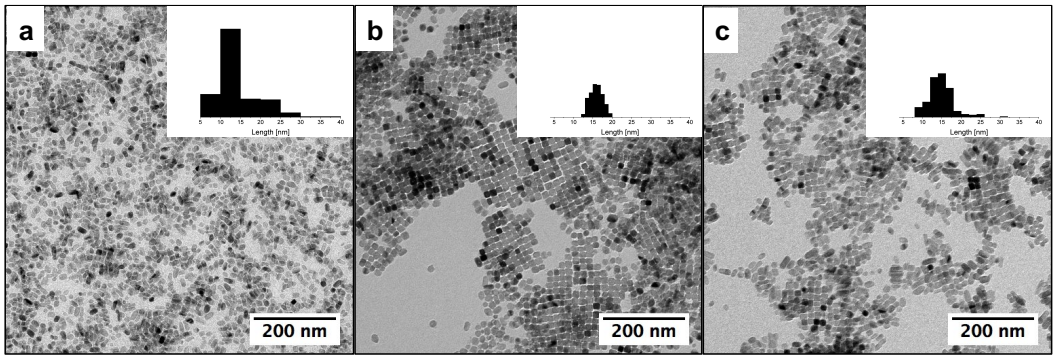

Fig. 5.3: TEM micrographs of anatase nanocrystals autoclaved at (a) 170, (b) 195, and (c) 225 °C in aqueous solution containing 15 wt% of TMAOH. Size distributions are shown in the insets.

In methanol the morphology of the nanocrystals remained always spherical, but their size increased from 9 ±2 nm to 17 ±3 nm when increasing the TMAOH concentration from 5 to 25 wt% (figure 5.4).

Most reported syntheses of TiO_2 particles use loosely bound surface ligands that do not exert a strong effect on particle solubility and properties. Typically, the particle solubility is low and particle dispersions are difficult to process. TiO_2 (and many metal oxide) nanocrystals can easily be functionalized with catechol-type ligands.[69,76,77] In particular, the high solubility of TiO_2 nanocrystals functionalized with 3,4-dihydroxy-cinnamic acid (DHCA) permits the preparation of very stable and highly concentrated nanocrystal dispersions (up to 200 g/L in alkaline ammonia solution)[78,79] proved useful for manufacturing well-ordered TiO_2 supercrystals.

The nanocubes could be assembled into mosaic-like particle arrays by placing a suitable substrate (e.g. a glass slide) in a concentrated aqueous dispersion of the nanocrystals and allowing the continuous liquid phase to evaporate. A scheme of the experimental setup is shown in figure 5.5a. Figure 5.5b shows a dense monoparticulate array with a thickness of approx. 1 µm from a dispersion with an initial particle concentration of 10 g/L particles in ammonium hydroxide solution (14 %) by allowing the particle layers to rearrange for a period of up to 2 weeks. The advantage of the assembly technique is its simplicity; the method is robust again temperature changes and smaller disturbances. The thickness of the film could be controlled by varying the concentration of the nanocrystal dispersion. Depending on the size of the glass substrate sample areas of up to several cm could be coated. The surface in figure 5.5c shows many features of Kossel's model[80,81] of a growing crystal: (A) a flat surface, (B) steps, (C) kinks, (D) surface-adsorbed growth units, (E) edge vacancies, and (F) surface vacancies (see figure 5.12, SI). The slow evaporation of water appears to provide a sufficient fluidity of the nanocrystal building blocks to

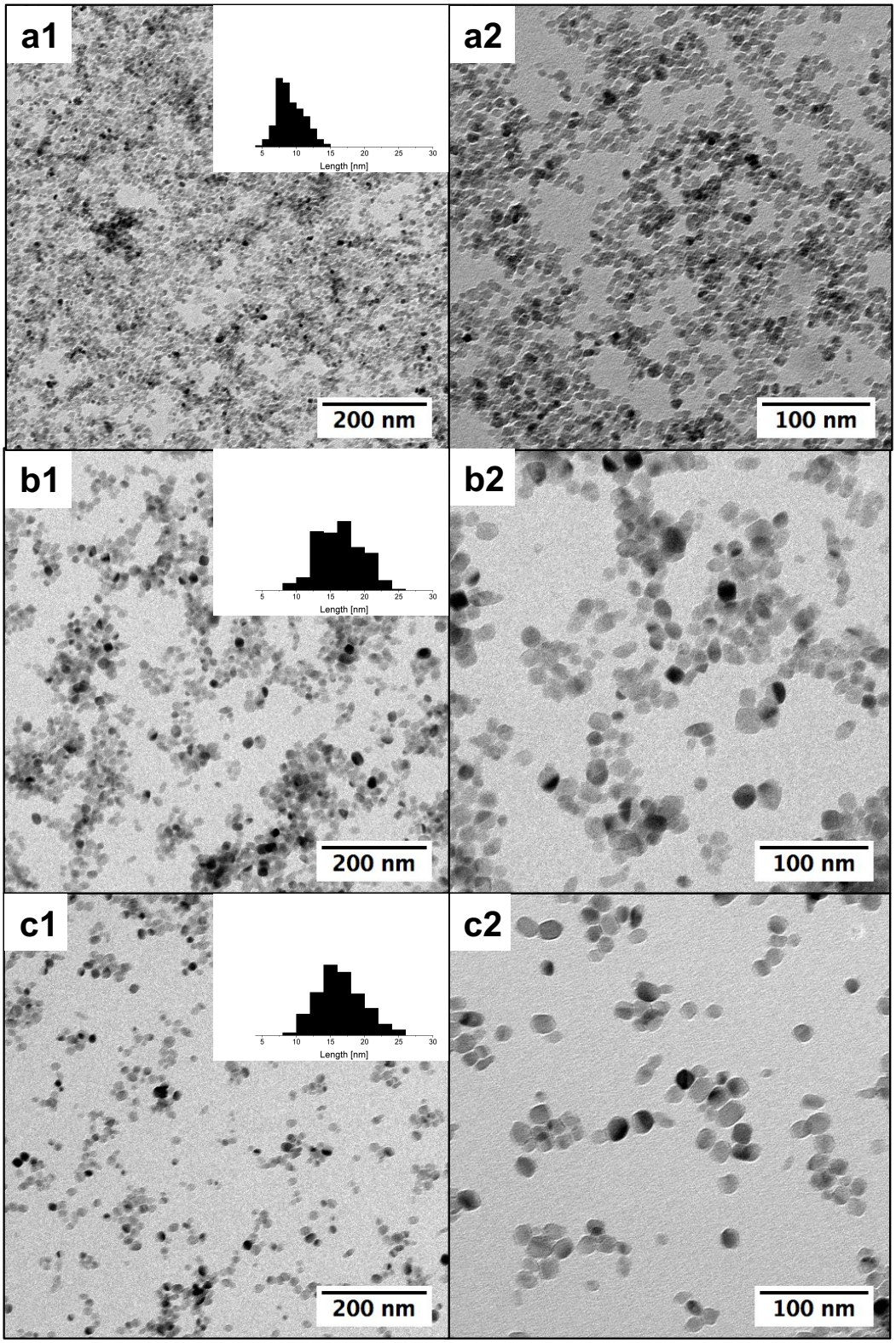

Fig. 5.4: TEM images of the TiO_2 nanoparticles synthesized in methanolic TMAOH, insert size distribution. a) 5wt% TMAOH, b) 15 wt% TMAOH and c) 25 wt% TMAOH.

promote particle rearrangement into a densely packed configuration with long-range order.

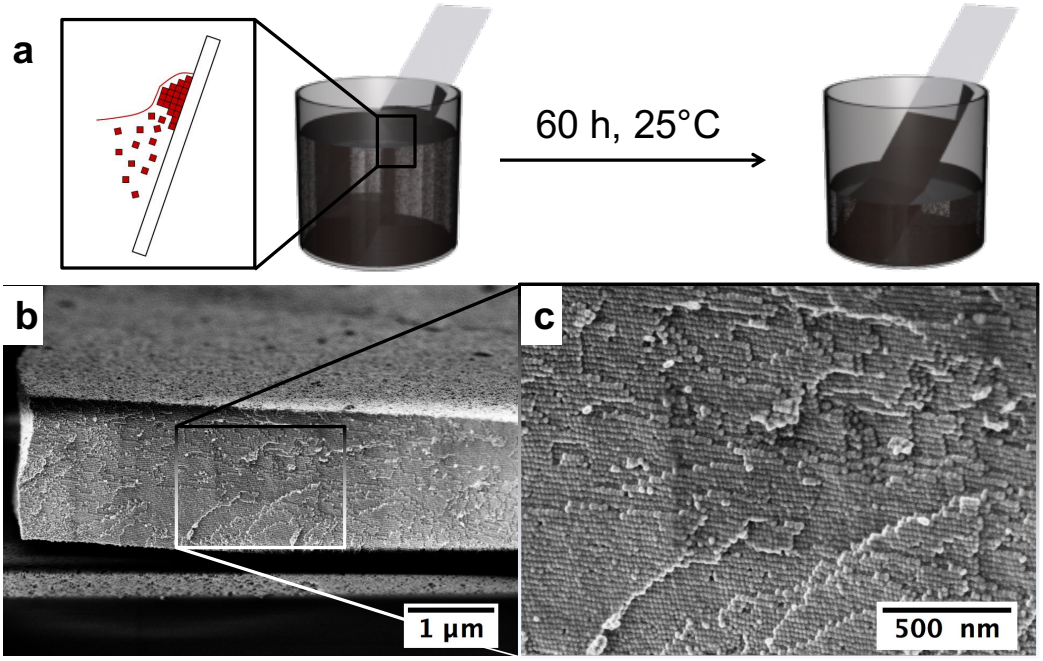

Fig. 5.5: Self-assembled oriented superlattice from anatase nanocubes. (a) Schematic presentation of the experimental setup. (b, c) SEM image of self-assembled of anatase nanocubes ordered in an oriented superlattice.

It was possible to fabricate nanocube superlattices with dimensions up several µm containing approx. 10^6 nanocubes by careful control of the particle concentration, temperature and evaporation time. Figure 5.5 shows a section of such a large superlattice that was obtained from a concentrated dispersion of DHCA-functionalized anatase nanocrystals. With suitable additives (e.g. polyvinylpyrrolidone) it is possible to suppress the formation of cracks. Naturally, the thermal equilibrium requires these very large superlattices to display defects and dislocations, but it may be possible to minimize these types of defects by tailoring the growth conditions.

The self-assembly process is based on the space filling of the building blocks and further controlled by the relative strength of van der Waals interaction, steric repulsion, directional dipolar and ionic interactions, superimposed by possible substrate effects and of drying-mediated self-assembly process in a thin solvent film.[82,83] Ionic interactions between the ammonium cations and the negatively charged DHCA-functionalized anatase nanocrystals are certainly the dominant forces in the hierarchy of interactions with a sufficient magnitude to create a long-range translational or orientational order, whereas the intrinsic interactions (i.e., the sum of van der Waals attraction and steric repulsion) between the anatase nanocrystals in our system are certainly weaker.The mosaic-like arrays formed by drying a solution droplet on a TEM grid (Figure 5.1b) suggests that the nanocubes initially form small ordered clusters that - with time - condense into a large ordered

array during a drying-mediated process. Ordering is a balance between lattice energy and thermal energy, and ordering therefore occurs in a certain temperature range. For an individual particle size of approx. 15 nm the thermal energy is sufficient for the particles to reorient. This "blocking temperature" also has a time component, which is generally defined as the point at which a particle can reorient under the influence of a specified field (gravitation, magnetic, electric) in approx. 100 s (a typical timescale for a measurement). Therefore it seems feasible that reorientation of individual particles may be related to the nucleation and growth of clusters beyond a critical size.

The additional electrostatic attraction of the nanocube anions and ammonium cations can promote the formation of a nucleus that is sufficiently large to dominate the subsequent growth of an ordered colloidal crystal with common orientation. The similarity of the surface structure of the superlattice in fig. 5.5 to Kossel's model[80,81] of a single crystal grown from solution lends support to the hypothesis that the superlattice grows by a slow crystallization process. Although the electrostatic interactions between the individual anatase nanocrystals may be responsible for the alignment of the nanocubes, it seems reasonable that other attractive forces such as van der Waals interactions play an important role for the slow growth of large, highly ordered three-dimensional superlattices.

In summary, we have demonstrated that large anatase nanocube superlattices with a high degree of crystallographic orientational order can be fabricated after suitable surface functionalization of the building blocks by slow solvent evaporation in a nucleation and growth self-assembly process. The strategy to induce a translational and orientational order of a superlattice of anatase nanocrystals by a electrostatic forces through the surface ligand may be extended to other systems, in particular superparamagnetic[45,82] or ferroelectric[83] nanocrystals, but also could be used to tailor more complex structures from other systems, e.g. anisotropic[84,85] or Janus particles[85] that display directional, anisotropic interactions. Further the application of the cubic nanoparticles as building blocks in hybrid SLs would help to decrease the voids in the inorganic particle layers and might yield in closely packed high refractive index - high density layers allowing to improve the photonic and phononic properties of the SLs.

5.4 Experimental Section

Titanium(IV) isopropoxide 98 % (TIP) was purchased from Acros Organics, Tetramethyl ammonium hydroxide solution 25 wt%, and 3,4-Dihydroxy hydrocinnamic acid 98 % (DHCA) were purchased from Sigma Aldrich. All chemicals were used without further purification.

5.4.1 Nanoparticle Synthesis:

In a typical synthesis 5.15 mL TIP was hydrolyzed by slowly dropping the TIP into 9.25 mL milliQ Water. After stirring the solution for 30 min the resulting white precipitate was collected in a Büchner funnel and dried at air for 30 min. After an ageing step of at least 72 hours, the resulting white powder was transferred into a Teflon-lined titanium autoclave, 0.24 g of DHCA and 3.52 ml of TMAOH solution (in different solvents and different concentrations) was added. The autoclave was sealed and heated to 120 °C for 4.5 h and 195 °C for 6 h respectively. The resulting claret solution was centrifuged for 10 min at 9000 rpm and the supernatant was used for further experiments.

5.4.2 Nanocubes assembly:

For assembling the cubic nanoparticles onto the substrate, first the substrates were cleaned by treatment with piranha solution washed with water and heated to 450 °C for about 1 h.

In a typical assembly process 5 mL of 10 g/L nanocube in 14 % ammonia solution was put into a glass jar, the substrate was carefully put into the jar and stored at RT for about one week.

5.4.3 Analysis:

TEM: For TEM analysis the nanoparticle solution was strongly diluted with ethanol and 3 drops of the solution was placed onto a carbon coated copper grid and dried at air. The images were taken with the transmission electron microscope JEOL 1400 at acceleration voltage of 120 kV.

HRTEM: For HRTEM measurements the same sample as for TEM imaging was used. For the imaging a Tecnai F20 device from FEI was used at an acceleration voltage of 200 kV.

SEM: The assembly was characterized by cross-sectional scanning electron microscope (SEM). Therefore the samples were broken and the edge was viewed with the LEO Gemini 153 at 0.7 kV.

XRD: Siemens D5000, transmission geometry, Ge(220) monochromator, Braun M50 position sensitive detector, step size 0.0155° at 2.5 sec step time.

5.5 Supporting Information

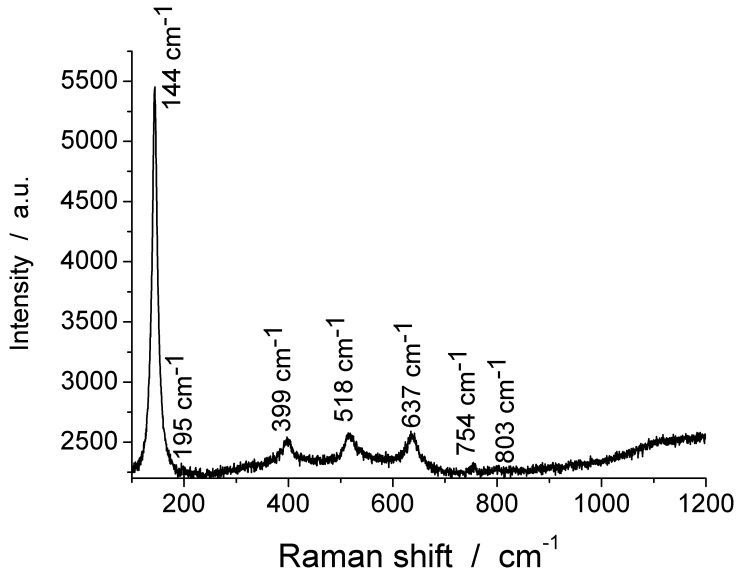

Fig. 5.6: Raman spectrum of the self-assembled anatase nanocube superlattice.

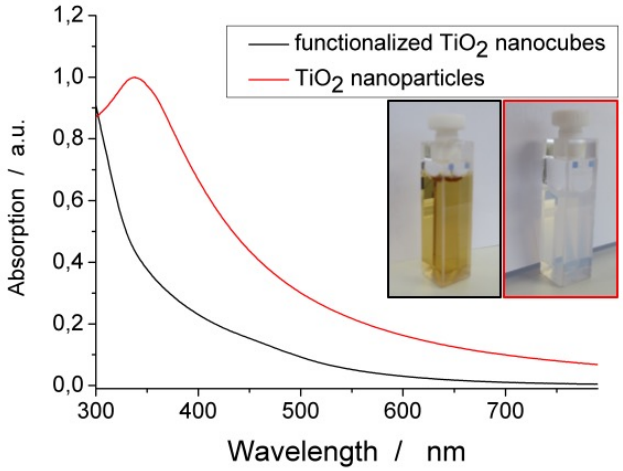

Fig. 5.7: UV-Vis spectra of the DHCA functionalized nanocubes (black line) and non-functionalized particles (red line), and photographs of the DHCA functionalized nanocubes (left) and non-functionalized particles (right).

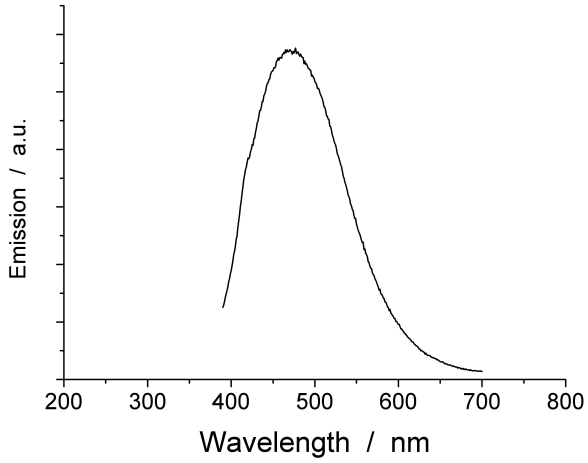

Fig. 5.8: Photoluminescence spectrum of the nanocubes with an excitation wavelength of 365 nm.

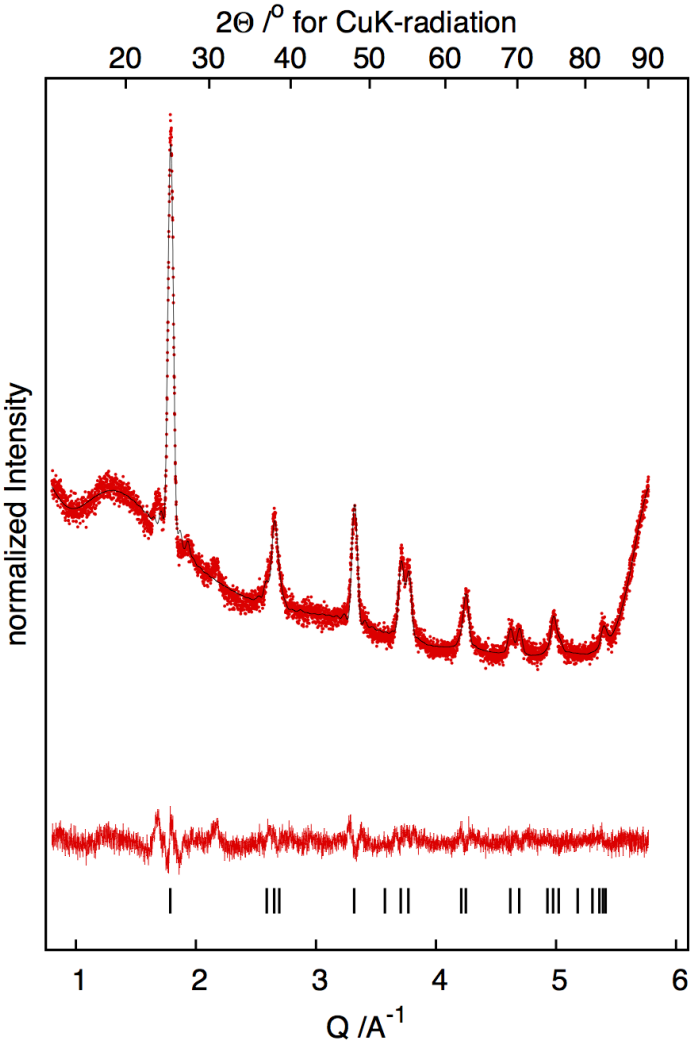

Fig. 5.9: X-ray diffractogram of the TiO_2 nanocubes.

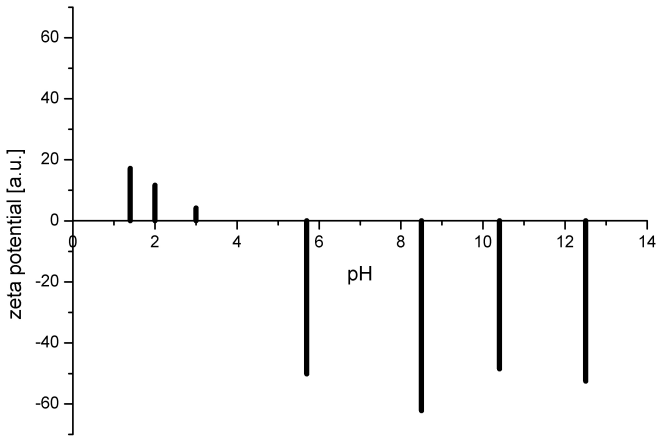

Fig. 5.10: Zeta potential of the nanocubes as a function of the pH.

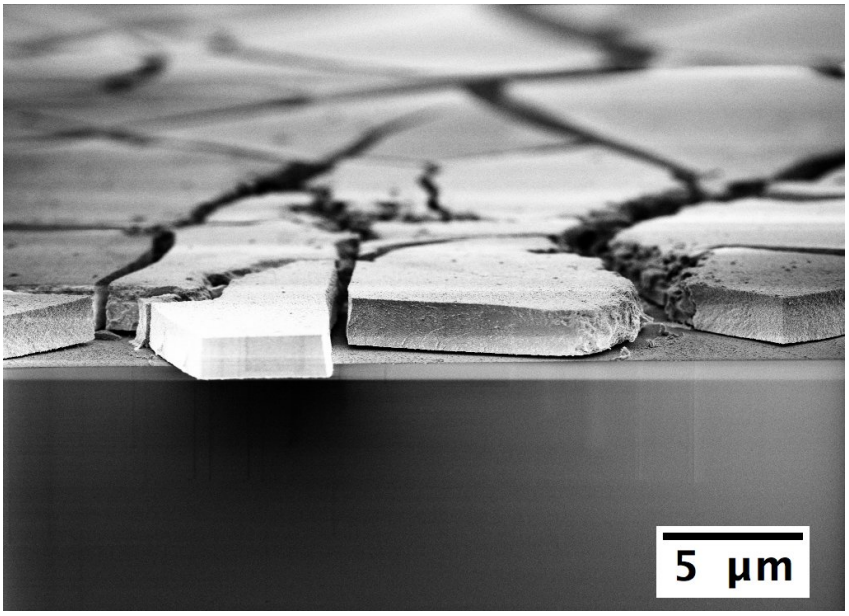

Fig. 5.11: SEM image of the assembled nanocube film.

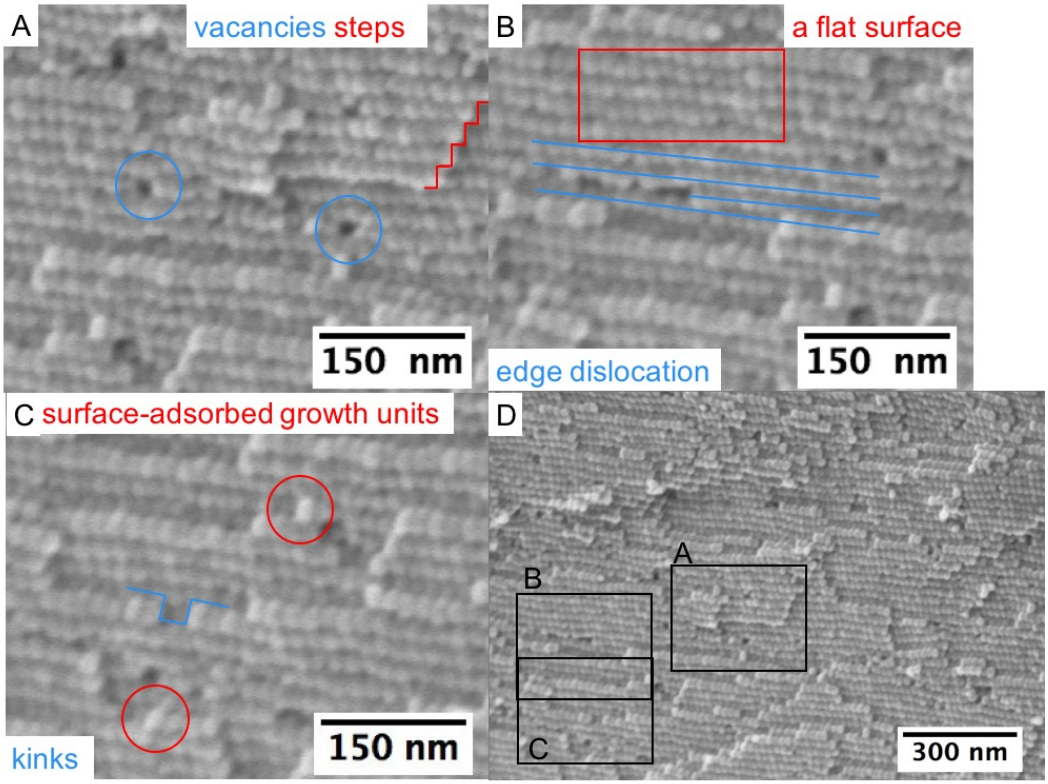

Fig. 5.12: Defects of growing nanocube mesocrystal after Kossel's model.

6 Synthesis and Application of $BaTiO_3$ Nanoparticles

6.1 Introduction

Barium titanate is a wildly used material. Besides being well established in the field of ceramics, it is interesting for application ranging from high κ capacitors and OFET gate dielectrics[86] over electrical energy storage devices[87] to liquid crystal displays[88] due to its ferroelectric properties.

For our work $BaTiO_3$ is attractive because of its high density of about 6.08 g/cm^3 and its relatively high refractive index of about 2.[89] This makes $BaTiO_3$ an excellent candidate for high density material in phononic crystals, while also providing strong optical contrast. Therefore $BaTiO_3$ is ideal for the fabrication of dual phononic and photonic band gap materials (see chapter 3 and 10).

In recent years there have been many approaches to control the growth of nano sized barium titanate particles and successful syntheses of spherical,[86,90–95] rod-like[96–100]and cubic[101–106] barium titanate particles have been published.[107] Most of the synthetic strategies are based on solvothermal synthesis, but especially for hydrophobic particles, syntheses in round bottle flasks with high boiling solvents seems to be most promising.[91] Other approaches include mechanochemical syntheses, in which the powders of barium carbonate and titanium oxide are reacted in a ball mill.[93] This syntheses yield the desired barium titanate powders but the particles show quite a broad size distribution. In 2008 a microwave assisted synthesis was published by Nyutu *et al.*[95] Here the advantage compared to other heating methods is a significant reduction of the reaction time.

In 2010 Huang and coworkers published a simplified synthesis of $BaTiO_3$ nano crystals with a size of about 10 nm,[86] which was based on a synthesis developed by Niederberger *et al.* in 2004.[92] Niederbergers method is a halide-free route to synthesise crystalline barium or strontium titanate starting from the metal barium. b Barium alkoxide is formed by the dissolution of barium in an alcoholic solvent and the addition of titanium isopropoxide yield the mixed-valent metal alkoxide. Through a heating step in an autoclave to 200 °C for 48 h the alkoxide mixture is transformed into the oxide material. Both authors report the a crystallite size of 10 nm and a pure perovskite phase.

Other authors published a $BaTiO_3$ synthesis starting from barium chloride and titanium chloride precursors in alkaline medium.[96] Furthermore they report that by adding ethylene glycol to the reaction mixture the morphology of the particles can

be changed from spherical to tetragonal rod-like shaped. They explain the formation of the tetragonal $BaTiO_3$ rods by reduced solubility of the Ba-Ti-OH intermediate through ethylene glycol.

A synthesis of cubic $BaTiO_3$ nanorods was published by Urban *et al.* already in 2002.[100] Starting from a BaTi-alkoxide precursor in heptadecane in the presence of oleic acid they synthesised nanorods with a perovskite phase. Here the oleic acid is the form-giving factor by forming micelles in heptadecane and thereby forcing the rod-like growth. A synthesis of cubic perovskite nanorods without additives can be achieved by using tetrabutyl titanate and barium acetate as precursors.[99] Another strategy to get well defined nanorods was developed by Limmer *et al.*, who used a polycarbonate membrane as a template to grow $BaTiO_3$ nanorods by electrophoresis.[97]

The variety of syntheses strategies to achieve different shapes of $BaTiO_3$ nanoparticles[102,104–106] until today[101,107] underlines the importance of this materials for new technological devices. In this work the strategy of Niederberger and Huang was followed to achieve $BaTiO_3$ materials, which are easy to spin coat. In a further step the synthesis conditions were optimised to tune the shape of the nanoparticles from spherical to rod-like.

6.2 Typical Synthesis of Barium Titanate Nanospheres

The here followed synthesis of barium titanate nanospheres[86] was scaled up to get a sufficient amount of nanoparticles for spin coating superlattices in an one batch synthesis.

In a typical synthesis ethanol was dried over sodium and redistilled under inert gas. Then 2.94 g of barium was transferred onto 180 mL of abs. ethanol under Schlenk-condition and stirred until all barium was dissolved. Over a septum 6.3 mL of titanium isopropoxide was added using a syringe. The mixture was homogenised for about 5 min before 180 mL of an ethanol water mixture (95:5) was slowly added over a dropping funnel. During the addition of the ethanol water mixture the reaction mixture turned into a transparent gel, which was transferred into three 250 mL teflon tubes. Hereby the gel was equally divided into the three vessels. The vessels were put into stain-less autoclaves, sealed and heated to 200 °C for 48 h. When the autoclaves were cooled down to room temperature, the resulting white slurry was transferred into centrifuging tube. After homogenisation of the mixture in a sonication bath for 5 min the reaction mixture was centrifuged (10 min; 9000 rpm). The washing step was repeated 3 times and the resulting white nano particle solution was put into glass vessel for storage. A further preparation of the spin coating solution is described in the chapter fabrication 7.

For TEM imaging the nanoparticles were dispersed in ethanol solution and dropped onto a carbon coated TEM grid using a pipette. The resulting particles are shown in figure 6.1. They show a average size of 7±1 nm with a narrow size distribution.

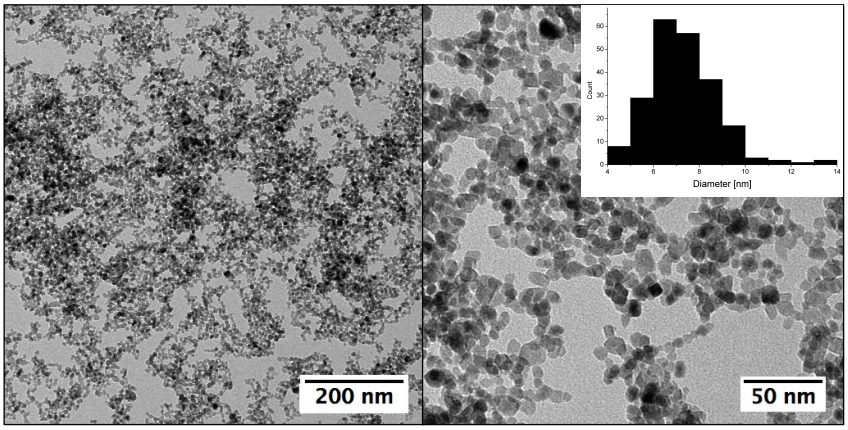

Fig. 6.1: TEM image of spherical $BaTiO_3$ particles in different magnification. Insert: Size distribution of the nanoparticles.

To confirm the formation of $BaTiO_3$ a x-ray diffraction pattern was collected. For the analysis the nanoparticles were dried at 100 °C, pestled and measured on scotch tape. The x-ray diffraction pattern confirmed the perovskite phase of $BaTiO_3$ (see figure 6.2).

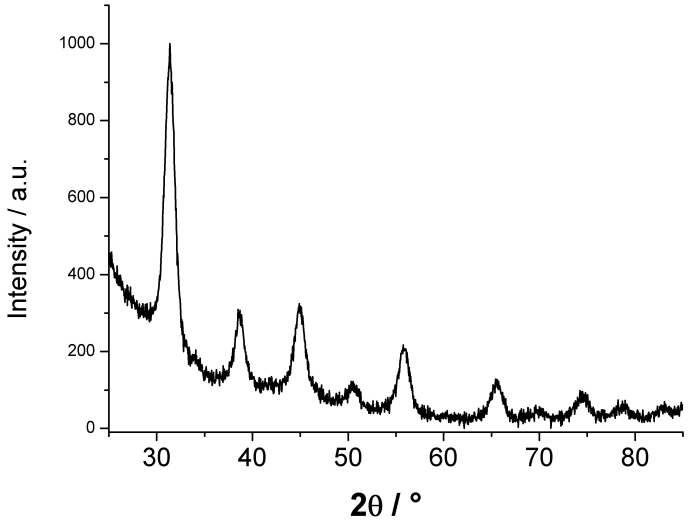

Fig. 6.2: X-ray diffraction pattern of $BaTiO_3$ nanospheres proofing the perovskite phase.

6.3 Barium Titanate Nanorods: Synthesis and Orientation in an Electric Field

Some experiments of this chapter were carried out by Tim Fischer during his Bachelor thesis co supervised by myself.

6.3.1 Motivation

$BaTiO_3$ is one of the most well studied ferroelectric materials in research. It was shown, that a seed mediated growth on $BaTiO_3$ nanoparticles in an electric field yields in cross-like/dumbbell shaped superstructures, orientated in well defined angles.[108] Meaning that the $BaTiO_3$ nanoparticles are sensitive to an external electric field and form a well defined superstructure when a electric field is applied. Further the orientation of iron oxide nanoparticles in external magnetic fields is well understood.[**Kral2014**, **Ho2015**] Following this two result we attempted to synthesise $BaTiO_3$ nanorods and orient them into superstructures by applying an external electric field.

6.3.2 Template-Mediated Synthesis

In a template mediated synthesis a precursor material is filled into a template. After the formation of the nanorods in the void space of the template, the template is removed and the nanorods can be isolated. Limmer *et al.* published such a template-mediated synthesis for $BaTiO_3$ nanorods, using barium acetate and titanium isopropoxide as precursors and a polycarbonate membrane as a template.[97] Following his lead we used the gel formed in our standard nanoparticle synthesis (see section 6.2) as precursor material and an AAO (anodic aluminium oxide) membrane as template. The gel was applied on the AAO disc and after a washing step the gel-filled AAO was heated to 450 °C to transform the gel into crystalline $BaTiO_3$. Finally the AAO was dissolved in sodium hydroxide solution and the $BaTiO_3$ rods were isolated.

This synthesis yield relatively large nanorods with spherical nanoparticles as side product. In figure 6.3 a laser and a transmission electron microscope image of the resulting particles are shown. On laser microscope image rods with an average length of 2 µm and a average thickness of 400 nm can be seen. Besides the nanorods all kind of other shaped particles are present. The TEM image gives a more detailed impression of the side products. It shows the presence of small nanoparticles beside the nanorods, these particles are similar to the particles formed in our standard synthesis. Further the nanorods look uniform in thickness, while the length of the particles varies a litlle. That allows us to assume, that the membrane was not completely filled with gel, so the incubation time of the gel into the membrane has to be optimized. Further experiments to reach a better filling of the membrane did not lead to homogenous particles. Only a electro-chemical approach seems to lead to a complete filling of the membrane and therefore to monodisperse nanorods.

Although the rods were not monodisperse we could use them for first orientation experiment in a electric field (see below).

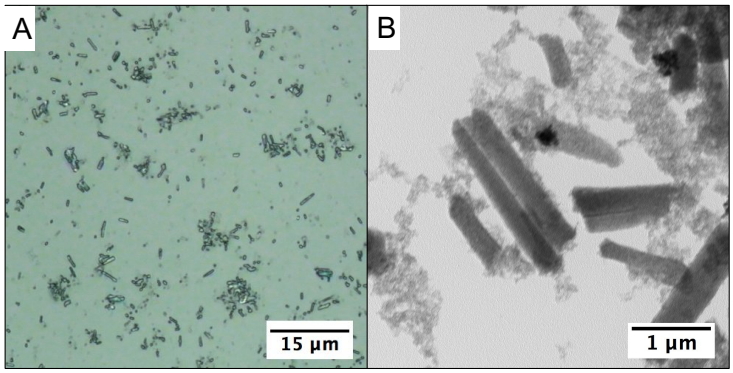

Fig. 6.3: A laser microscope image (A) and a TEM image of the $BaTiO_3$ nanorods.

6.3.3 Surfactant-Mediated Synthesis

In nanoparticle research the impact of coordinating molecules on the morphology of nanoparticles has been studied for different nanomaterials. For barium titanate acid function[100]as well as amino functions[99] have been reported to coordinate on the surface of barium titanate and therefore influence the morphology of the resulting nanoparticles.

We followed the procedure of Huang[86] and studied the influence of oleic acid in the reaction mixture on the morphology of the particles.

First we added different amounts of oleic acid to the $BaTiO_3$ gel just before it was transferred to the autoclave for heating. We added different equivalents of oleic acid in comparison with the equivalents of Ba used for the preparation of the gel. The resulting particles for the addition of 0.2, 0.66 and 1.33 molar equivalent of oleic acid are shown in figure 6.4.

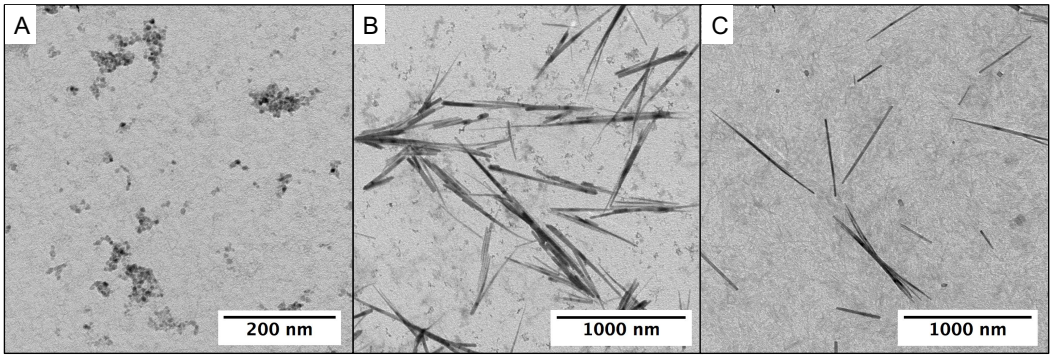

Fig. 6.4: TEM images of the $BaTiO_3$ nanoparticles synthesized with different amounts of oleich acids. A) 0.2 eq resulting spherical particles and B) 0.66 eq. C) 1.33 eq. resulting in nanorods.

The addition of 0.2 eq of oleic acid yields spherical particles with a average size of 7 nm (see figure 6.4A). These particles differ from the ones from the standard synthesis only in their solubility. While the standard synthesis yields particles which

are soluble in ethanol, the particles synthesised in the presents of oleic acid are soluble in hexane. The different solubility is caused by a coordination of the oleic acids on the surface of the barium titanate particles. The hydrophobic hydrocarbon chain of the oleic acid provides a good solubility of the particles in hydrophobic solvents. In the standard synthesis no surfactants are added during the synthesis leading to particles with good solubility in ethanol and more polar solvents.

By increasing the amount of added oleic acid to 0.66 eq the morphology of the resulting particles changes to rods (see figure 6.4B). The rods have a length of 250 to 1050 nm and a width of 10 to 30 nm. Some of the rods are branched and do not show a high monodispersity.

A further increase of the oleic acid amount yields in less polydisperse, and less branched nanorods (see figure 6.4C). They are around 1 µm long and 20 nm thick. These rods are soluble in hexane due to their oleic acid functionalization.

An even further increase of oleic acid to the reaction mixture was conducted by Tim Fischer. He showed that the formation of the rods could not be enhanced by a further increment of oleic acid, but instead a network like structure from barium titanate results.

The synthesis with the addition of 1.33 eq oleic acid provides the best results. The particles show the best morphology and a narrow size distribution. The formation of $BaTiO_3$ was confirmed by an EDX measurement with a resulting atomic ratio of 1:0.94 (Ba:Ti) (see experimental details figure6.8).

The addition of laurylamine did not effect the shape of the particles in this synthesis route. In his bachelor thesis Tim Fischer showed that the addition of laurylamine yield spherical particles which agglomerate easily.

6.3.4 Preliminary Experiments on Orientation of Nanorods in an Electric Field

The orientation of the nanorods in the electrical field was carried out in cooperation with Martin Brehmer from the Zentel group.

For the experiments an electric cell was used, as systematically illustrated in figure 6.5. The electrical cell was built from a microscope slide on which two copper tapes were fixed as electrodes. The gap between the two copper tapes forms the cell where the sample was filled in. To seal the cell a cover glass was put on top of the two copper tapes. The copper tape was connected to the electrical source by soldering two wires onto the tapes.

In a first experiment, the nanorods shown in figure 6.3 were filled in the electrical cell. Before applying an electrical field the nanorods were oriented randomly and no preferred orientation of the rods could be observed. Figure 6.6 shows the nanorods while applying a electrical field. They show a preferred orientation in the direction of the electric field with a clockwise rotation of around 20°. While applying a direct current (DC) a movement of the particles perpendicular to the electric field towards the anode was observed. This movement could be suppressed by applying

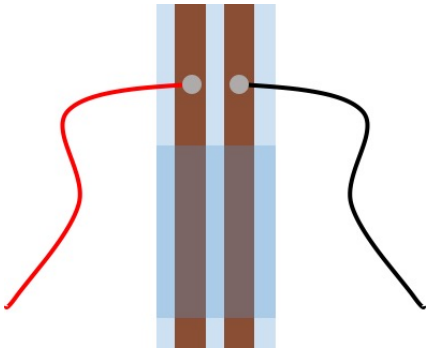

Fig. 6.5: Systematic scheme of the electrical cell.

an alternating current (AC). In this case the particles turned around in the speed of the change of the voltage.

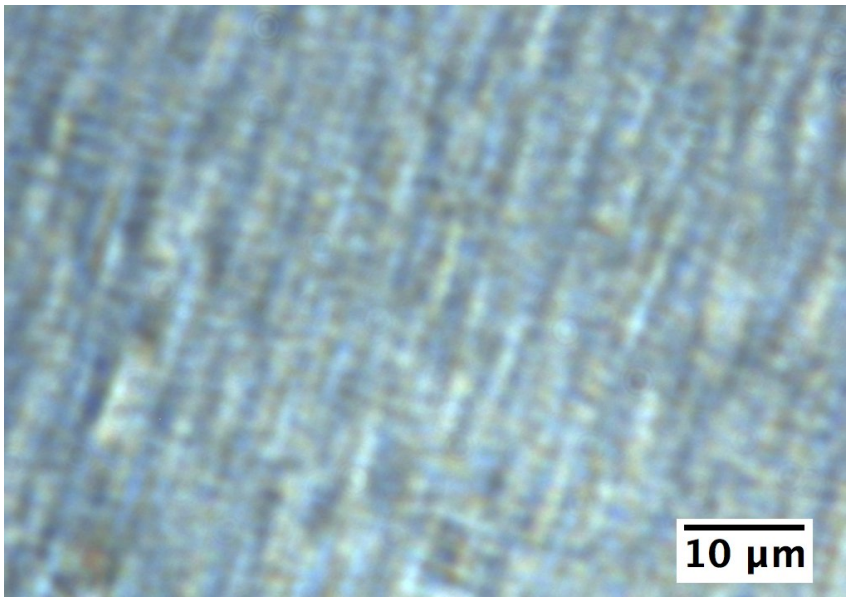

Fig. 6.6: Light microscope image of the $BaTiO_3$ nanorods in the electric cell while an electric field is applied.

To have a closer look at the orientation of the rods, another sample of the nanorods for the SEM was prepared. For the SEM imaging the absence of solvents is mandatory. The nanoparticles were dissolved in cyclohexane, transferred to the electrical cell and while applying the electric field all solvents was evaporated. The dried sample was measured with the LV SEM, the resulting images are shown in figure 6.7.

The nanorods are clearly orientated and all rods are aligned parallel to each other. They are not exactly oriented parallel to the field (the field was applied from left to the right side of the image), but shown a clockwise rotation of 30°. One possibility for the rotation could be caused by a change of the orientation through the outgoing solvent vapour during the drying process. The solvent vapour has to leave the cell

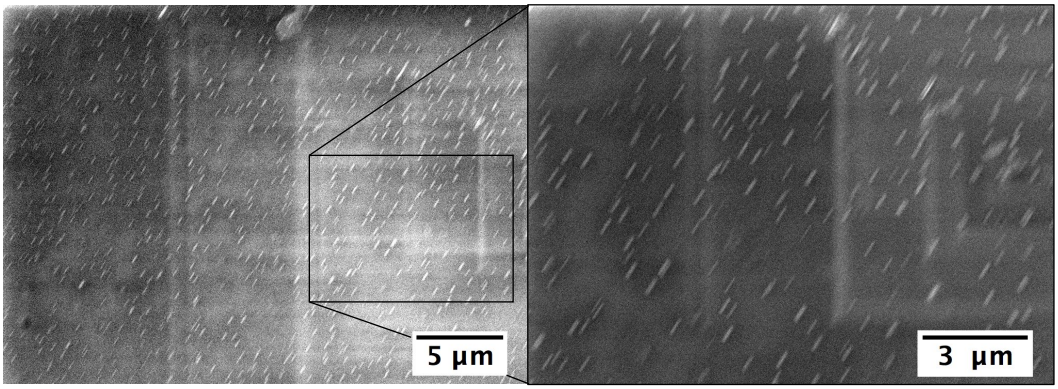

Fig. 6.7: SEM image of the oriented nanorods (top view).

on the top or the bottom side of the cell turning the rods a little while passing them. Another reason could be a tilted dipole in the nanorods.

6.4 Summary and Outlook

In this chapter the successful synthesis of $BaTiO_3$ nanorods could be shown. It was possible to reproduce the synthesis published by Huang *et. al*[86] and to scale the synthesis up to yield enough $BaTiO_3$ nanoparticle for spin coating. The influence of different additives on the synthesis of $BaTiO_3$ was invested. Oleic acid was found to bind on the surface of $BaTiO_3$ nanoparticles and therefore made them soluble in hydrophobic solvents. By further increase of the oleic acid concentration the morphology was successful changed from spheres to rods.

First experiments on the orientation of the $BaTiO_3$ nanorods show a orientation of the nanorods in the direction of the electric field with a small rotation of 30°. This orientation needs to be further investigated. The nanorods could be oriented because of their anisotropy or by their ferroelectricity. To confirm the orientation of the nanorods due to their ferroelectricity it is needed to heat the nanorods above their Curie temperature while applying the electric field. Only if they loose their orientation above the Curie temperature it is proofed that the orientation is caused by the ferroelectricity. Further the concentration of the nanorods in the assembly could be optimized. Higher concentrated nanorod mixtures could show liquid crystalline behaviour, which makes $BaTiO_3$ an attractive candidate for electro-optic switching devices.

And finally the synthesis of the nanorods need a further optimisation. First a sufficient amount for a XRD diffraction pattern has to be synthesized to confirm the perovskite structure of the nanorods and the concentrations of oleic acid needs to be fine tuned and the the influence of the concentrations, times and temperatures on the synthesis needs to be further investigated.

6.5 Experimental Details

6.5.1 Template Mediated Synthesis:

0.163 g of barium was dissolved in 10 mL absolute ethanol under inert gas conditions. After 0.35 mL titania isopropoxide was added, the formation of a gel was induced by adding 10 mL 95 vol% ethanol solution over a period of about 20 min. 1 mL of the gel was put onto a AAO membrane and the membrane was kept on an electrical shaker for 20 min. The membrane was carefully washed with water to remove the left over gel and heated to 200 °C for 2 h and to 450 °C for 2 h respectively. To remove the AAO membrane the filled membrane was kept in 1 M sodium hydroxide solution for 30 min. The nanorods were collected by centrifugation of the reaction mixture at 9000 rpm for 5 min. The particles were washed with 1 M sodium hydroxide solution and dispersed in ethanol or other solvents.

6.5.2 Surfactant Mediated Synthesis:

The gel was prepared like the gel in the typical synthesis of barium titanate nanospheres as described above. Before the gel was transferred to an autoclave the oleic acid was added. The added equivalents of oleic acid are always compared with 1 equivalent of Ba added to the gel. For A) 0.2 eq oleic acid 0.3 mL of oleic acid was added to 20 ml of the barium titanate gel. For B) 0.66 eq 1 mL and for C) 1.33 eq 2 mL respectively. After sealing the autoclaves the reaction mixtures were heated to 200 °C for 48 h. The resulting particles precipitated and were readily dissolved in hexane. Before further characterisation the particles were washed three times by dissolving them in hexane followed by a precipitation with ethanol followed by centrifuging the particles at 9000 rpm for 5 min.

6.5.3 Orientation in the Electric Field:

For the experiments we used the electrical cell shown in figure 6.5. Typically we used concentration of 1 g/L nanorods in ethylene glycol diether (for the *in situ* observation) or in cyclohexane (for the dried sample for SEM imaging). For the nanorods in cyclohexane we used a voltage of 50 to -50 Volt (AC) and for the samples in heptadecane a higher voltage of 100 to -100 Volt (AC) was needed. (For further details see:[109])

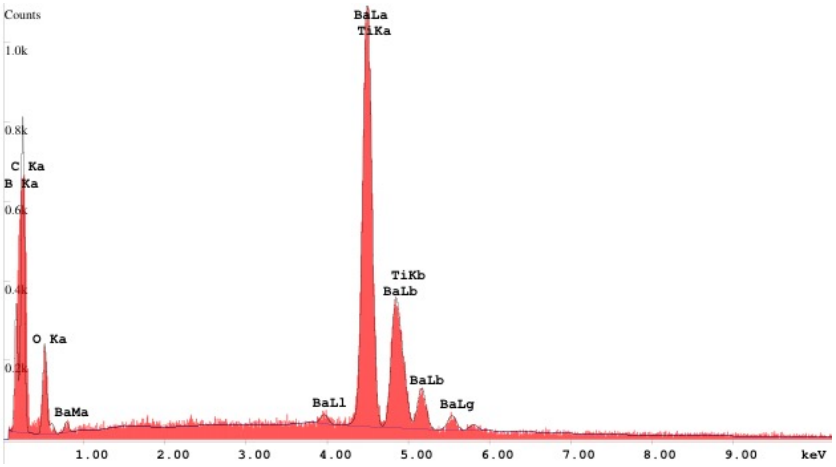

Fig. 6.8: EDX of the $BaTiO_3$ nanorods.

Part III

Superlattices

In this part the fabrication and characterisation of hybrid superlattices will be presented. Six different superlattices, with different compositions and different periodicity will be described and characterised.

7 Fabrication Method of the Superlattices

This chapter gives an introduction to the fabrication technique of the superlattices (SL), it is divided in two sections. The first section gives an introduction of the technique of spin coating, its advantages and disadvantages and the parameters used for the fabrication of all superlattices presented in this work are given. The second section gives a short overview of the used polymer and and nanoparticle solutions, explaining, which conditions are used and why.

7.1 Spin Coating Technique

The spin coating technique is a widely used technique to coat different kinds of substrates with thin films in the nanometer scale. Due to its simplicity it is already applied in microelectronic industries as well as in the manufacturing of digital versatile discs (DVDs) and compact discs (CDs).[110]

The principle of spin coating is very easy. Basically, a homogeneous solution of the to spin coated substance, a clean substrate and a spin coater is needed. First, the substrate gets fully covered by the solution using a pipette or an other dosing device and then the spin coater is started. During the acceleration of the spin coater, the spinning forces spread the solution over the substrate and further over the etch of the substrate, while the substrate is fixed to the chuck of the spin coater by a vacuum force. So the spare solution is disposed and the substrate is covered by the substance. The spinning takes place for a defined time until the solvent is evaporated. A schematic illustration of the spin coating table is given in figure 7.1.

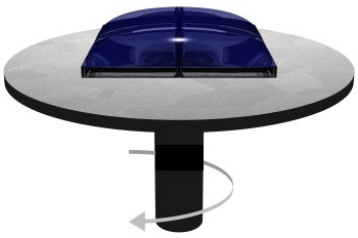

Fig. 7.1: Schematic image of the rotating unit of a spin coater.

As easy as that technique sounds, there are many parameters influencing the quality of the coating. One important factor is of course the nature of the solution used (this parameter is in discussed section spin coating solutions below). Further,

the surface of the substrate and the resulting interaction between the surface and the coating materials play an important role. For an optimal coating, a clean smooth substrate surface is needed. Glass or silicon substrate can be cleaned with piranha treatment. Piranha treatment means to etch the glass substate with a 3 to 2 mixture of sulfuric acid and H_2O_2 for about 30 min. After the piranha treatment the substrates can be heated to 450 °C to get a fully oxidised surface.

Other important factors are the spin coating parameters, i.e. the acceleration speed, the spinning speed and the duration of the spinning process.

The acceleration speed influences the speed in which the solvent is spread and removed from the substrate. If the acceleration is slow, the solvent is removed slowly and polymers and nanoparticles have time to agglomerate. To prevent agglomeration of nanoparticles during the spin coating, a high acceleration speed is needed, so that the solvent is removed very quickly.[111]

The spinning speed influences the shear forces acting on the solvents. If the shear forces are higher than the surface tension of the solvent, a uniform coating of the substrate can be achieved. Further, the spinning speed influences the thickness of the resulting coating layer. A high speed gives a thin film and a lower speed gives a thicker film, because more substance remains on the substrate.

The spinning time should be sufficient enough to let all solvent evaporate. If the time is too short, the solvent does not evaporate completely and a non-homogenous coating results. If too much solvent remains int the layer, the second layer might partly dissolve the first layer because the first layer is not stable.

Further the amount of substance used influences the thickness of the resulting layer.

The optimization off all these parameters can be found in the PhD thesis of D. Maschke[112]. The best resulting multilayers have been coated with an acceleration speed of 5000 rpm/sec and a spinning speed of 5000 rpm, a spinning time of 20 sec was long enough for a satisfactory evaporation of the solvents used.

For the formation of separated layers, a post-treatment after each layer coating is mandatory. During the spin coating process the solvent evaporates. Nevertheless, residual amounts of the solvent remain in the layer after spin coating. The polymer as well as the nanoparticles strongly interact with solvent molecules capture them within the layers. To achieve a coating of fully separated layers, it is mandatory to remove the residual solvents from the layers. Only by utilising a heat treatment a partially dissolution of the layers while spin coating the second layer can be prevented. Usually, it was sufficient to heat the samples to 100°C for 15 min. In some cases, 120 °C and 20 min were needed. The limiting factor for the temperature was given by the glass transition temperature of the polymer. If the polymer is heated above its glass transition temperature for too long, the structure of the layer will get destroyed or the polymer will penetrate into the nanoparticle film and disappear. The usage of a vacuum oven was considered as well. In this case, it would be possible to remove the solvents at low temperatures. But the first experiments in the vacuum oven

resulted in non-homogenous layers. Probably, the solvent was removed too fast and the layers were bursted.

In conclusion the spin coating technique is a very good technique to build up layered hybrid structures from polymers and nanoparticles in nanometer scale. A clean substrate as well as suitable solvents (see below) are mandatory. Furthermore a post heat treatment after each spin coating step is needed to obtain well-structured layered materials with a clear interface between the single layers.

7.2 Spin Coating Solutions

To obtain uniform layers by spin coating the solvents used need to have a suitably viscosity, small surface tension, a good volatility and, most importantly, the substance, which will be spin coated, should be well dissolved in the solvent of choice.[113] Organic molecules or polymers are widely used for coatings. Especially for the manufacturing of organic solar cells in research labs, many papers have been published on the theory as well as on the experimental optimisation of the spin coating process.[113–118] For the inorganic layer, there are basically two approaches to form homogenous layers using the spin coating technique. One is the spin coating of a precursor solution and the other is spin coating of a nanoparticle solution (see section below). Spin coating of precursor solutions has the advantage that it is possible to spin coat small molecules, which are usually well dissolvable in solvents and form highly stable solutions. The disadvantage of that method is that the desired component often needs a heat treatment at high temperatures. This makes this technique incompatible for hybrid structures. The polymeric components are often not stable at temperatures much higher than 100 °C and therefore melt or at higher temperatures even decompose to carbon monoxide and other gases.

For hybrid Bragg stacks, the different nature of the materials is a huge challenge. While nanoparticle layers are partly porous, the polymers tend to infiltrate into them. Due to the infiltration, the physical properties of the inorganic layer change. The degree of infiltration is difficult to predict and there fore should be measured. There is a limit of equipment for measuring the degree of infiltration.[119] The change of the physical properties significantly takes place in the density, sound velocity and refractive index. And this three factors strongly influence the properties of the phononic and photonic band structures. We studied one approach to stop the infiltration of the polymer into the porous inorganic layer by applying a blocking layer in-between (see below).

7.2.1 Nanoparticle Solution

For spin coating nanoparticle solutions the same factors as for spin coating any other solution are important. To form homogenous films, a solvent with a suitable viscosity and volatility has to be chosen further a good solubility of the nanoparticles in the solvent is needed to prepare a high concentrated stable nanoparticle solution.

Especially, oxide nanoparticles tend to agglomerate even at low concentrations and precipitate. There are different strategies to avoid the agglomeration.

For example TiO_2 nanoparticles can be stabilised by bringing a ligand onto the surface of the particles. A suitable ligand should contain two functional groups: One group to bind onto the nanoparticles and the other group to gain good solubility in the solvent and prevent agglomeration of the particles.

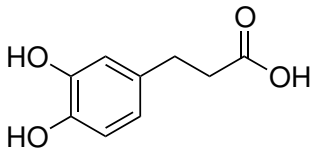

Fig. 7.2: Molecular structure of 3,4-dihydroxy hydrocinnamic acid.

A suitable ligand to enhance the solubility of TiO_2 in water is 3,4-dihydroxy hydrocinnamic acid (DHCA) (See figure 7.2). The catechol function has a good affinity to the metal oxide surface of the nanoparticles. So it is a good ligand and coordinates the metal ions on the surface of the nanoparticles well. Further, the acid function readily deprotonates in slightly alkaline solutions. This leads to a good solubility of the nanoparticles in diluted ammonia solution. The deprotonated carboxylic groups repel each other (figure 7.3) and hence prevent agglomeration of the nanoparticles. Highly DHCA-functionalized TiO_2 particle solutions can be prepared with a nanoparticle concentration as high as 200 g/L, which allows to spin coat relatively thick layers.

But before spin coating TiO_2 nanoparticles, the solution has to be diluted to the desired concentration (depending on the targeted layer thickness) and to 10 mL of the solution 100 µL of 10 wt. % sodium dodecyl sulfate (SDS) solution in water needs to be added. SDS acts as a detergent and reduces the surface tension of the ammonia solution. This leads to a better wettability of the substrate (or the underlaying layer) and yields a more homogenous coating. Further, the resulting solution needs to be sonicated for 5 to 10 min and finally filtrated through a syringe filter with a pore size of 0.45 µm (PTFE membrane) to remove the last agglomerates. The filtered solution was used immediately for the spin coating. If the spin coating procedure could not be finished within one day, the solution needs to be sonicated for another 10 min again just before the spin coating, to make sure that the nanoparticles are well-dispersed.

Barium titanate nanoparticles used in the presented work needed a similar treatment as titania. Barium titanate nanoparticles were synthesised in ethanol solution. After the synthesis they were strongly agglomerated. Even long treatment in a sonication bath did not disperse the particles strongly enough to use the dispersion for spin coating. Experiments of spin coating the as-prepared $BaTiO_3$ solutions after treatment in the sonication bath for about one hour did not yield the results needed. The layers always contained a lot of satellites, which are big agglomerates

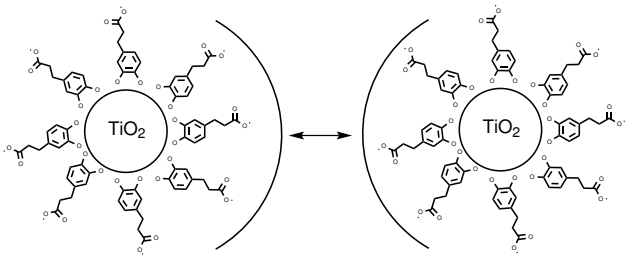

Fig. 7.3: Scheme of 3,4-dihydroxy hydrocinnamic acid at the surface of nanoparticles.

of nanoparticles forming huge defects in the layers. In figure 7.4, a SEM image of a spin coated 10BL PMMA-$BaTiO_3$ layer from a $BaTiO_3$ solution without any treatment after the synthesis is shown.

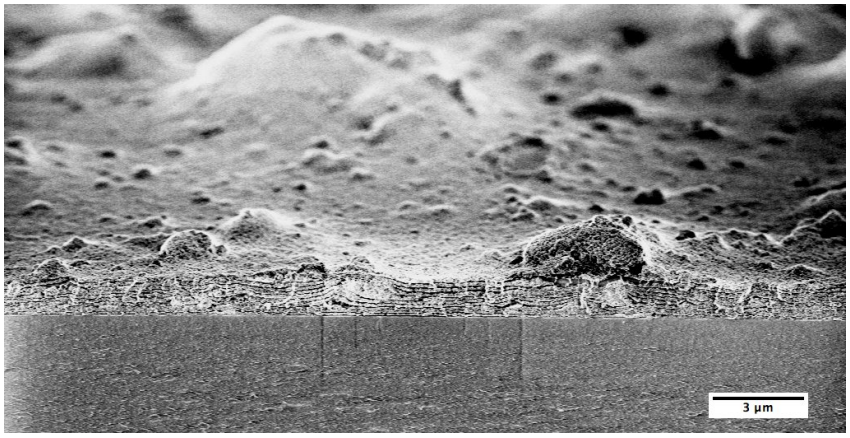

Fig. 7.4: Cross-sectional SEM image of a 10 BL PMMA-$BaTiO_3$ SL containing satellites.

These satellites could not be removed using the same methods as for the TiO_2 solutions. Here we needed to first remove bigger agglomerates through centrifugation, before we were able to filter the solutions through syringe filters. The first step to prepare the $BaTiO_3$ solutions for spin coating was a slow centrifugation step of the freshly prepared nanoparticle solution at 1000 rpm for 10 min. The resulting precipitate was removed form the nanoparticle solution and the remaining nanoparticles in the solution were filtered through syringe filters beginning with a pore size of 3 µm. Because the particle solution still contained some smaller agglomerates, the solution was filtered multiple times through the same 3 µm syringe filter and in a final step through a 0.8 µm pore sized filter. Compared to the TiO_2 particle solution in the $BaTiO_3$ solution many $BaTiO_3$ particles were retrained in the filter, so that the concentration of the particle solution was determined after the filtering process. $BaTiO_3$ nanoparticles were always used from ethanol solution, and because ethanol has a good wetting ability, there was no need to add further additives for homogenous coatings.

A third nanoparticle solution used in this work was Ludox solution from Sigma-Aldrich (LUDOX AS-30 colloidal silica 30 wt. % suspension in H_2O). This solution was used as purchased, diluted to the desired concentration, 100 µL of 10 wt. % SDS

solution was added to 10 mL of the Ludox solution and after a 10 min treatment in the sonication bath, the solution was filtrated through a 0.45 µm syringe filter and used for spin coating. In the Ludox solution, the SiO_2 nanoparticles are stabilised already so no further treatment before spin coating was needed.

Tab. 7.1: Nanoparticle concentrations used for a layer thickness of about 50 nm. (To 5 mL of the TiO_2 and the SiO_2 solutions 500 µL of 10 wt % SDS solution was added.)

Nanoparticles	Layer thickness [nm]	Concentration [g/L]
TiO_2	50	60
SiO_2	50	33.5
$BaTiO_3$	50	20

7.2.2 Polymer Solution

To spin coat polymers is easier than to spin coat nanoparticles. The most important point is to find a good solvent for the polymer, so that the polymer chains are well dissolved and do not form big secondary structures in the solvent. Here the molecular weight of the polymers plays an important role. For PMMA in toluene a molecular weight of about 35 k g/mol was used. While for poly (dopaminacrylamide) and poly(2-vinyl pyridine) (P2VP) a molecular weight of 15 to 20 kg/mol was used. Because the polymers were all dissolved in organic solvents, which have a low surface tension, there was no need to add additives to the solution. If the concentration of the polymer is too high, the spin coating solution becomes too viscous. A highly viscous solution is difficult to spread over the substrate and therefore not ideal for spin coating. If a highly viscous solution needs to be spin coated, the substrate has to be covered completely before starting the spin coater and the spinning speed needs to be enhances and longer spin coating time needs are required. To spin coat relatively thick layers, viscous solutions have to be used. But the reproducibility of layer thicknesses is not as reliable when using highly concentrated solutions. In this work usually polymer solution in toluene was used. The concentration was depending on the desired layer thickness between 1 wt % and 3 wt%. All polymer solutions were filtered trough a 0.2 µm syringe filter before spin coating and all solutions were transparent. Slightly turbid solvents indicates poorly dissolved polymers and needed to be filtered once more.

8 Characterisation

8.1 Optical Characterisation

The photonic band gap was identified using a simple spectrophotometer (Cary 5G 180-3300 nm). In a standardised method the absorption was measured from 300 to 1000 nm, if needed the wavelength region was adjusted. To confirm that the absorption is not caused by the building blocks the reflection was recorded using a integrating sphere. In the band gap region a maximal reflection/absorption was measured. All samples were measured on microscope glass and measured at least at 2 different spots to justify that the optical spectrum measured was identical over the whole sample and therefore confirm a homogenous spacing in the SL.

8.2 Mechanical Characterisation

The mechanical characterisation of the phononic crystals was done using a technique called Brillouin Light Scattering (BLS). This non destructive and non contact technique utilises the photo-elastic coupling between laser light and phonons. It is based on the inelastic scattering of monochromatic laser light from thermally activated phonons. This technique opens us the ability to monitor phonons in the giga Herz frequency range. The photons of monochromatic laser light probe thermal phonons in the phononic crystal. This interaction causes a frequency shift of the laser. The frequency shift of the light corresponds to the frequency of the probed phonons ($q_{[phonon]}=k_{[out]}-k_{[in]}$). A systematic image of the BLS process is shown in figure 8.1.

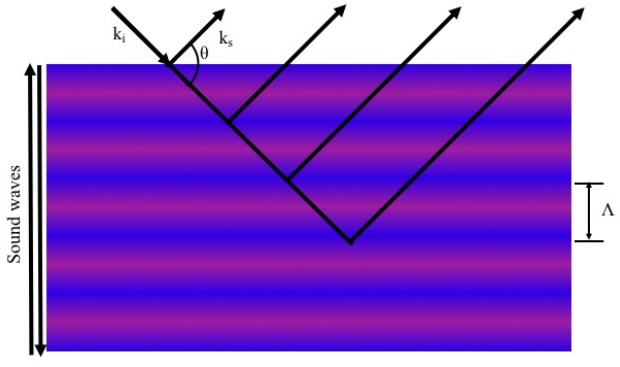

Fig. 8.1: A systematic image of the BLS process.

For the light waves with velocities of about $3 \cdot 10^8$ m/s acoustic waves with velocities of about 10^3-10^4 m/s seem like standing waves. Due to dielectric inhomogeneities

the acoustic waves with a wavelength of Λ can be treated as a periodic multilayered superlattice with the periodicity of Λ, on which the photos undergo multiple reflection. Interference of the reflected photons leads to a maximum intensity of phonons with the wavelength of $\lambda = 2n\Lambda sin\frac{\theta}{2}$. Where λ is the wave length of the photons, n is the refractive index of the medium, Λ the wave length of the phonons and θ is the scattering angle.

By applying the Bragg condition $q = \frac{4n\pi}{\lambda} sin\frac{\theta}{2}$ we can demonstrate that $q = \frac{2\pi}{\Lambda}$ and therefore it is equivalent to the wave vector k of the sound waves ($k = \frac{2\pi}{\Lambda}$). It follows that q directly depends on the scattering angel θ. The angular frequency of the incident photons (ω_i) undergoes a frequency shift through the inelastic scattering of the photons with the phonons, the scattered photons have a frequency of ω_s. Depending on the motion direction of the acoustic wave the with or against the direction of the light, the photon ether gains (Stokes shift) or looses energy (anti-Stokes shift). So the angular frequency shift of the shattered photons is equivalent to the angular frequency of the phonon $\omega_\mathrm{phonon} = |\omega| \equiv \omega_\mathrm{s} - \omega_\mathrm{i}$. With $\omega_\mathrm{phonon} = \omega = \frac{2\pi c}{\Lambda}$ giving the angular frequency of phonons in dependency of the velocity of the acoustic wave (c) and the wavelength Λ of the phonon. The frequency of phonons can be calculated from the angular frequency by: $f = \frac{\omega}{2\pi}$. Knowing this, it can be easily understood that the the frequency of the phonons undergo a Doppler shift ($f_\mathrm{s} = f_\mathrm{i} \pm \frac{cq}{2\pi} = f_\mathrm{i} \pm \frac{c}{2\pi}\frac{4\pi n}{\lambda} sin\frac{\theta}{2}$). With plus corresponding to the anti-Stokes process (waves propagate toward the direction of the detector leading to an increased phonon frequency) and minus describes the Stocks process (motion of acoustic waves way from detector yielding in a decreased phonon frequency).

The BLS spectrum gives us a doublet corresponding to the two angular frequencies (Stocks and the anti-Stocks) of the phonons $\omega = \omega_\mathrm{s} - \omega_\mathrm{i} = \pm cq$.

8.2.1 BLS Setup

The experimental setup of a Brillouin light scattering experiment is shown in figure 8.2. It consist of a monochromatic laser, a rotating sample holder, and a Tamdem Fabry-Perot Interferometer (FPI). A detailed description of the working principal can be found elsewhere.[120,121].

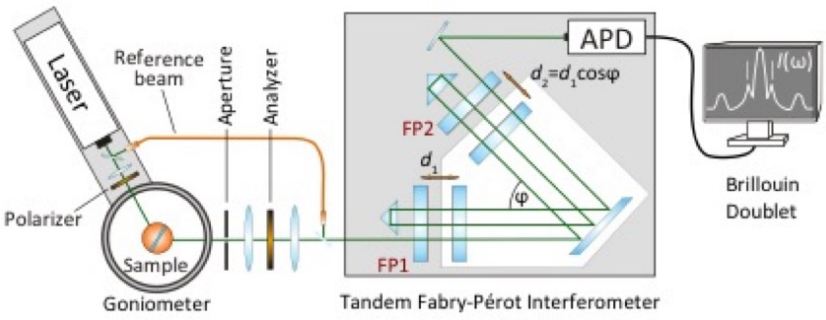

Fig. 8.2: Scheme of the experimental setup of the BLS experiment.[121]

As mentioned above the measurement is based on the opto-elastic effect of photons with phonons. Because frequency shifts need to me monitored with a very high resolution a high quality TFP interferometer is needed to be able to resolve the frequencies. The laser used for experiments in this work was a solid-state diode-pumped single-mode laser with a wavelength of λ=532 nm (Coherent, Compass 315M 70 mW). This laser is placed on a goniometer arm, which makes it possible to measure different scattering angels θ ranging form 5 to 150° and measure in different scattering geometries (see below). Before the laser beam passes the sample it passes a Glan-Thompson polariser so only vertical polarised light reaches the sample which is fixed on the centre of the goniometer. After the sample the scattered light passes to another Glan-Thompson prism to selectively collect polarised and depolarised light. Before the scattered light enters the FPI it passes a pinhole with the size of 300 µm. The FPI resolves the frequency of the light and finally it reaches the avalanche photo diode detector (multi channel analyser 1024 ch) which gives a frequency resolution as a function of the free spectral ranges.

As mentioned before there are two different geometries in which we can measure the scattered photons. Both configurations are shown in figure 8.3. a) is the so called transmission geometry. Here the scattered photons are detected after passing through the sample. This geometry has the advantage of being independent from the refractive index n. And for the special case $\theta = 2\alpha$ the calculation of the $q_{\parallel}$ gets very easy: $q_{\parallel} = \frac{4\pi}{\lambda} sin\frac{\theta}{2}$.

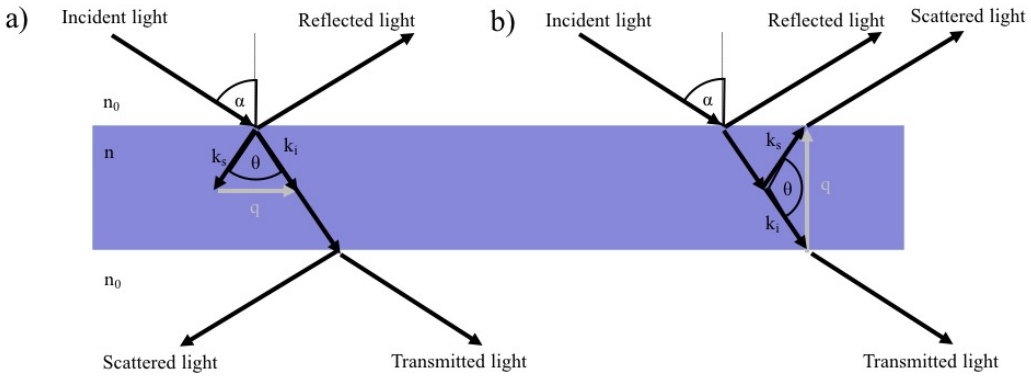

Fig. 8.3: The two different scattering geometries used for BLS measurements. a) Transmission geometry and b) reflectivity geometry.

For the scattering geometry shown in figure 8.3b), the reflective mode $q_{\perp}$ is give by: $q_{\perp} = \frac{4\pi n}{\lambda} sin[\frac{1}{2} arcsin(\frac{sin\alpha}{n}) + \frac{1}{2} arcsin(\frac{sin(\theta+\alpha)}{n})]$, for $\alpha = \frac{180-\theta}{2}$ the probed wave vector is equal to $q_{\perp}$. This measurement mode is therefore dependant on the refractive index of the measured material.

BLS experiments are a powerful and advanced tool to characterise the phononic band structure of one, two and three dimensional nanostructured materials. In the context of this thesis all BLS measurements were conducted by Elena Alonso-Redondo from the Butt group (group leader Georg Fytas) at the MPIP.

8.3 Structure of the Samples

The structure of the SL was investigated by using low voltage scanning electron microscopy (LVSEM). The following section gives an introduction to the sample preparation as well as the advantages of the LVSEM technic, the setup of the SEM used in this work and experiment parameters.

8.3.1 Sample Preparation

The SL were prepared on 2x2 cm glass substrates or Si-wafers (see chapter 7) and characterised by cross-sectional SEM imaging. For the preparation a sample for the measurements, the substrate was scratched with a glass cutter on the top side of the sample. The cut was only done on one side of the sample and it was a few milli meter long (see figure 8.4b). Next the samples was pressed onto the breaking-device in the manner that the cut was in the middle of the spike. And then pressure was exerted equally onto both sides of the substrate using two thumbs (see figure8.4c). The breaking device is shown in figure 8.4a. Basically it is a metal block with a spike in the middle of the block to get an edge for breaking the glass in a straight manner. The broken pieces were put onto the cross-sectional holder for SEM imaging (see figure 8.7 below). The breaking edge facing the electron beam.

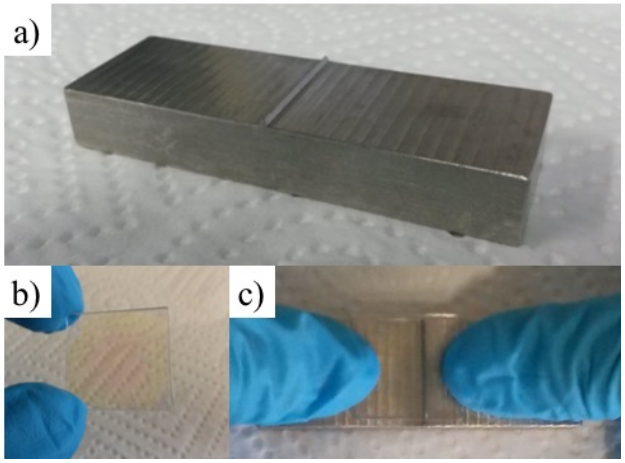

Fig. 8.4: SEM sample preparation: a) The breaking device. b) A scratched glass substrate. c) Phtot of a sample being broken.

8.3.2 Advantages of Low Voltage SEM

The challenge for the SEM imaging of the SL is that they are composed of non-conducting hybrid materials from inorganic nanoparticles and electron sensitive polymers. With the conventional SEM using electron beams from 5-35 kV the structure of the samples would get completely destroyed, meaning the polymer would disappear due to radiation damage of the beam. This effect could be minimised by sputtering the sample before the imaging process with a protective layer of gold or platinum. In figure 8.5 a sample of a PMMA-$BaTiO_3$ SL is shown. On the left side an image taken with a conventional SEM with a electron acceleration beam of 15 kV

can bee seen. The sample was sputtered with platinum before imaging. On the right side of that figure the SEM image taken with a low voltage SEM at 700 V is shown.

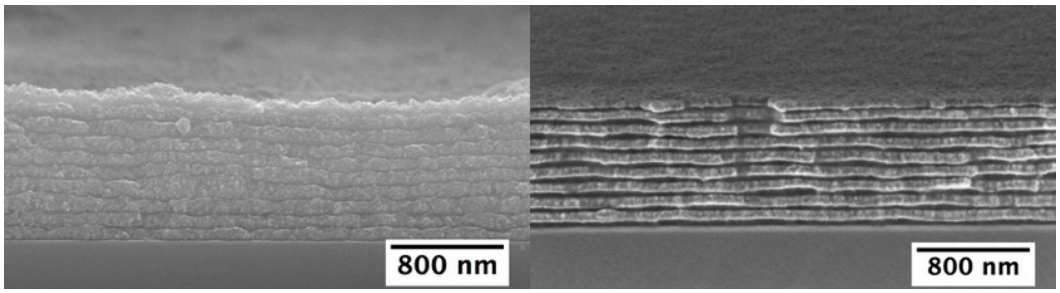

Fig. 8.5: Comparison between a cross-sectional SEM images of a 10 BL PMMA-$BaTiO_3$ SL measured at a conventional SEM at 15 kV (left side) and being measured at a LVSEM at 700 V (right side).

There are two aspects we need to consider. First the left side SEM image is taken from 90 degree top view, while the LVSEM image is taken under a tiled angle of 75 degree (see figure 8.7). This makes the whole stack appear thinner even though it is not. What can be observed as well is that the ratio from inorganic (light colour) to polymer (black) ratio is clearly higher for the conventional SEM image. This is caused by radiation damage of the polymer under the beam. While measuring the sample it is possible to observe a reduction of the polymer layer thickness even thought the sample was sputtered with a protective layer of platinum.

The low voltage SEM technique using typical acceleration voltages below 5 kV, has several big advantages compared to the conventional SEM.[122,123] It opens the possibility to image non-conducting samples, while minimizing beam induced radiation damage of the sample and reducing the charging of the sample during the imaging process. An important step for the development of the LVSEM technology was the development of the field emission gun (FEG) as an electron source. This electron gun has a high brightness while keeping a small spot size and a low energy spread. This allows a high resolution at low voltages.

In this work a LEO 1530 Gemini LVSEM from Zeiss was used. As electron source it has a FEG and the secondary electrons are detected by an in-lens detector (see figure 8.6).

The advantages of the Gemini column is that due to its positively charged biased booster, which shifts the energy of the primary electrons, the aberrations are minimised and the sensitivity to interfering stray-fields are reduced. Further the positively charged biased booster takes care that the secondary electrons emerging from the sample reach the in-lens detector safely. The beam is focused by a combination of magnetic and electrostatic retarding lenses and gets decelerated to the desired primary energy only shortly before it hits the sample, which is placed below the column. That makes it possible to image magnetic samples as well.

Using this LVSEM it is possible to image the SL without any sputtering before imaging, thereby avoiding a thick protecting layer on the sample via sputtering. The

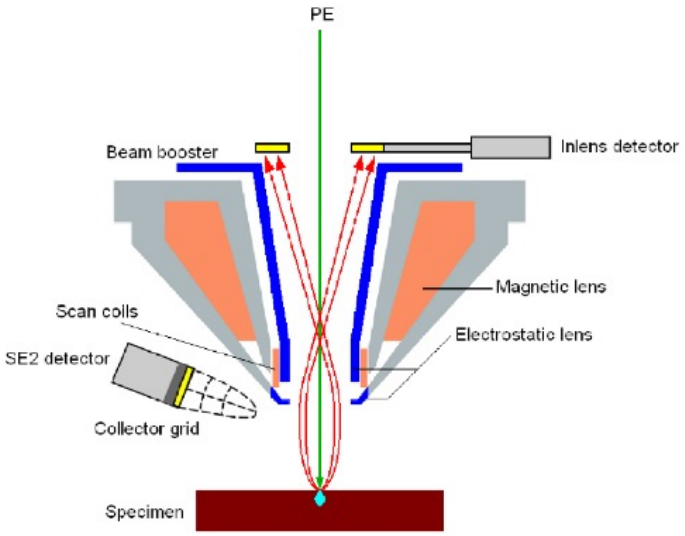

Fig. 8.6: Systematic sketch of the Gemini column.

LVSEM allows us to directly image the surface of the sample without destroying the polymeric layer and without a heavy charging of our non-conducting sample.

8.3.3 Imaging Conditions

For imaging the SL an acceleration voltage of 700 V was used. The cross-sectional sample holder is shown in figure 8.7. The sample was fixed onto the 75 ° tilted surface of the sample holder with a carbon tape. To minimise the charging of the sample it was mandatory to remove all air between the glass substrate and the carbon tape. Depending on the morphology of the sample a working distance from 2 mm to 1.5 mm was chosen, while for top view imaging a typical working distances was around 3 mm. The lens chosen was either a 30 µm or the 20 µm aperture lens. For obtaining high quality images the line average noise reduction mode was used.

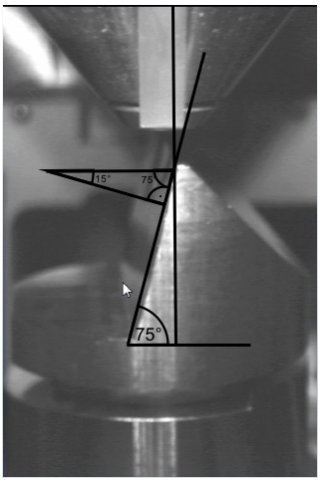

Fig. 8.7: Photo of the 75°-tiled sample holder for cross-sectional SEM imaging.

9 Pho(X)onic Superlattice

This chapter is taken from: Huesmann Huesmann*, Elena Alonso-Redondo*, El-Houssaine El Boudouti,Wolfgang Tremel, Bahram Djafari-Rouhani, Hans-Jürgen Butt and George Fytas, ACS Appl. Mater. Interfaces 2015, DOI 10.1021/acsami.5b01247. (*equal contribution) and additional comments have been added.

9.1 Abstract

We studied experimentally and theoretically the direction-dependent elastic and electromagnetic wave propagation in a supported film of hybrid PMMA (poly[methylmethacrylate])-TiO_2 superlattice (SL). In the direction normal to the layers, this one-dimensional periodic structure opens propagation band gaps for both hypersonic (GHz) phonons and near-UV photons. The high mismatch of elastic and optical impedance results in a large dual pho(X)onic band gap. The presence of defects inherent to the spin-coating fabrication technique is sensitively manifested in the band gap region. Utilising Brillouin light scattering, phonon propagation along the layers was observed to be distinctly different from propagation normal to them and can, under certain conditions (SL thickness and substrate elasticity), reveal the nanomechanical properties of the constituent layers. Besides the first realisation of unidirectional pho(X)onic behaviour, hybrid (soft-hard) periodic materials are a promising simple platform for opto- acoustic interactions and applications such as filters and Bragg mirrors.

9.2 Introduction

Properties of periodic nanocomposites differ from those of their bulk constituents. The flow of elastic and electromagnetic waves is drastically altered by the presence of alternating dissimilar impedances in composite structures. The destructive interference along the periodicity direction opens frequency band gaps that prohibit wave propagation. This property can be exploited to develop and customise materials with designed mechanical and optical characteristics. Potential applications of periodic structures include their use as Bragg reflectors for non absorbing laser cavity mirrors as humidity and liquid sensors[6,124] or for thermal management.[125–127] In particular, polymer composites are attractive because of their elasticity, transparency and easy fabrication. Despite the closeness of the refractive indices, photonic applications incorporating polymers are well-established. For example, this is the case of the microsegregated block copolymers.[6],[128],[129] Yet, to function as phononic materials, a sufficiently large elastic impedance $Z = \rho c$ mismatch (involving two

physical quantities, density ρ and sound velocity c) is required for a sizeable band gap.[15,20,130,131] Inorganic materials are frequently used to boost the impedance mismatch for a designed phononic and photonic crystal.[132],[16] One-dimensional (1D) crystals facilitate the study of elastic wave propagation because of the vector character of the latter. The majority of experimental investigations deal with inorganic materials such as Si, GaAs, AlAs or Au because molecular beam epitaxy, sputtering or lithography allow for good control over sample thickness and defects.[133–138] In particular, 1D crystals with periodicity normal to the substrate, termed superlattices (SLs), promote both phononic and photonic band gaps. Expansion to hybrid SLs with one soft polymeric phase enlarges the range of elastic impedance. For example, SLs consisting of alternating poly(methyl-methacrylate) (PMMA) and porous silica (SiO_2) nanoparticle layers fabricated by spin coating have advanced our fundamental knowledge in small scale phononics.[15],[16],[17] The cavity and surface modes as well as their interaction when varying the thickness and the position of the cavity layer were identified by the full theoretical description of the phononic density of states (DOS) recorded by Brillouin light scattering (BLS). In general for SLs, the band gap at normal incidence depends on the c and ρ contrast between the layers. Replacement of the SiO_2 ($c_{SiO_2} = 5660\,m/s$, $\rho_{SiO_2} = 2400\,kg/m^3$) layer by TiO_2 ($c_{TiO_2,bulk} = 8440\,m/s$, $\rho_{TiO_2,bulk} = 3900\,kg/m^3$) should boost the elastic impedance. The phonon propagation in an almost symmetric TiO_2-PMMA SL with a lattice constant of 0.22 μm was earlier investigated with a photoacoustic technique.[139] In that study, the probed phonon wavelengths ($6 < \Lambda < 30$ μm) are much longer than the lattice constant, and fall within the long wavelength regime far from the band gap region. Hence, this earlier study of phonon propagation along the periodicity direction could not reveal phononic behaviour. Instead, the propagation normal to the layers yielded the effective medium elastic properties that unexpectedly resemble those of the PMMA layer. To achieve large phononic and photonic band gaps, we fabricated a PMMA-TiO_2 SL by spin-coating subsequent layers on a glass substrate. We have chosen a spatial periodicity of d $\approx$100 nm and probing phonon wave vector q, with qd $\approx$ 1. The periodicity was selected to achieve dual band gap, a near-UV photonic and a hypersonic (GHz) phononic. Also, we probed phonon propagation normal to the periodicity direction using BLS, where no phononic gap but different effective medium behavior is expected. At the nanoscale, confinement and interface effects can render different effective material elastic properties than in the bulk. Experimental results along with theoretical band structure analysis allow a complete optical and nanomechanical characterization of the multilayer structure, thereby settling the necessary fundamental knowledge for applications. The paper is organized as follows: in Section A, we present the structural characterization of the PMMA-TiO_2 SL. In Section B, we describe how the sound velocity of the constituent layers, measured by BLS, is estimated. In addition, we discuss the conditions under which the effective medium sound velocity of the SL can be obtained from the in-plane BLS spectra. In Section C, we provide the phononic band structure along the

periodicity direction and demonstrate the phononic behavior both experimentally and theoretically. In Section D, we characterize the optical transmittance and photonic band structure of the SL, which confirms the dual gap for elastic and electromagnetic waves.

9.3 Results and Discussion

9.3.1 Design of Transparent SL

To fabricate our one-dimensional SL, we spin-coated 1D alternating bilayers of PMMA and TiO_2 nanoparticles, in total 20 layers on transparent SiO_2 glass substrate. The polymer used was PMMA (poly [methyl-methacrylate]) with a molecular weight M_w = 35 kg/mol, transparent for the wavelengths of our study and thermally stable. TiO_2 (titania) nanoparticles were chosen because of the large impedance contrast with the PMMA; additionally, the transparency of the TiO_2 in the visible spectrum and strong absorption for the UV light represent advantageous attributes in order to create transparent films and protect the polymer from UV degradation. The diameter of the spherical TiO_2 nanoparticles is ∼7 nm, which allows (a) a good dispersion in the solvent for subsequent spin-coating and wettability and (b) several strata of particles, for a homogeneous inorganic layer. PMMA shows a good adhesion to the TiO_2 particles, essential for a stable multilayer composite without voids. The mismatch of elastic and optical properties is large for these compatible components, in comparison with other combinations of polymer and inorganic particles. For example, $LiNbO_3$ (refractive index n = 2.32) has no good to 40 ± 5 nm and 57 ± 7 nm, respectively, and hence the periodicity is d = 97 ± 6 nm. The shape and ordering of the layers is extended over large areas (Figure 9.1a). Because of the fabrication technique, there is a non-perfect alternation of the layer spacing in the SL (Figure 9.1b), however the bandgap was found to be robust to structural incoherence of few nanometers.[16] We have labeled in Figure 9.1b the two layers with marked differences, named cavities c_1 and c_2 with thicknesses 30 and 75 nm, respectively. The identification of these cavities is crucial in the theoretical representation of the phononic band structure (next Section C). The small roughness observed in Figure 1c are less than 10% and does not represent an obstacle to achieve large bandgaps, as reported previously.[16] Moreover, the probing spot size (50 μm) is much larger than the length scale of the roughness, affecting mainly the width of the experimental BLS spectra.

9.3.2 Constituent Layers and SL in-Plane Propagation

To characterise separately the elastic properties of the constituents, we fabricated additional single films of PMMA and TiO_2. The estimation of the sound velocities in the two constituent layers is necessary to reduce the number of adjustable parameters in the theoretical modelling of the phononic dispersion of the SL. We prepared PMMA and TiO_2 nanoparticle films drop casted from solution. The thickness of

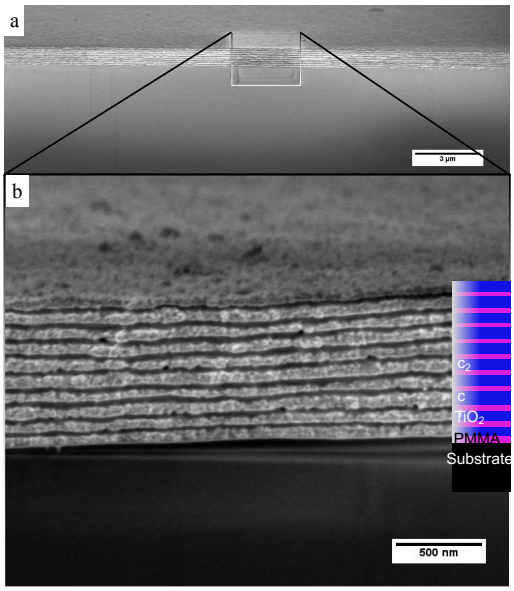

Fig. 9.1: a) Cross-sectional SEM micrograph of the 10-bilayer PMMA-TiO_2 superlattice. b) Schematic of the SL. The two cavity defects are noted as c_1 and c_2.

the films was in the micrometer range to measure bulk properties and avoid surface modes.[140–142] The dispersion relation in Figure 9.2, measured by BLS, is linear (i.e., purely acoustic) as expected for homogeneous films. The longitudinal sound velocity, obtained from the linear slope, amounts to $c_{drop} = 3390 \pm 40$ m/s in the TiO_2 drop casted and $c_{L,PMMA} = 2730 \pm 20$ m/s in the PMMA. The low c_{drop} relative to c_{TiO_2},bulk is due to the porosity of the TiO_2-drop casted film. In the fabrication of the SL by spin-coating, infiltration of PMMA is unavoidable and hence the c_{drop} value might not be the appropriate estimate of the sound velocity in TiO_2 sublayer of the SL.

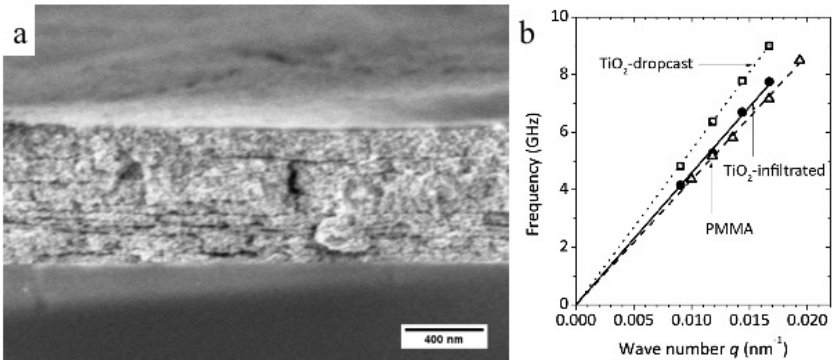

Fig. 9.2: a) Cross-sectional SEM image of the TiO_2-infiltrated film. b) Linear (acoustic) dispersion, frequency vs wave vector, for the longitudinal phonon in the TiO_2-infiltrated film (solid circles), TiO_2-drop casted (open squares) and PMMA (open triangles). The wave vector q is parallel to the film surface. The experimental error for the phonon frequencies amounts 1%.

To find a better representation of the TiO_2 layer in the SL, we prepared a third film by spin-coating subsequent layers of TiO_2 and a thin layer (1 wt%) of

PMMA, up to a total thickness of about 1 μm. PMMA is completely infiltrated in the TiO_2 layer, as confirmed by the SEM image (Figure 9.2a). In spite of the layering observed in the direction perpendicular to the substrate, this film appears homogeneous, because these local heterogeneities are much smaller than the phonon wavelengths ($\Lambda > 300$ nm). Hence a single purely acoustic phonon is observed (Figure 9.2b) yielding an effective medium sound velocity $c^*TiO_2 = 2900 \pm 50$ m/s. The infiltration of PMMA in the porous TiO_2 layer seriously impacts its sound velocity as compared to the $c_{TiO_2,bulk}$ of anatase crystal and even c_{drop} in the TiO_2-dropcasted. Therefore, the access to the experimental $c^*_{TiO_2}$ is crucial.

A similar drop is anticipated for the density $\rho^*_{TiO_2}$ of this layer that affects the elastic impedance. However, since this value can be hardly estimated without serious assumptions on the porosity and composition dependence of the mean density, we deliberately used $\rho^*_{TiO_2}$ as an adjustable parameter that sensitively enters the theoretical description of the SL band structure. From the representation of the experimental dispersion relation (Figure 9.3), we estimated $\rho^*_{TiO_2}$ = frequency f at the peak position increases linearly with $q_{||}$ (right panel of Figure 9.3a) yielding the longitudinal sound velocity $c_L = 2\pi f/q_{||} = 3010 \pm 40$ m/s. Unexpectedly, this value exceeds both $c^*_{TiO_2}$and c_L,PMMA of the infiltrated TiO_2 and PMMA layers and cannot represent the effective medium longitudinal velocity $c_{L,eff}$ of the SL. We note that for a similar SL (infiltrated SiO_2/PMMA),[16] c_L falls between the sound velocities of the two sublayers and a good agreement with $c_{L,eff}$ was reported. The latter can be theoretically estimated for an infinite PMMA-TiO_2 SL using essentially $c^*_{TiO_2}$ and $c_{L,PMMA}$ with minor effect of the corresponding transverse sound velocities (Table 9.1).[143]

Tab. 9.1: Physical quantities of the 10-Bilayer PMMA-TiO_2 superlattice constituents and substrate used in the theoretical calculations[a]. ([a]Density (ρ), sound velocity (c_L), thickness (d) and refractive index (n). [b]Infiltrated.)

Parameter	TiO_2 layer[b]	PMMA layer	SiO_2 substrate
ρ (kg/m^3)	1900	1190	2480
c_L (m/s)	2900	2700	5660
c_T (m/s)	1800	1400	2350
d (nm)	57	40	1 mm
n	1.85	1.50	1.50

Indeed,the computed $c_{L,eff} = 2840$ m/s falls between the sound velocities of the constituent layers and is 6% smaller than the experimental c_L. Because of the finite size effect of the SL, a computation of the density of states (DOS) for the in-plane elastic excitations in the supported SL helped to identify the experimental acoustic mode. Below the transverse sound velocity $c_{T,SiO_2} = 3250$ m/s of the substrate, there are two types of Rayleigh modes: one localised at the surface of the SL with sound velocity 1420 m/s (slightly below the mean $c_T \approx 1500$ m/s of PMMA and TiO_2) and the second localised at the surface of the glass substrate with c_R =

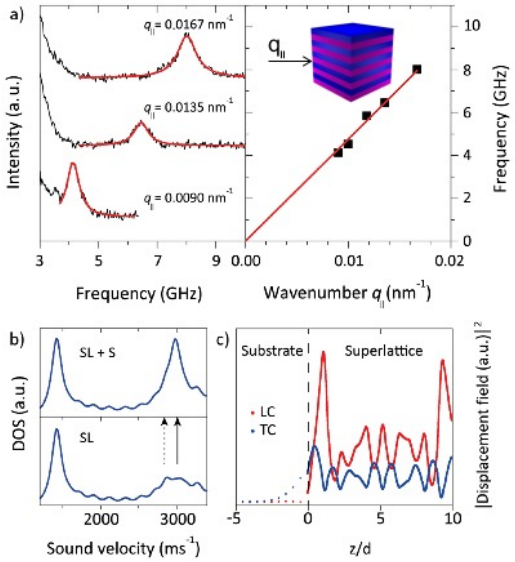

Fig. 9.3: a) BLS spectra recorded parallel to the substrate (normal to the periodicity) at three wave vectors $q_{||}$ as indicated in the plot. The spectra are well-represented by a single Lorentzian shape (red line) and the peak frequency is plotted against $q_{||}$ in the right panel. The pure acoustic nature of the phonon is indicated by the solid red line. b) Computed total density of states (DOS) integrated over the thickness of SL and substrate (top) and only in the SL (bottom). The two arrows indicate the frequencies of the experimental longitudinal sound velocity c_L = 3010 m/s phonon (solid) and the computed effective medium sound velocity $c_{L,eff}$ = 2840 m/s (dashed) at $q_{||}$ = 0.0167 nm^{-1}. c) Square modulus of the displacement fields of the acoustic modes around 3000 m/s in the supported SL with longitudinal (LC, red line) and transverse (TC, blue line) components of the polarisation against the dimensionless z/d position.

3000 m/s (slightly below c_{T,SiO_2}). In addition, there are several discrete (or standing) modes confined in the SL. The calculation of DOS and displacement field for the present SL, shown respectively in panels b and c in Figure 9.3, was performed using the densities and sound velocities listed in Table 9.1 1.32 Figure 9.3b gives the DOS vs the sound velocity at $q_{||}$ = 0.0167 nm^{-1}, with (upper panel) and without (lower panel) the contribution of the glass substrate. The upper panel shows good agreement with the Brillouin spectra (Figure 9.3a), where the SiO_2 Rayleigh mode dominates the other SL guided modes. The lower panel shows a broad peak where the increase of DOS around the frequencies of the effective medium acoustic phonon ($c_{L,eff}$ = 2840 m/s, dashed arrow) is associated with the longitudinal guided mode (LGM)[144],[145] Indeed, an analysis of the displacement field of this mode (Figure 9.3c) clearly shows that it is confined in the SL region and decreases exponentially in the substrate. Also, its longitudinal component (red line) is predominant in comparison with the transverse component (blue line). From a comparison between Figures 9.3a and b, and the fortuitous proximity of the values of c_R (= 3000 m/s) and $c_{L,eff}$ (= 2840 m/s), one can deduce the experimental c_L (= 3010 m/s) bears both contributions, rendering their discrimination ambiguous. Thus, the experimental c_L for in-plane propagation cannot be uniquely associated with the elastic properties of the two layers of the SL and is not free of substrate effects.

In the earlier investigation of the in-plane phonon propagation for a PMMA-TiO_2 SL, also on glass substrate, two dispersive phonons were resolved in the long wavelength limit ($q_{\parallel}d < 1$) using a photo-acoustic technique.[139] Their dispersion in the multilayer structure was described assuming it was a single uniform layer with effective sound velocity 2870 m/s, being closer (15%) to the sound velocity in PMMA (2490 m/s[17]). In this low $q_{\parallel}$ range, the access to two dispersive elastic excitations allows the estimation of effective sound velocity, subject to the assumption of a uniform single layer. In the same context, the measured sound velocity 3020 m/s for a SiO_2-PMMA SL supported on glass substrate is very close to the effective value[16] and is affected to a lesser extent from the substrate because of the higher sound velocity of the SiO_2 nanoparticle phase c_{L,SiO_2} (= 3100 m/s) exceeding the c_R of the glass.

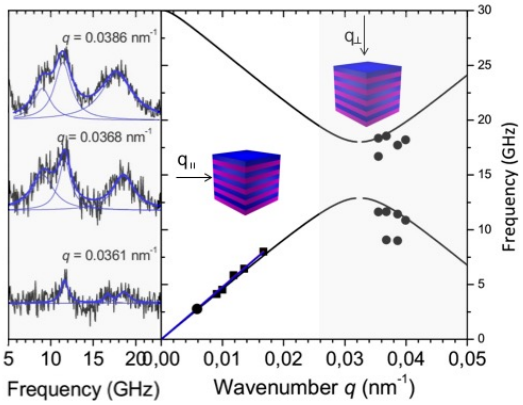

Fig. 9.4: Left: BLS spectra recorded perpendicular to the substrate (parallel to the periodicity) at three wave vectors $q_{\perp}$ indicated in the left panel. Right: Dispersion relation for phonon propagation along the two orthogonal directions, parallel (squares) and perpendicular (circles) to the PMMA-TiO_2 SL layers. The dispersion for an infinite SL with $q_{\perp}$ is shown as a black solid line, whereas the blue solid line represents the linear (acoustic) dispersion for the in-plane propagation ($q_{\parallel}$) also shown in the right panel of figure 9.3a.

9.3.3 Hypersonic Phononic Band Gap (Normal to the SL)

Bragg interference band gap in SLs appears along the periodicity direction when the wavelength of the phonon propagating normal to the film is commensurate with the lattice constant, i.e., $q_{\perp}d \approx 1.10$ The BLS spectra recorded for $q_{\perp}$ values close to the first BZ, at $\sim\pi/d = 0.032$ nm^{-1}, deviate from the single peak structure of an effective medium acoustic propagation. Defect-free SLs display two-phonon branch structure at the Brillouin edge, whereas the presence of defects causes an increase of the number of resolved modes in the BLS spectrum.[17]

In fact, Figure 9.4 (left panel) shows that three Lorentzian shapes are necessary to represent the experimental BLS spectra and obtain the frequencies of the resolved modes at different wave vector modulus $q_{\perp}$. The dispersion along this direction reveals the anticipated Bragg-type phononic band gap centred at 15 GHz, with a bandwidth of ~5 GHz as shown in Figure 9.4 (right panel). The lower edge

of the band gap is related to a standing wave with nodes located in the softer material (PMMA); the maximum amplitude of the displacement field is located in the TiO_2 layer. The opposite applies for the upper edge of the band gap, connected to the standing wave with nodes in TiO_2. Additional modes in the phononic band diagram are unequivocally related to the structural defects in the SL and their unique identification requires theoretical modelling of both the band diagram and BLS spectra. The band structure is very sensitive to periodicity perturbations. The theoretical spectral shape considering the contribution of two cavity modes representing the defects is mapped in the contour plot of Figure 9.5, which accounts for the BLS intensity shown in a colour scale (arbitrary units). The ideal case of an infinite defect-free lattice is represented by a solid grey line (Figure 9.5a). For the theoretical modelling, we considered two defects in the third and fifth layers of TiO_2 with thicknesses $d^3{}_{c_1} = 30$ nm and $d^5{}_{c_2} = 75$ nm, and the elastic parameters given in Table 9.1. The square modulus of the displacement field at the frequencies of modes labeled $c_|1$ and c_2 is shown in Figure 9.5d. The maximum displacement occurs in the region of the considered defects, noted by dots in the position axis, and vanishes in the surface. Its frequencies are $f_{c_1}(f_{c_2})$ for the thin (thick) cavities with $f_{c_1} < f_{c_2}$. The two frequencies do respect the $f_c \approx 1/dc$ dependence,[17] but as they fall on two different branches they appear to violate this relation. The total DOS integrated over the thickness (Figure 9.55c) identifies these cavity modes, and determines the Brillouin intensity as visualised in the BLS spectra of Figure 9.5c at $q_\perp = 0.0368$ nm^1. The theoretical BLS spectrum is represented by Lorentzian functions broadened by convolution with the instrumental function (∼0.5 GHz).

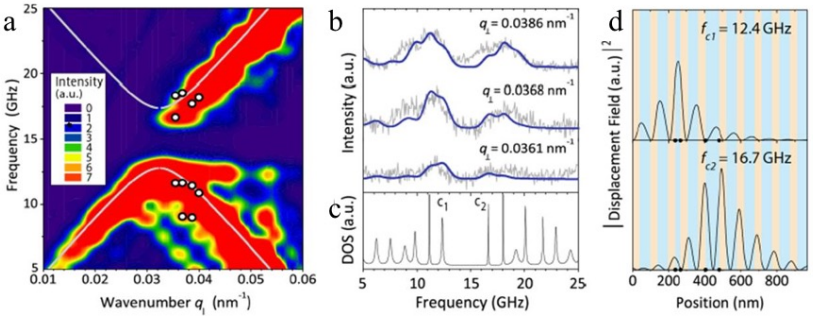

Fig. 9.5: a) Theoretical dispersion relation of an infinite SL (solid line) and Brillouin intensity, given as a colour scale, for the PMMA-TiO_2 SL considering two cavity defects. b) Theoretical (solid line) and experimental BLS spectrum for three selected wave vectors $q_\perp$ (along the periodicity direction). c) Total density of states (DOS), where c_1 and c_2 denote two cavity modes lying inside the band gap (d) Square modulus of the displacement fields of the two cavity defects. The points in the position axis denote the limits of the defects.

In addition to the band gap structure, the effective medium behaviour (low $q_\perp$ limit) along the periodicity direction is also predicted. The effective $c_{L\perp}$ can be obtained from the mean longitudinal modulus of the SL envisaged as a single uniform layer with $M_\perp = \rho {c_{L,\perp}}^2$, where ρ (= 1610 kg/m^3) is the mean density. Because the SL modulus $M_\perp$ obeys Wood?s law[146] its value is obtained from the

moduli of the constituent layers. Using the densities and the sound velocities of Table 9.11 and the volume fraction of the layers in SL, $M_{\perp}$ =11.8 GPa yielding $c_{L,\perp} = 2710$ m/s. Interestingly, the effective medium sound velocities along the two symmetry directions are not the same; $c_{L,\perp}$ is about 5 % lower than the in-plane $c_{L,eff}$ (= 2840 m/s). Assuming isotropic density, the effective in-plane elastic constant (C_{11}) is about 9 % higher than the out-of-plane (C_{33}) component, asserting the anisotropic nature of the elastic tensor of the SL.[143] Access to direction dependent mechanical properties is not possible with conventional rheology or atomic force microscopy (AFM), but requires elastic wave propagation selectivity, feasible through the vector nature of the BLS technique.[147] As in the case of PMMA-SiO_2 SLs,[16,17] both phononic band diagram and the experimental BLS spectrum are well-represented with two adjustable parameters (ρ*TiO_2 and ratio of elasto-optic constants (The ratio of elastic-optic constants for PMMA and TiO_2 was assumed as p_{PMMA}/p_{TiO_2} = 1.9.) using all elastic moduli fixed to the values of the constituent TiO_2 and PMMA layers; the assumed number of defects and thicknesses are in conformity with the SEM images. These two successful cases allow for a reliable prediction of the elastic wave propagation in 1D phononic structures.

9.3.4 Photonic Band Structure

Further characterisation of the SL was done via optical spectroscopy. When a monochromatic light is launched onto a periodic layered medium, with frequency in the range of the forbidden band gap, such a wave is evanescent and does not propagate through the medium. The energy is reflected, and the medium acts as a Bragg reflector. The peak reflectance for normal incidence occurs at the centre of the forbidden band, given by $\lambda = 2n_{eff}d$[148] In the present SL with an effective refractive index $n_{eff} = 1.71$ and lattice constant d = 97 nm, the peak should appear around 332 nm. Indeed, the photonic band gap was found experimentally in the range 315-360 nm (Figure 9.6a). As the films are supported by a glass substrate, a strong absorber in the UV region, experimental curves are affected by an error for $\lambda < 300$ nm. At the laser wavelength (532 nm) used in the BLS experiment, the SL is transparent (arrow in Figure 9.6a) allowing for optimal transmittance required for strong BLS signal. The modulation of the SL optical behaviour is noticeable in comparison to its constituents (dotted and dash-dotted lines), both being transparent in the visible.

To account for the band gap observed in the experimental transmittance, we have computed the photonic band structure of Figure 9.6b using the refractive indices $n_{PMMA} = 1.5$ and $n_{TiO_2} = 1.85$ for the constituent layers (Table 9.1).[149] We should note that n_{TiO_2} must be lower than the bulk anatase TiO_2 ($n_{TiO_2,bulk} = 2.5$) due to the infilled PMMA. We have estimated n_{TiO_2} from n_{eff}, n_{PMMA} and the TiO_2 fraction in the SL, assuming a linear dependence. The computed photonic band structure exhibits a gap in the region of wavelengths 310-350 nm. The band gap opens because of the large mismatch in the dielectric constant ϵ ($\epsilon \approx n^2$), or in other words, because of the difference in field energy location. At the edges of the band

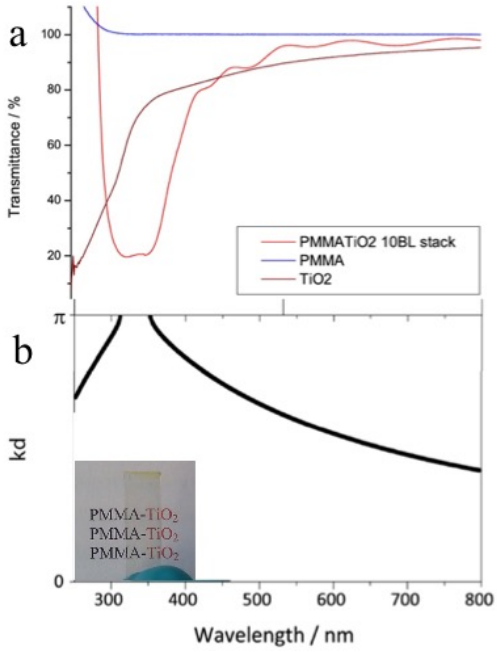

Fig. 9.6: a) UV/vis spectrum of the ten bilayer PMMA/$TiO_{2\ SL}$(red). The PMMA (blue) and TiO_2 nanoparticle (bordeaux) films are also shown with a distinct transmittance than the SL. The wavelength of the probing light (532 nm) is pointed by an arrow. b) Calculated band structure of the infinite SL. Inset: picture of the sample showing its transparency in the visible region.

gap, the majority of the energy is localised either in the PMMA (lower part of band 2) or TiO_2 (upper part of band 1). The gap located in the UV region blocks those wavelengths and lets the rest, e.g., visible light, pass through the structure as seen in the photograph (inset of Figure 9.6b). Thus, a unidirectional pho(X)onic behaviour (Figures 9.5a and 9.6) at different frequencies but with almost the same wavelengths for the elastic and electromagnetic waves is realised and justified for a hybrid SL.

9.4 Conclusion

We have studied by Brillouin light scattering (BLS) the elastic wave propagation in supported one-dimensional PMMA-TiO_2 multilayer structure (superlattice, SL) along and normal to the periodicity direction. The isotropic wave propagation in the constituent layers becomes direction dependent in the SL, with rich dispersion frequency vs. wave vector relations. Normal to the periodicity (in-plane) phonon propagation depends on the elastic mechanical properties of the constituent layers but also on the glass substrate in the case of finite SL thickness. The observed acoustic mode is not necessarily identified with the longitudinal acoustic phonon of the effective SL medium, fully determined by the composition and properties of the constituent layers. Instead, it relates to the predominantly longitudinal guided mode (LGM) localised in the SL as reflected by the computed displacement fields of the propagating modes along the layers. Based on the density-of- states (DOS) calculations, the LGM frequency of this SL is higher than the frequency

of the effective medium phonon. The proximity of the two modes depends on the longitudinal sound velocities in the constituent layers relative to the transverse velocity of the glass and the thickness of the SL. Hence, the extraction of the material elastic properties from the experimental acoustic mode is not straightforward. For the elastic and electromagnetic wave propagation along the periodicity direction studied by BLS and optical reflectance, a dual large band gap in the hypersonic (GHz) and near UV frequencies is realised for the first time in hybrid SLs. Although the spin-coating technique provides a facile fabrication of SLs with large range of materials, however the structure coherence is low compared to semiconductor SLs using MBE fabrication. The width of the band gaps is rather robust to such thickness variation but distinct defects are manifested in the BZ edge as localised modes. The theoretical representation of the dispersion band diagram, as well as of the BLS spectra, allows the identification of cavity defects and the elastic properties of the constituent layers. Surprisingly, the sound velocity in the TiO_2 layer is marginally higher than in PMMA layer and hence the observed large band gap essentially reflects the density contrast. For the effective medium elastic modulus along the symmetry direction, a low ($\sim$9%) mechanical anisotropy is revealed.

This is the first realisation of a unidirectional pho(X)onic hybrid SL occurring at similar phonon ($\Lambda = 2\pi/0.032$ nm) and photon ($\lambda = 332/n_{eff}$ nm) wavelengths $\sim$200 nm, and complements the recent report on porous silicon SL.[133] However, in the present BLS experiment with a laser wavelength at 532 nm the phonon-photon coupling must be weak. To the best of our knowledge, there are only theoretical works on active 1D pho(X)onic structures.[150,151] The present experimental and theoretical study provides a thorough understanding of 1D pho(X)onic structures necessary to access fundamental concepts such as opto-acoustic interactions, phonon and photon confinement for sound amplification and Bragg mirrors. Alternative fabrications techniques such as direct ink writing[152] can be examined to further improve and extend the range of hybrid SLs, which is a step forward from the conventional semiconductor-based structures.

9.5 Materials and Methods

9.5.1 Nanoparticles

3,4-Dihydroxy hydrocinnamic acid (DHCA) functionalized TiO_2 nanoparticles were synthesised by hydrolysing 20.6 mL of titanium isopropoxide in 37 mL of Milli-Q water and stirring for 1 h. The resulting white precipitate was filtered and dried in air before transferring into a stainless steel autoclave containing 0.96 g of DHCA and 12.8 mL of 5 wt% tetramethyl ammonium hydroxide solution (TMAOH). The autoclave was sealed and heated to 120 °C for 6 h and 4.5 h to 195 °C. The particles are composed of the anatase phase with mass density of 3.9 g/mL.

9.5.2 Superlattice

To prepare the spin coating solution from the TiO_2 nanoparticles 6.78 mL of 14% NH_3 and 100 μL of 10 wt% sodium dodecyl sulfate were added to 3.22 mL of the as-prepared nanoparticle solution. Ten alternating layers of 2.2 wt% of PMMA (poly[methyl-methacrylate], Acros Organics) solution in toluene and TiO_2 solution was spin coated on a glass substrate (spin coating parameters: v = 5000 rpm, t = 20 s.; ACL = 5000 rpm/s), with a heat treatment of 100 $^{\circ C}$ for 15 min after each layer.

For the TiO_2-infiltrated film, we used the TiO_2 solution and a 1 wt% PMMA solution in toluene. The spin-coating procedure was the same as for the SL, with a total number of 13 layers of TiO_2, which amounts to a thickness of $\sim$1 μm.

9.5.3 Brillouin Light Scattering and Optical Spectroscopy

BLS is a noninvasive technique which utilises the scattering of an incident probing laser beam from thermally activated density fluctuations (phonons) in transparent materials along a certain direction. The probing wave vector direction is selected with the scattering geometry, and its wavenumber $q_{\parallel} = 4\pi/\lambda \sin(\theta/2)$ is dependent on the wavelength of the probing beam λ = 532 nm and the scattering angle θ for propagation parallel to the substrate plane. The probing wave vector $q_{\perp}(n)$ perpendicular to the substrate is depending on the refractive index, n, and the analytical expression can be found elsewhere.[16] The BLS spectrum for homogeneous materials consists of a double frequency shift ($\pm$f) at GHz frequencies, resolved by a tandem Fabry-Perot interferometer (JRS Instruments), whereas for structured materials, a more complex spectrum arises. The dispersion relation f(q) reveals much information such as sound velocity, effective refractive index, and avoided frequency regions (band gaps) in the GHz regime. The optical transmittance of the SLs was checked by an UV/vis spectrometer (Varian, Cary 5G UV/vis NIR spectrometer) at normal incidence.

9.5.4 Electron Microscopy

The morphology and microstructure of the SL were characterised by a scanning electron microscope (SEM, LEO Gemini 1530) at 0.7 kV. The measured thickness

of the PMMA (TiO_2) layers is 40 ± 5 (57 ± 7) nm. A deviation of this value is observable, especially in certain layers that are subsequently treated as defects, which are of special importance in the theoretical description of the band structure. Nanoparticles were drop-coated on a carbon-coated copper grid from an ethanol solution and measured with at acceleration voltage of 120 kV with a transmission electron microscope (TEM, JEOL 1400). Nanoparticles are spherical, with an average diameter of (7 ± 2) nm (Figure 9.7).

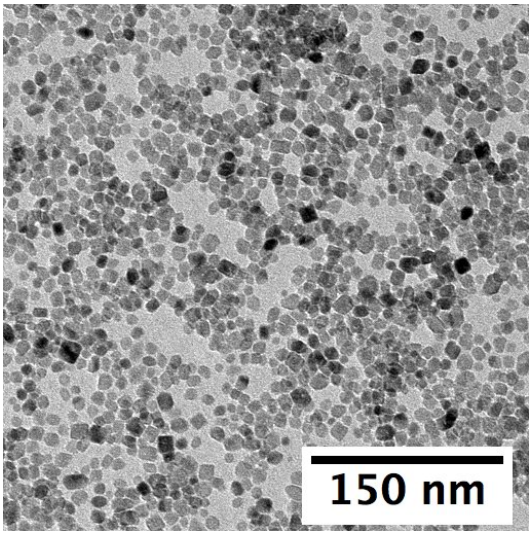

Fig. 9.7: TEM Image of the TiO_2 nanoparticles used for spin coating the SL.

9.5.5 Theoretical Modeling

The computation of BLS spectra is based on the calculation of DOS utilising Green?s function technique. The reader is referred to Supplemental Information of ref[17].

9.6 Additional Comments

As mentioned in section 9.3.2. the sound velocity of the titania layers in the superlattice are not well known but well approximated. The challenge is to know the actual composition of the layer. PMMA infiltration occurs for sure but to know the exact amount stays a challenge. There are different methods to analyse the compositions of layers. For example via ellipsometry or x-ray diffraction experiments. For ellipsometry we would need an exact layer thickness, which is difficult, because the single layers in the SL have a variation of about 5 %, this error can not extinguish. And during x-ray experiments the PMMA is damaged and degenerated and therefore an other inaccuracy rises. In conclusion the approximation made in the paper is equally correct.

To prove this further experiments on titania PMMA blends were conducted. Different mixtures of PMMA and titania nanoparticles with well-defined fractions of PMMA were prepared and the sound velocities of this blends were measured using BLS. The blend were prepared as follows. First a homogenous mixture of nanoparticles and PMMA in a solvent was prepared. This mixture was drop casted onto a glass substrate and after the solvent was evaporated at air the samples were transferred into a oven and heated for 30 min to 120 °C to remove the remaining solvent.

Figure 9.8 shows the measured sound velocity of the TiO_2-PMMA blends starting from a pure PMMA film to a pure porous TiO_2 film. The sound velocity rises parallel to the fraction of TiO_2 nanoparticles. This behaviour is expected, because the had TiO_2 is known to have a higher sound velocity than the soft PMMA. To confirm, that the blends show a homogenous distribution of polymer and nanoparticles cross-sectional SEM images of the 0.3 and 0.7 TiO_2-PMMA blends were taken. The images in figure 9.9 and 9.10 show, that the polymer and the nanoparticles are mixed well and that a adequate blend is achieved.

The absolute value of the sound velocity does not match exactly with the values of the sound velocity of the spin coated sample (2900 m/s), but this can be explained by the different fabrication method. During the drop casting fabrication method, the nanoparticles and the PMMA have time to pack well, while during spin coating the particles pack randomly and relatively more air in included into the film. Air voids reduce the sound velocity and therefore the lower sound velocity measured in spin coated sample in section 9.3.2 simulates the value of the sound velocity of the TiO_2 layers within the SL more accurate that the blends. This demonstrated that sound velocity of films does not only depend on the used materials but on the fabrication method as well. So the results on the blends only prove, that the used principal of the assumption of the sound velocity is right, but not the absolute value.

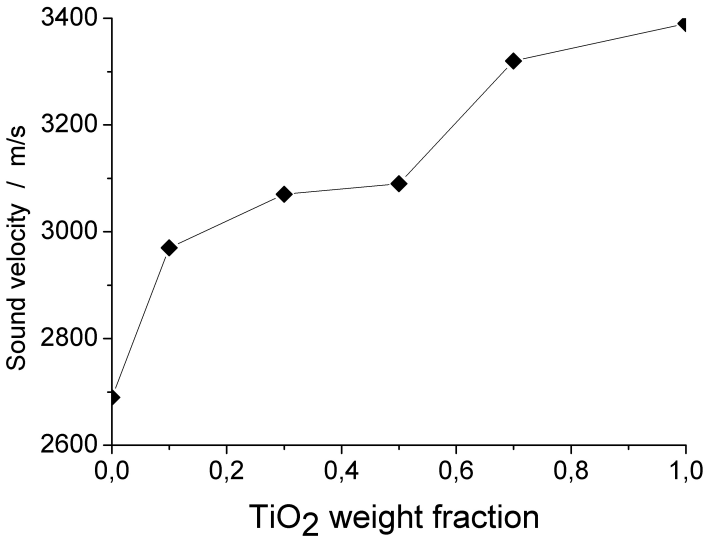

Fig. 9.8: Sound velocity of TiO_2-PMMA blends as a function of the TiO_2 weight fraction.

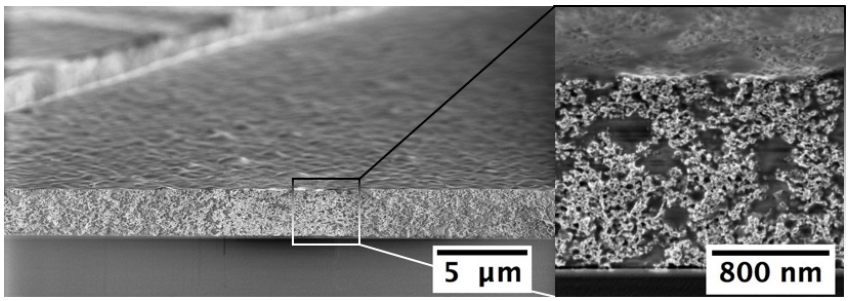

Fig. 9.9: SEM image of the TiO_2 PMMA blend with a TiO_2 weight fraction of 0.3.

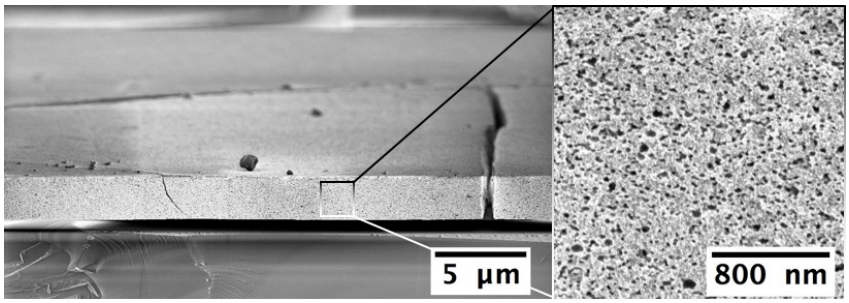

Fig. 9.10: SEM image of the TiO_2 PMMA blend with a TiO_2 weight fraction of 0.7.

9.6.1 Experimental details

For the fabrication of the blends a mixtures of the polymer and the TiO_2 nanoparticles were made as described in table 9.2. The used solutions were: NP: 2.2 wt% TiO_2 NP in TMAOH; PMMA: 20 wt% PMMA in ACN. Microscope slides were cut into 1x2 cm pieces and cleaned in hot piranha solution (H_2SO_4:H_2O_2 2:1) for 30 min. The glass substrates were afterwards washed with ethanol and heated to 450 °C for 2 h. 25 μL of the as prepared mixtures were spread onto a glass substrate by using a Eppendorf pipette and dried at air. After the samples seemed dry they were transferred into a 120 °C hot oven and kept there for 30 min to make sure no solvent would remain in the sample.

Tab. 9.2: Mixing protocol for the fabrication of the TiO_2 PMMA blends (* a 2.2 wt% PMMA solution in ACN was used).

TiO_2 weight fraction	NP / μL	14 % NH_3 / μL	ACN / μL	20 wt% PMMA / μL
0	0	0	0	25*
0.1	100	600	200	99
0.3	300	400	225	77
0.5	500	200	254	55
0.7	700	0	0	300*
1	25	0	0	0

10 PMMA-$BaTiO_3$ Superlattices

10.1 Introduction

In chapter 9, we demonstrated that it is experimentally possible to get so-called pho(X)onic crystals with dual photonic and phononic band gaps. In this chapter, we will try to push the limits of the optical and the mechanical contrast in the building materials of the SL. By increasing the refractive index of the inorganic building block, the photonic band gap is expected to shift to longer wavelengths. For the phononic band structure, a widening of the gap is expected when the elastic impedance difference is raised. To increase the refractive index and the elastic impedance, it is necessary to switch to other materials or find a method to improve the packing of the nanoparticles within the layer. It is relatively easy to substitute the titania nanoparticles. There are some suitable candidates. Barium titanate has a high refractive index of 2.38 and in a solid state a very high density of 6.02 g/cm^3. Therefore, it seems to be a very good candidate to push the contrast of the refractive index and the density in comparison to PMMA. Another approach is to use a softer or lower refractive index polymer than PMMA. But it is hard to find suitable polymers with significantly lower refractive indices or mechanically softer polymers which are still easy to process. In this chapter, two PMMA-$BaTiO_3$ SLs are introduced and characterized.

10.2 Results and Discussion

The PMMA-$BaTiO_3$ SLs were built up from commercially available poly(methyl methacrylate) and spherical $BaTiO_3$ nanoparticles. The synthesis of $BaTiO_3$ nanoparticles is described in chapter 6, spherical 7 nm-sized particles were used to build the SLs. They were fabricated using the spin coating technique, a detailed description of this technique is given in chapter 7. Here, two SLs are presented SL A is a SL with asymmetric layer symmetry, the PMMA layer is very thin while the $BaTiO_3$ layer is almost four times thicker. SL B is a SL with symmetric spacing with similar PMMA and $BaTiO_3$ layer thicknesses.

SL A shows a lattice constant of a = 106 nm, with an average layer thickness of 21 nm and 85 nm for the PMMA and the $BaTiO_3$ layer, respectively. SEM images of this SL are shown in figure 10.1a. It shows a good homogeneity over a large area, while the inset gives a more detailed image of the single layer structure. The PMMA layer (dark/purple) is homogenous, while the $BaTiO_3$ layers show a porous structure with small variations in thickness. Based on the earlier PMMA-SiO_2[16] and

PMMA-TiO_2[79] results, these small variations do not affect the properties of the SL dramatically. The optical absorption spectrum of SL A is presented in figure 10.1b. It exhibits a maximum at 419 nm. To prove that this peak is neither caused by the absorption of PMMA nor by the absorption of $BaTiO_3$ nanoparticles, the absorption of the PMMA and $BaTiO_3$ films are plotted below. The PMMA absorption (dashed line) as well as the $BaTiO_3$ nanoparticle absorption (dotted line) do not show any significant absorption in the wavelength range of interest. This proves that the absorption is caused by the structure of the SL and the maximum at 419 nm presents therefore the photonic band gap (PtBG) of the SL A. To get a better understanding of the optical properties, the Bragg-Snell law ($m\lambda_{Max} = 2(n_L \cdot h_L + n_H \cdot h_H)$), which is known to give a first hint of the expected position of the PtBG of 1D PtC, was applied. By using a refractive index of 1.5 for PMMA and 2.38 for $BaTiO_3$, the Bragg-Snell law predicts the band gap at 467.5 nm. This value is, considering the inaccuracy of the approximation, in good agreement with the PtBG found, knowing that the refractive index of $BaTiO_3$ is reduced due to infiltration of the PMMA into the $BaTiO_3$ layer. It is useful to calculate the refractive index utilizing the Bragg-Snell law in a reverse manner by putting the lattice spacing and the absorption maximum into the equation. This gives a refractive index of the $BaTiO_3$ layer of 2.09 and therefore a reduction of the refractive index of 12% compared to the value for the bulk material from literature. For the PMMA-TiO_2 SL a reduction of the refractive index of the TiO_2 layers of 25% was assumed.[79] Knowing that the refractive index of the nanoparticle layer was reduced due to the void space between the nanoparticles, the theoretically expected and the measured band gaps are in a very good agreement.

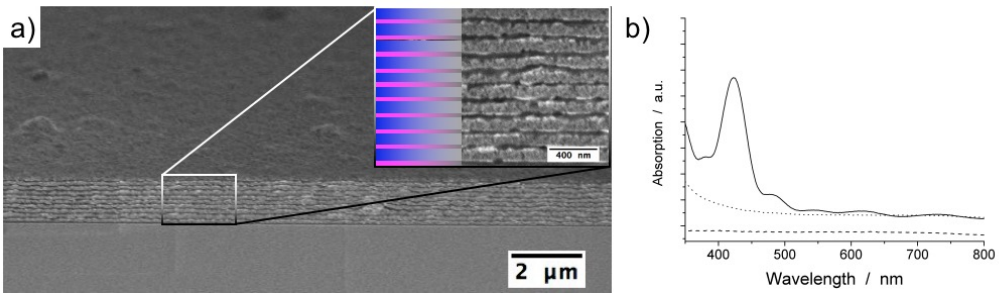

Fig. 10.1: a) Cross-sectional SEM images of the PMMA-$BaTiO_3$ SL A. b) UV/Vis absorption spectrum of the PMMA-$BaTiO_3$ SL A (solid line) and a PMMA film (dashed line) and a $BaTiO_3$ film (dotted line).

The phononic characterization of this SL was not trivial, a broad phononic band gap, as expected, could not be found (see figure 10.2). Instead, for SL A a surprisingly low average effective longitudinal sound velocity, an extremely low effective refractive index of 1.54 and a small band gap was found, when assuming a density of 1.5 for the $BaTiO_3$ layers. The average value for the longitudinal sound velocity is with 2570 m/s lower than the sound velocity of PMMA films (2700 m/s) and bulk $BaTiO_3$

(6200 m/s). In the range between $0.001 < q < 0.01$ / nm three dispersive modes can be identified. The low effective sound velocity, and the origin of the dispersive modes will be discussed below. Further, for $q_\perp$ a single mode was found, meaning that the evidence for a phononic band gap is not given. There is a possibility that the band gap still exist, but the lower branches cannot be detected due to low intensity.

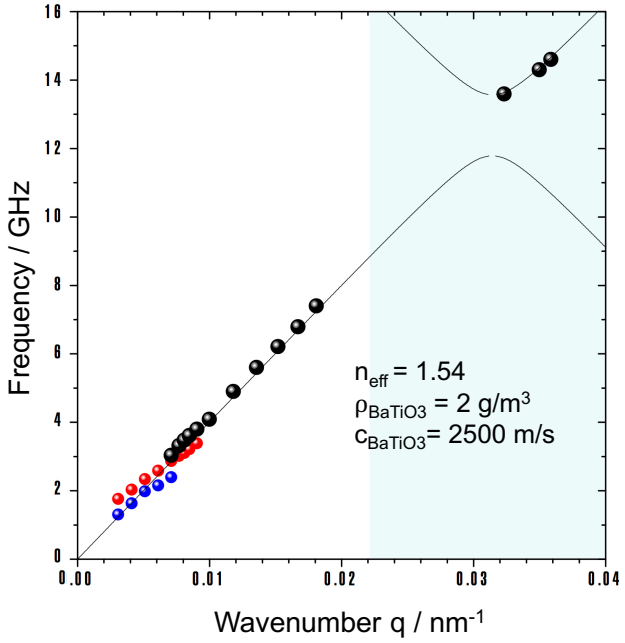

Fig. 10.2: Dispersion relation of the PMMA-$BaTiO_3$ SL A, dots measured values and black line calculated dispersion relation for an infinite SL with optimized values for the effective refractive index (1.54), density of the PMMA layers (2 g/m^3 and the sound velocity of the $BaTiO_3$ layers (2500 m/s).

It was suspected that the closing of the band gap was caused by the asymmetric layer spacing, therefore a symmetric PMMA-$BaTiO_3$ SL was prepared.

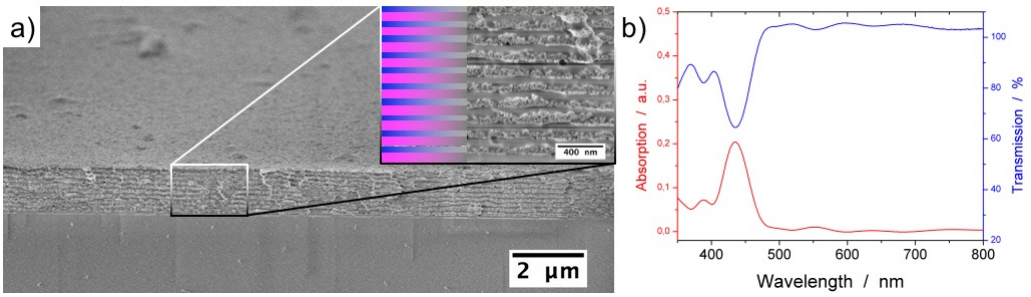

Fig. 10.3: a) Cross-sectional SEM images of the PMMA-$BaTiO_3$ SL B. b) UV/Vis absorption (red line) and transmission (blue line) spectra of the PMMA-$BaTiO_3$ SL B.

By reducing the concentration of the $BaTiO_3$ nanoparticles solution from 34 g/L to 20 g/L, the $BaTiO_3$ layer thickness was reduced from 85 nm to 63 nm. At the same time, the PMMA spin coating solution was concentrated from 2.0 wt% to 2.5 wt% which caused an increase of the layer thickness from 21 nm up to 70 nm.

An SEM image of the PMMA-$BaTiO_3$ SL B is given in figure 10.3a. With a lattice constant of a = 133 nm, the total thickness of the SL is higher, the layer thickness of the PMMA and the $BaTiO_3$ layer was measured to be 70 nm and 63 nm, respectively. The quality of the single layers is similar to SL A. Applying the Bragg-Snell law, a PtBG at 509.8 nm is expected. The optical transmission and absorption spectra of the SL B are shown in figure 10.3b. With the absorption maximum at 435 nm, the theoretical calculation is less precise than the calculation for SL A. This can be explained by a stronger infiltration of PMMA into the $BaTiO_3$ layer. If we have a closer look at the inserted SEM image in figure 10.3a, a strong infiltration of PMMA can be seen. The Bragg-Snell law, applied in a reverse manner to calculate the refractive index of the $BaTiO_3$ layers, yielded a refractive index for these layers of 1.79, meaning a reduction of the refractive index of 25%. This is a similar reduction as observed for the PMMA-TiO_2 SL in the previous chapter and due to a similar lattice spacing between these two SLs a reasonable value for the refractive index of the $BaTiO_3$ layers.

The phononic properties were investigated as well, but a proof for a phononic band gap could be found neither in the symmetric SL B nor in the asymmetric SL A. The dispersion relation of the SL B is given in figure 10.4. The same slow average effective longitudinal sound velocity and the dispersive modes for small scattering vectors q, as well as the low effective refractive index as in SL A were found.

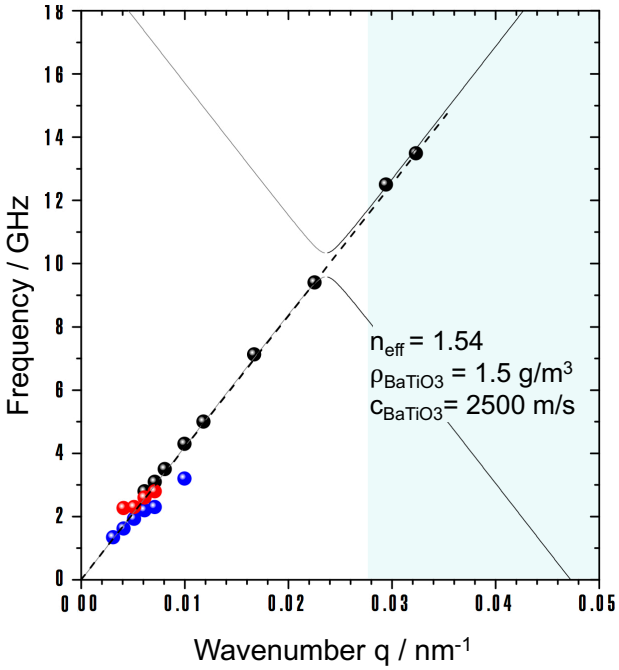

Fig. 10.4: Dispersion relation of the PMMA-$BaTiO_3$ SL B, dots: measured values, black line: calculated dispersion relation for an infinite SL with optimized values for the effective refractive index (1.54), density of the PMMA layers (2 g/m^3 and the sound velocity of the $BaTiO_3$ layers (2500 m/s).

As mentioned above, it is interesting, that in SL A and B for small $q_{\parallel}$ three dispersive modes are observed. These modes could correspond to the Lamb modes of the $BaTiO_3$ layers. In figure 10.5 the phase velocity ($2\pi f/q$) as a function of q is given. It is noteworthy, that this is the first time to detect these modes in the hybrid SL. In previous SLs (see chapter 9 and literature[16,17]) it was not possible to detect the signal of the Lamb modes. One possible reason for the appearance of these modes could be the extraordinary high density of the $BaTiO_3$ nanoparticles. The contrast between the density of the PMMA and the $BaTiO_3$ is much higher than in previous SLs and this could allow the detection of the lamb waves.

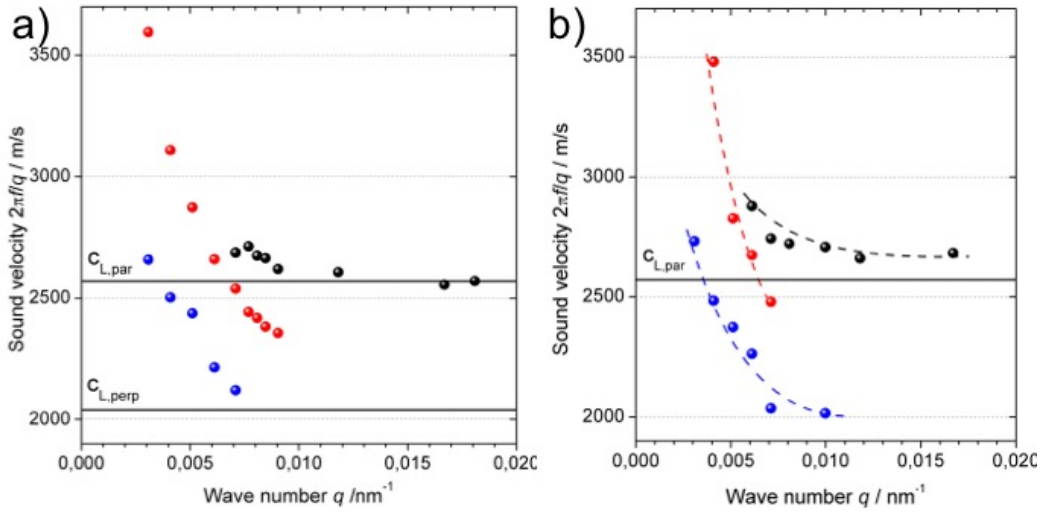

Fig. 10.5: Phase velocity ($2\pi f/q$) as a function of q, the dispersion of the modes in plane is revealed, a) for SL A, b) for SLB.

For a deeper understanding of the behaviour of the $BaTiO_3$ containing SLs, the properties of a single $BaTiO_3$ film were investigated.

To do so, a $BaTiO_3$ film with a thickness of 1 µm was prepared by repeatedly spin coating 14 layers of $BaTiO_3$. A laser microscope and an AFM image of the resulting $BaTiO_3$ film are shown in figure 10.6a and b. Using nanoindentation, the Young's modulus E of 3.28 ± 0.88 GPa was determined (see figure 10.6c). Further, the determination of the sound velocity of the same $BaTiO_3$ film was done by BLS measurements. Here too, a surprisingly low value for the longitudinal sound velocity of 1500 m/s was found, the corresponding dispersion plot is given in figure 10.6d. The low sound velocity of the $BaTiO_3$ film helps to understand the low effective sound velocity found in the SL A and B. Since the Young's modulus and the sound velocity of the $BaTiO_3$ film are known, we can extract, that the density of the $BaTiO_3$ film is higher than 1.46 ($M = \rho c^2 > E$). To know that the density has to be higher than 1.46 helps to know the dimension of the density values used for the calculation of the dispersion relation of the SLs.

This pure $BaTiO_3$ film gives a hint of the properties of the $BaTiO_3$ layer, but does not describe the exact reality. As mentioned before, the inorganic nanoparticle

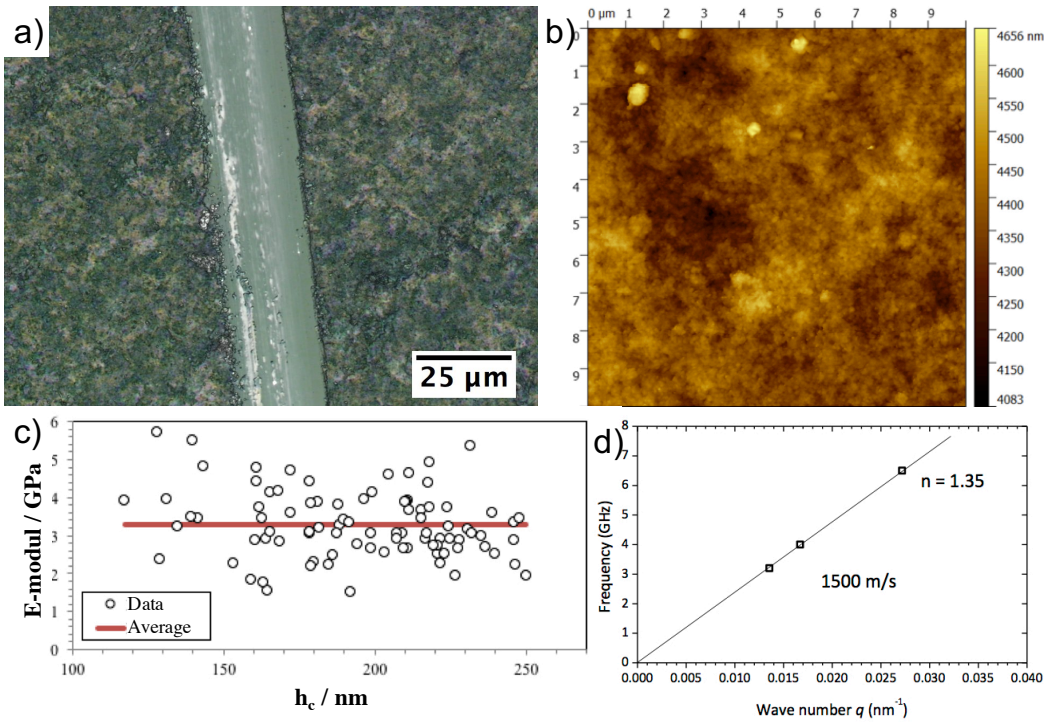

Fig. 10.6: a) Laser microscope image and b) AFM image of the $BaTiO_3$ film. c) Diagram of E-modulus vs. indentation depth nanoindentation, circles: measured data, red line: average over all data points. d) Linear (acoustic) dispersion plot of the $BaTiO_3$ NP film.

layers within a SL are infiltrated with PMMA. Thus, preliminary experiments on PMMA and $BaTiO_3$ blends were conducted. These experiments demonstrate how important the fabrication method, the post-fabrication treatments and the surface functionalization of the nanoparticles are for the properties of the films. Here, two batches of blends were fabricated using drop casting technique. The measured sound velocities for the two batches of PMMA-$BaTiO_3$ blends with different volume fractions are given in figure 10.7. The first batch of blends (squares) was prepared using a slow drying method with different heating steps. The second batch (triangles) were heated only once to a high temperature, therefore the solvent was evaporated fast. The difference in sound velocity can be explained by thinking about the different packings of a slowly and a quickly evaporated solvent sample. A slow evaporation of the solvent gives the nanoparticles time to arrange in a closely packed order, while a fast evaporation of the solvent means that the packing of the nanoparticles will not be as ideal, therefore more void space will remain in the film and the sound velocities will be reduced. Additionally, it should be pointed out, that the sound velocity of the drop casted (slowly dried) pure $BaTiO_3$ film is, with 2090 m/s, significantly higher then the sound velocity of the spin coated film (circle) (for the pure $BaTiO_3$ films a close packing of nanoparticles is assumed, thus, a volume fraction of 0.74). This gives a hint, that spin coated layers are not close-packed, but contain even more void space than drop casted films. Thus, to really exactly reproduce the layer composition within the SLs, the blends need to be fabricated using the same method

like the SLs, thus they need to be spin coated. The results on the blends presented here are preliminary results, at the moment this results are being reproduced to confirm their correctness. But in previous experiments with different blends, it was observed, that solvents, particle morphology, surface ligands and the fabrication method influence the sound velocity of the films tremendously.[153] In conclusion, the packing of the particles within the film and the contact of the particles to their neighbours influence the speed of sound in films.

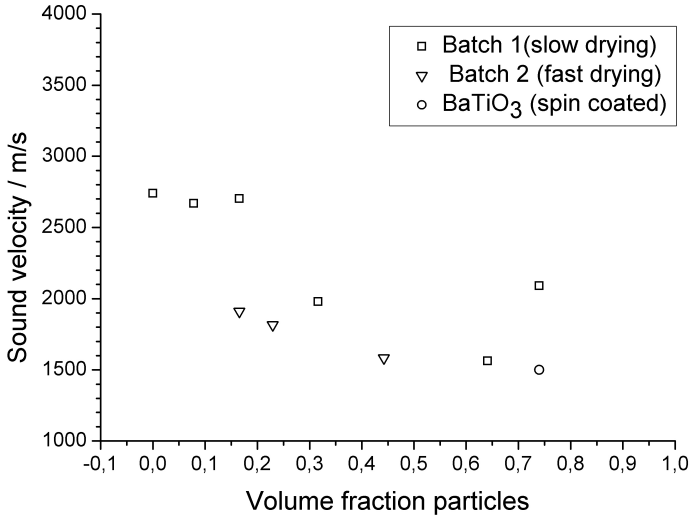

Fig. 10.7: Blot of the sound velocity vs. volume fraction of the PMMA-$BaTiO_3$ blends.

10.3 Summary and Outlook

The fabrication of PMMA-$BaTiO_3$ SLs was successfully demonstrated. By changing the concentration of the $BaTiO_3$ nanoparticle solution, the lattice spacing was well adjusted and controlled. The interpretation of the photonic behaviour of the PMMA-$BaTiO_3$ SLs gives a hint, that the $BaTiO_3$ layers within the SLs show a strong infiltration with PMMA. The pure $BaTiO_3$ film was found to exhibit a surprisingly low sound velocity, while the characterization of the blends revealed a strong influences of the experimental fabrication methods and the degree of infiltration on the sound velocities of the layer. The BLS measurements of the two SL showed unexpected behaviour. Instead of a broad phononic band gap, a small band gap was found, whereas the proof of the gap (lower branches for $q_\perp$) could not be found so far. The reason for the small gap might be connected to the low sound velocities of the $BaTiO_3$ layers. However it is not clear wether the fact, that $BaTiO_3$ is a ferroelectric and photorefractive material, and shows light induced absorption influence the BLS measurement. Because some questions remain open, the study of the PMMA-$BaTiO_3$ SLs is going on. At the moment, theoretical calculations of the UV-Vis absorption spectra as well as the phonon dispersion of the SLs are in preparation. From these calculations, we hope to gain a deeper understanding of the experimental results. It seems that $BaTiO_3$ nanoparticle films show an unexpectedly low refractive index and sound velocity in comparison to solid state $BaTiO_3$.

10.4 Experimental Details

Fabrication of two PMMA-$BaTiO_3$ SL was conducted by spin coating 20 alternating layers of PMMA solution (SL A: 2.0 wt% and SL B: 2.5 wt% in toluene) and $BaTiO_3$ particle solution (SL A: 34 mg/mL and SL B: 20 mg/mL in EtOH) at 5000 rpm for 20 s. After spin coating, each layer was heated in the oven for 15 min at 100 °C. Here, the SL A was spin coated onto quartz substrate and the SL B was spin coated on ordinary microscope slides (soda-lime glass).

11 A Tandem Superlattice

11.1 Introduction

After the fabrication and characterization of $(AB)_n$-type superlattices with A being PMMA and B being silica, Schneider *et all.* investigated the effect of different defects onto the phononic dispersion relation of the SLs.[17] They found new modes within the band gap region by introducing an extra PMMA surface layer and defect layer within the SL. Within this theses an exchange the building blocks, especially the nanoparticles in the SLs was presented. The exchange of the building blocks allows to tune the position of the band gap and broaden the width of the gap (see previous chapters).[79]

Within this chapter we want to go on step further and combine two SL into one tandem SL with a structure illustrated in figure 11.1.

In literature a tandem PtCs was published by Goto *et al.*, reported the fabrication of a dielectric multilayer built up from Ta_2O_5-SiO_2 SL with a Ta_2O_5 surface layer and a bismuth-substituted yttrium garnet-SiO_2 SL[154]. This tandem SL is reported to show a optical Tamm state, which is an allowed state within the band gap of the two SLs. This shows that the combination of two different SLs with an additional defect layer exhibits not only the properties of the single lattices but shows new characteristics.

The idea to build 1D PnC with higher symmetry is not new, Quotane *et al.* reported a theoretical study of the propagation of acoustic waves in quasi-periodic structures inspired by the Fibonacci SL.[155].

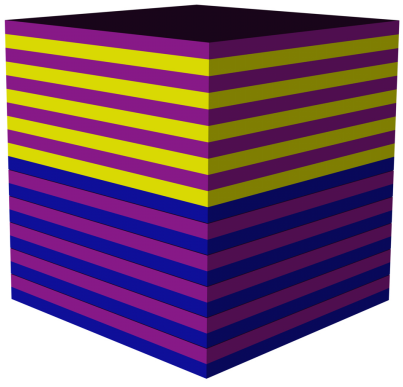

Fig. 11.1: Systematic image of an $(AB)_5A(CB)_5$ tandem superlattice (purple: PMMA, blue and yellow: inorganic nanoparticles).

Nevertheless, the fabrication and characterization of a tandem SL build up from two SL each containing a periodic modulation of the refractive index as well as of the elastic moduli has not yet been published and will be presented here.

11.2 Results and Discussion

The fabrication of the tandem SL was carried out in the same fashion as the AB-type SLs from the previous chapters. First the lower SL was spin coated starting with a SiO_2 layer, and followed by alternating spin coating of PMMA and SiO_2 layers ending with an SiO_2 layer as a defect layer. On top of the SiO_2 layer the $BaTiO_3$-PMMA SL was added using the same strategy. A SEM image of the SL is given in figure 11.2. The lattice spacing of the SiO_2-PMMA lattice was measured to be 143 nm, with a thickness of the SiO_2 layer being 74 nm and a PMMA layer thickness of 69 nm. The upper SL built up from $BaTiO_3$ and PMMA exhibits a lattice spacing from 134 nm, withe the same PMMA layer thickness as the lower SL and a thickness of the $BaTiO_3$ layer of 65 nm.

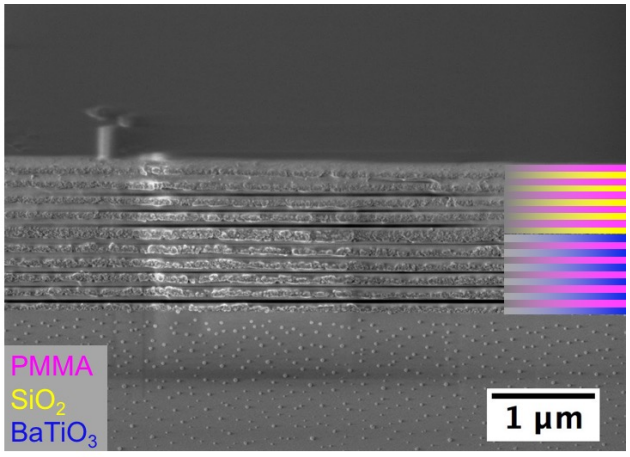

Fig. 11.2: Cross-sectional SEM images of the tandem SL.

Tab. 11.1: Refractive indices and layer thickness (∗ values used in the theoretical calculation).

	refractive index	layer thickness	layer thickness*
PMMA	1.49	69 nm	79 nm*
SiO_2	1.46	74 nm	72 nm*
$BaTiO_3$	1.58	65 nm	74 nm*

11.2.1 Optical Properties

The optical properties of the tandem SL were investigated by measuring the absorption (red line) and transmission (blue line) of the SL. The results are presented in figure 11.3 and two significant absorption maxima were identified at central wavelength of 467 nm and 527 nm. It should be noted that the transmission spectrum is more or less the inverse absorption spectrum and that the single layers do not show any absorption, therefore, the absorption measured here has its origin

in the band gap of the SL. It is known, that the photonic band gap (PtBG) of a single SiO_2-PMMA SL is expected at wavelength around 400 nm, while the PtBG of the $BaTiO_3$-PMMA SL is expected at about 400-500 nm (cp. chapter 10. It is not surprising, that two absorption maxima are found within that region. In comparison to the expected band gap wavelengths, the two maxima found at 467 nm and 527 nm might correspond to the SiO_2-PMMA and the $BaTiO_3$-PMMA sub-SL respectively.

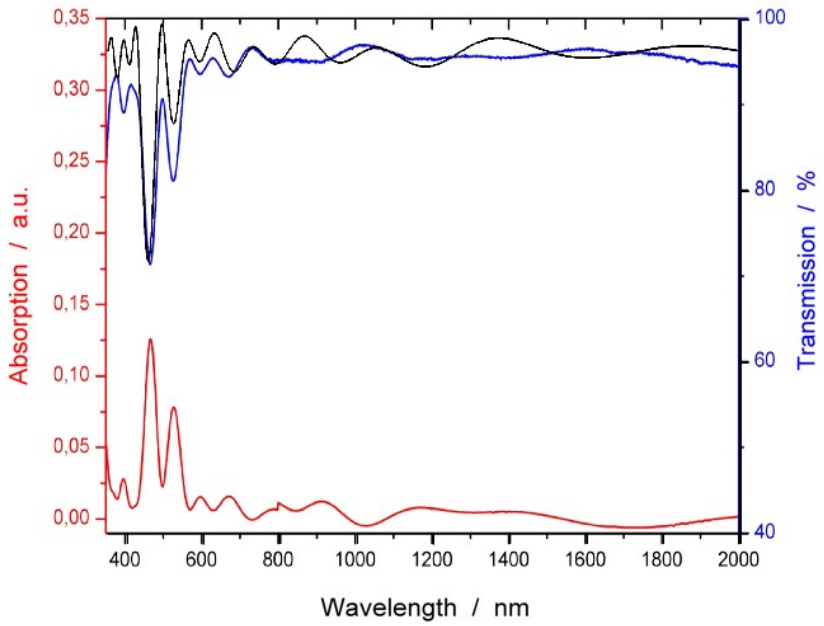

Fig. 11.3: Experimental UV/Vis absorption (red line) and transmission (blue line) spectra and simulated transmission spectrum (black line) of the tandem SL.

The simulated the UV-Vis transmission spectrum, black line in figure 11.3 reflects the experimental data well. The parameters used for the calculation are given in table 11.1, it has to be mentioned that the used layer thicknesses are slightly different but the order lies within the values of the accuracy of measurement error. The refractive indices of 1.5 for the PMMA and 1.46 for the SiO_2 were used before.[16,79] The refractive index for the $BaTiO_3$ layers with 1.58 seems very low but in chapter 10 an explanation for this low refractive index can be found. Evaluation of the theoretical data explain that the two transmission minima are the band gap caused be the tandem SL and the dip in the PtBG at 493.56 nm is an allowed mode within the PtBG. The spatial localization of this mode (square modulus of the electric field versus the space position see figure 11.4 black line), shows that it is propagating inside the SiO_2-PMMA sub-SL, and vanishes inside the $BaTiO_3$-PMMA sub-SL.

For a further interpretation of the BG the transmission spectra of the two sub-SLs were calculated with 20 repeating units to obtain a better quality of the spectra. The transmission spectra and the dispersion curves of the two sub-SLs are given in figure 11.5, it shows that the $BaTiO_3$-PMMA sub-SL causes a larger gap because of

the lager refractive index mismatch between PMMA and $BaTiO_3$ in comparison to the PMMA SiO_2 refractive index difference.

It can be concluded that the optical band gap found in the $(SiO_2\text{-PMMA})_5\text{-}SiO_2\text{-}(BaTiO_3\text{-PMMA})_5$ tandem SL is caused by an addition of the two sub-SLs.

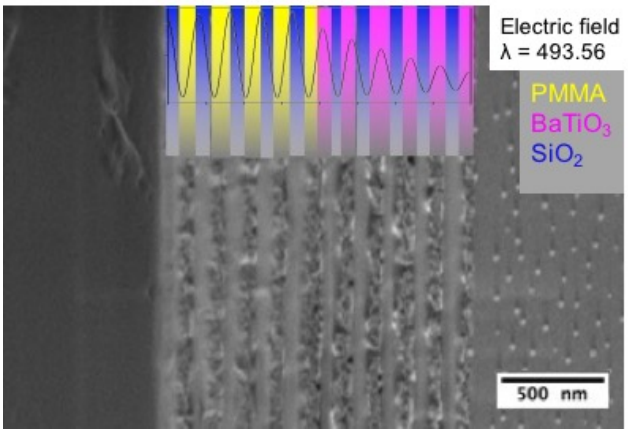

Fig. 11.4: Cross-sectional SEM images of the tandem SL with the spatial localization of the mode at 493.56 nm (black line).

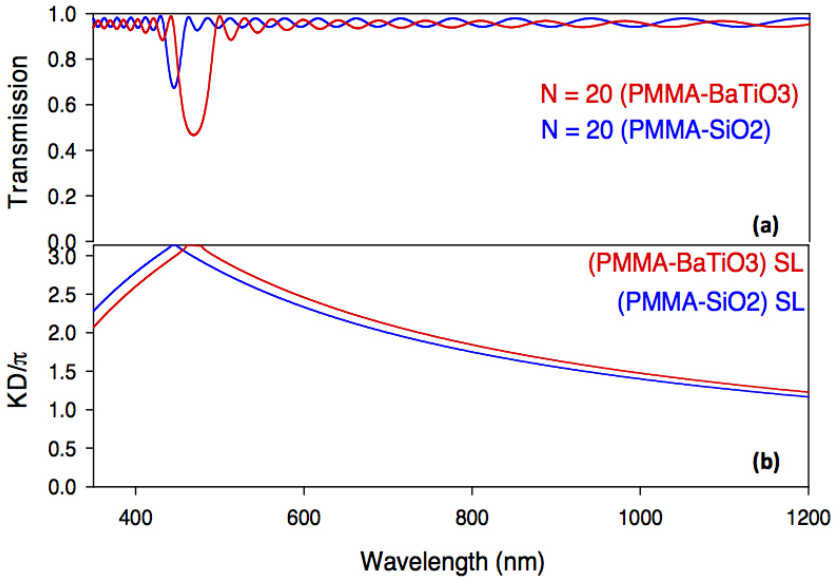

Fig. 11.5: Calculated transmission spectra and below the corresponding dispersion curves of the two sub-SLs (blue line: SiO_2-PMMA sub-SL; red line: $BaTiO_3$-PMMA sub-SL; N=20 repeating units).

11.2.2 Acoustic Properties

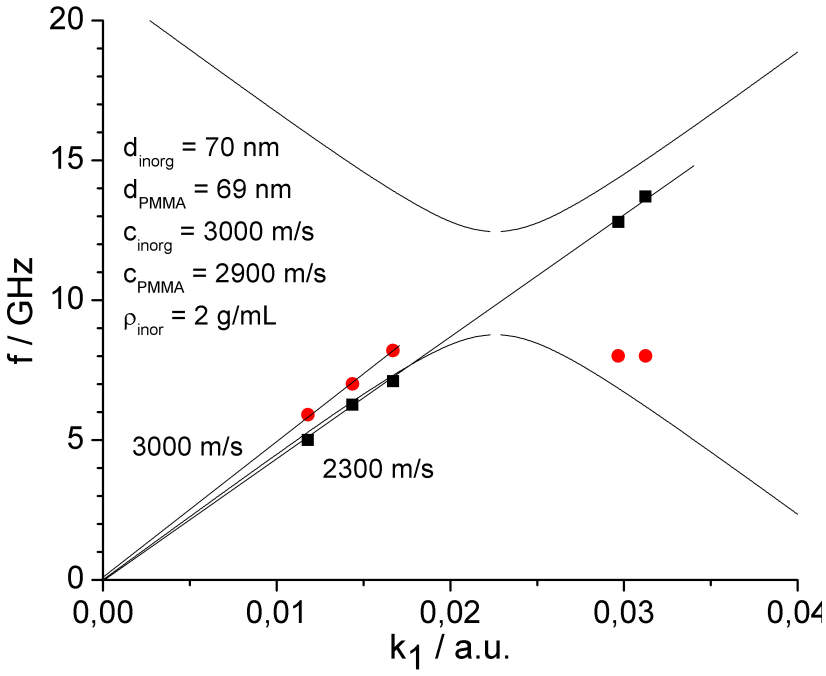

Fig. 11.6: Phonon dispersion relation of the tandem SL, the black line indicates the dispersion relation of an infinite SL with average properties over all inorganic layers. The black squares and the red dots are the measured values from the BLS spectrum, whereas the peaks with higher intensity (black squares) and lower intensity (red dots) are being distinguished.

The phononic properties were investigated as well and the collected BLS spectra are given in figure 11.7 in the experimental details section. The calculated phonon dispersion relation for an infinite SL with average properties (indicated in the figure black line) and the measured dispersion relation are shown in figure 11.6. Without a simulation of the phonon dispersion relation an exact conclusion about the origin of the measured modes is difficult to do. In $q_{\parallel}$, the measured BLS spectra displays a doublet. The dispersion relation of each peak is linear, corresponding to a homogeneous medium of effective sound velocity 3000 m/s and 2300 m/s. The former can be identified with the average sound velocity of a PMMA and SiO_2 blend, with a composition of nanoparticles greater than 50%; this is possible due to the infiltration of PMMA in the SiO_2 nanoparticle layer during the fabrication process. The latter (2300 m/s) can be identified to the average sound velocity of a PMMA with $BaTiO_3$ dispersed nanoparticles; experimental results have reported about the decreased sound velocity of $BaTiO_3$-PMMA blend, respect to the PMMA value (2800 m/s).

Probing with the wave vector $q_{\perp}$ along the periodicity axis, the tandem SL seems to display a phononic band gap with central frequency about 11 GHz. By examining the BLS spectra, one can see a very intense high frequency phonon, and a weak low frequency phonon. The former could be linked to the $BaTiO_3$ sub-SL, due to the

very strong signal (as well in the q-par spectra), and the latter to the phonon in the SiO_2 sub-SL. The absence of the high frequency phonon in the SiO_2 sub-SL could be explain by 1) the short periodicity (only 5 periods) makes the phononic signals to be weak, or 2) the overlapping with the strong phonon in the $BaTiO_3$ sub-SL.

To confirm the assumption of a phononic gap, theoretical simulations must be performed in order to identify the probed modes.

11.3 Summary

Within this chapter the fabrication and characterization of a tandem SL build up from a SiO_2-PMMA and a $BaTiO_3$-PMMA SL was presented. Two absorption maxima at 467 and 527 nm were experimentally found and in theoretical calculations of the transmission spectrum the optical band gap with an allowed mode of a wavelength of about 500 nm was identified. The phononic behaviour of the SL was investigated as well, but could not be justified by theoretical calculations up to now. Meaning the dispersion relation presented here is only a preliminary result and a further characterization of the tandem SL is in process.

11.4 Experimental Details

We fabricate these superlattices analog to the AB-type lattices as described in chapter 7. The PMMA solution had a concentration of 2.5 wt% in toluene and the SiO_2 nanoparticle solution had a concentration of 33.5 g/L and $BaTiO_3$ 20 g/L Spin coating parameters: speed: 5000 rpm, time: 20 s, acceleration: 5000 rpm/s, heat treatment: 100 °C 15 min.

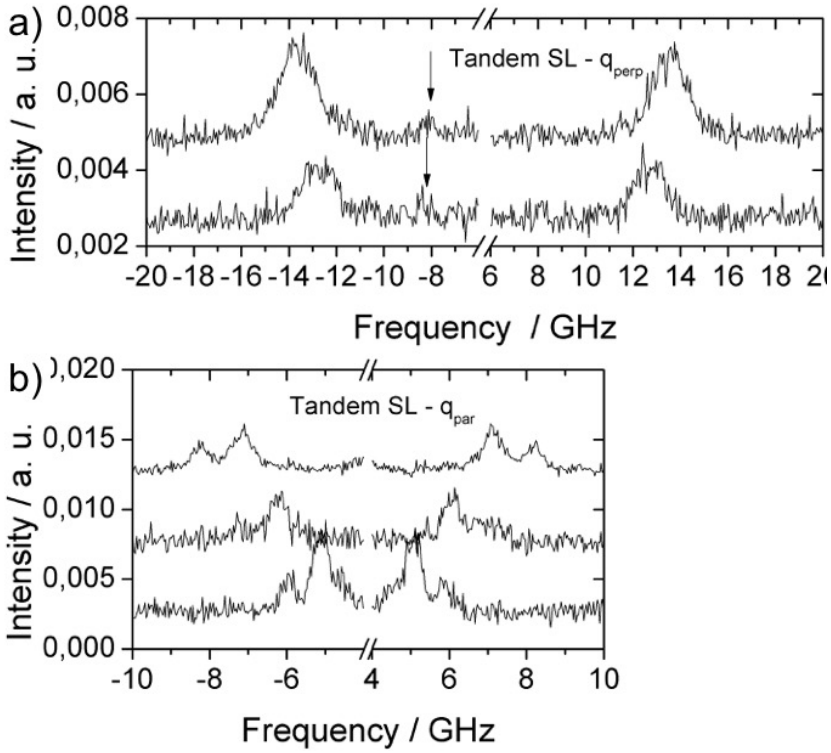

Fig. 11.7: Perpendicular (a) and parallel (b) BLS spectra of the tandem SL.

12 Superlattices with an $(ABAC)_n$ Periodicity

12.1 Introduction

The SL presented in this chapter is constructed from three different building blocks and shows higher-order periodicity. The $(AB)_n$-type SL discussed in the previous chapters can be understood as crystal lattices form two ions, like for example calcite ($CaCO_3$). When taking a closer look at the calcite crystal structure along the c-axis, a layered structure can be identified. In one plane the carbonate groups are located (layer A) and in the second plane corner-linked calcium octahedra can be found (layer B). In a calcite crystal these two layers are repeated multiple times, similar to the multilayers in the SLs, just on a different length scale.

By going from calcite to dolomite ($CaMg(CO_3)_2$) the crystal lattice changes from an $(AB)_n$-type to an $(ABAC)_n$-type, with A being carbonate groups, B being calcium ions and C being magnesium ions. Transferring the dolomite periodicity onto our polymer-nanoparticle SLs, results in the SL shown in figure 12.1.

In the previous chapters four materials were optimized as layer materials, namely PMMA, and SiO_2, TiO_2 and $BaTiO_3$ nanoparticles. By using these four different materials, and taking into account, that PMMA is the only soft material to achieve a contrast of the elastic moduli, three different SLs with a $(ABAC)_n$ periodicity can be easily prepared, with A being PMMA and B and C being SiO_2, TiO_2 or $BaTiO_3$ nanoparticles.

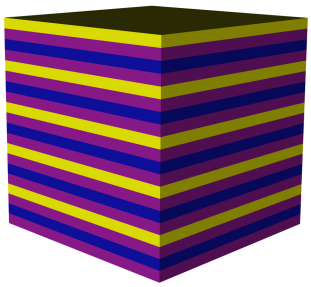

Fig. 12.1: Systematic image of an $(ABAC)_n$ superlattice (purple: PMMA, blue and yellow: inorganic nanoparticles).

Unlike the tandem SL these SLs are not just a combination of two SLs. Here, in each SL three different layer materials are combined and three new higher ordered SLs are fabricated.

12.2 Results and Discussion

Below the morphology and optical properties of three different $(ABAC)_n$ superlattices are discussed. The SLs are built up from PMMA as a soft, low refractive index material and SiO_2, TiO_2 and $BaTiO_3$ nanoparticles as hard, high refractive index materials. The SLs were fabricated following the same spin coating and heat treatment methods as described in chapter 7. All three (ABAC)n SLs have five repeating units (n=5), build from ten PMMA and twice five inorganic nanoparticle layers. In this chapter SL will be named as follows:
SL I: A: PMMA, B: SiO_2, C: TiO_2,
SL II: A: PMMA, B: SiO_2, C: $BaTiO_3$ and
SL III: A: PMMA, B: TiO_2, C: $BaTiO_3$.

Cross-sectional SEM images of the SLs are shown in figure 12.2. On the left side, a high magnification image shows the detailed structure of the layers and the lower magnification images on the right side confirms that all layers are homogenous over a large area. The SEM images show, that all SL are build from 20 layers starting from bottom to top with a PMMA layer (black in the SEM image) and ending with an inorganic nanoparticle layer. Further the SEM image allows to recognize a small contrast difference between the two different nanoparticle layers. Especially in the SEM image of SL I the TiO_2 layers are a little brighter than the SiO_2 layers. This is caused by the higher contrast of TiO_2 in comparison to the SiO_2, due to the higher electron density.

The lattice parameters for the three SLs are given in table 12.1. Interesting is that even though the same nanoparticle solutions was used, the layer thicknesses seem to differ slightly. However, the variation of the thickness is within the measurement error. For the PMMA the variation of the layer thickness is more significant and can not be explained only by an experimental error. As mentioned in chapter 7 the layer thickness is influenced by different factors and the fabrication outcome can differ from day to day, since a slower start of the spin coater after the deposition of the solution leads to a thicker layer. This could have caused the large differences within the PMMA layer thicknesses in SL II and SL III.

Tab. 12.1: Lattice parameter for SL I-III and the refractive indices of the layer material, the values in brackets are being used for the calculation.

	SL I	SL II	SL III	refractive index
PMMA	53 (65) nm	36 nm	74 nm	1.5
SiO_2	63 (73) nm	53 nm		1.46
TiO_2	58 (68) nm		56 nm	1.85
$BaTiO_3$		54 nm	52 nm	1.6

For optical characterisation of the SLs UV/Vis absorption and transmission spectra were recorded. The resulting UV/Vis spectra and photographs of the SLs are shown in figure 12.3. The SLs have a yellow colour when observed from a top view but when

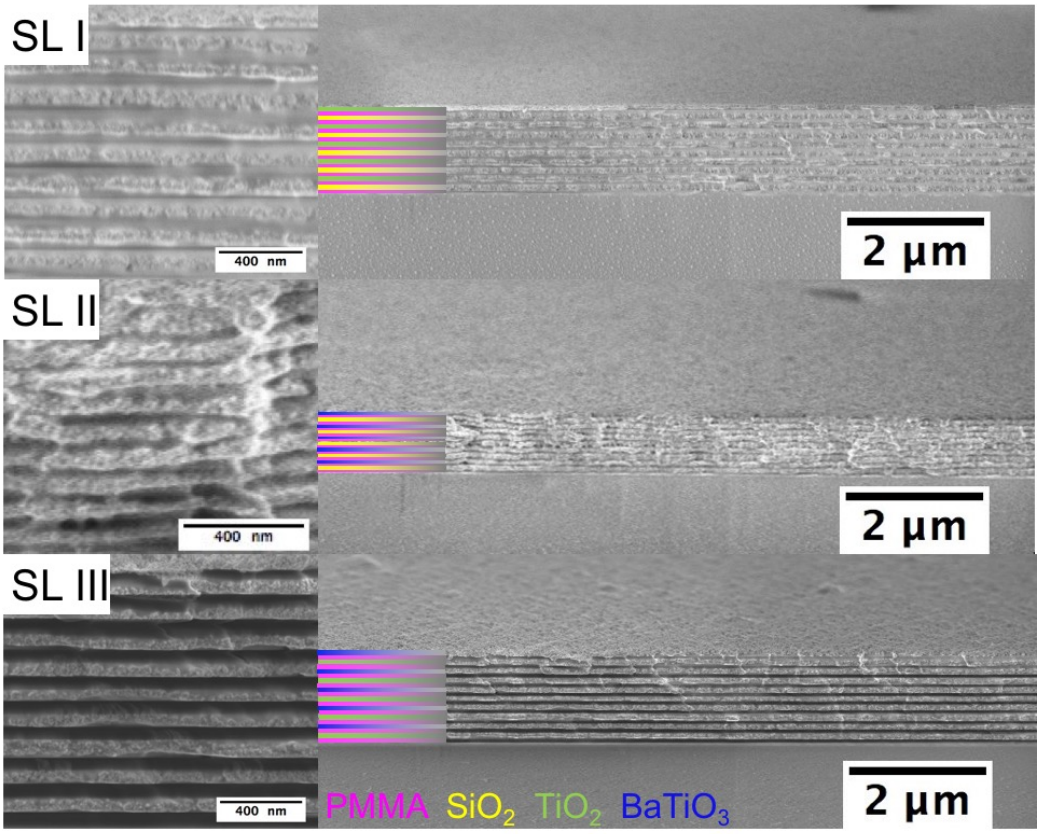

Fig. 12.2: Cross-sectional SEM images of the three $(ABAC)_n$ SLs with SL I consisting of A: PMMA, B: SiO_2, C: TiO_2, SL II of A: PMMA, B: SiO_2, C: $BaTiO_3$ and SL III is built uo from A: PMMA, B: TiO_2, C: $BaTiO_3$.

the SLs are slightly tilted they appear blue. This behaviour is typical for photonic crystals. The UV/Vis absorption spectrum of SL I shows two strong maxima at 438 nm and 835 nm, while SL II shows only one strong absorption maximum and 567 nm and SL III one at 457 nm.

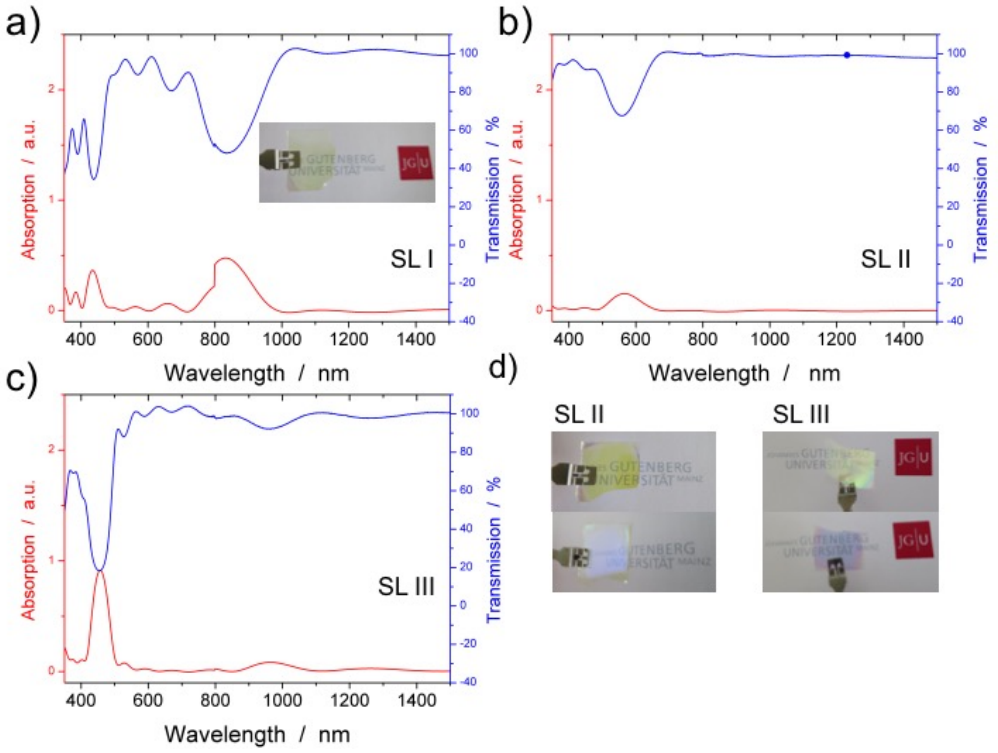

Fig. 12.3: UV/Vis absorption and transmission spectra of a) SLI, b) SLII, c) SLIII. d) Photos of SL II (left) and III (right) in the upper photos the SL appears yellow, while if the SL is slightly tilted, as shown in the lower image the SL appears blue.

As mentioned above SL I shows two strong absorption maxima which are expected to have their origin in the strong refractive index mismatch between PMMA and TiO_2 on the one hand and SiO_2 and TiO_2 on the other hand.

It is known, that PMMA-TiO_2 SLs exhibits an optical band gap at 315 - 360 nm.[79] The red shift, in comparison to previous results, is caused by the higher lattice constant. To understand the origin of the second band gap with a central frequency of 835 nm theoretical calculations need to be done. One could expect that the SiO_2 - TiO_2 SL is responsible for the second band gap.[112]

To confirm the origin of the resulting band gaps the optical reflection and absorption spectra of the SL I was calculated by El-Houssaine El Boudouti and coworkers using a numerical approach. The results are given in figure 12.4 (doted lines) and show a very good agreement between the calculation and the experimental data (continuous lines).

Especially if the repeating units are raised from five, as fabricated in the experiment, to 20 the shoulders within the calculated spectrum disappear while the position of the band gap stays close wavelengths found experimentally (see figure 12.5 a)

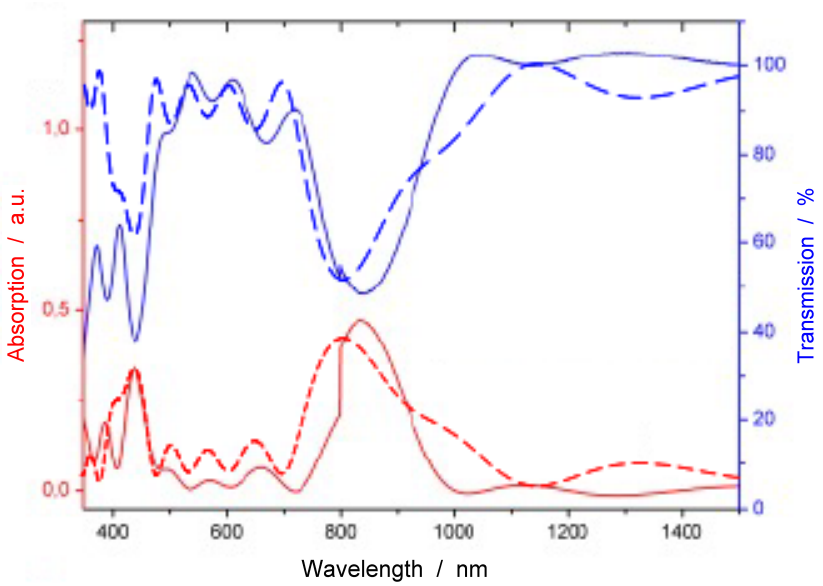

Fig. 12.4: The experimental (continuous lines) and the calculated (dashed lines) UV/Vis absorption and transmission spectra of SLI.

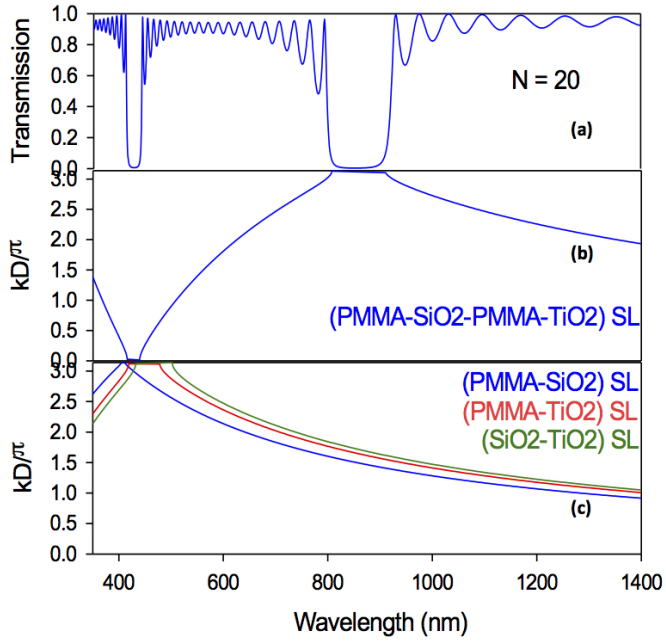

Fig. 12.5: (a) Calculated transmission spectra of the SL I with 20 repeating units. (b) Calculated dispersion curve of an infinite SL I. (c) Dispersion curves of infinite PMMA-SiO_2 (blue), PMMA-TiO_2 (red) and a SiO_2-TiO_2 (green) SLs.

and b)). The calculation of the dispersion relations of the single PMMA-SiO_2, PMMA-TiO_2 and SiO_2-TiO_2 sub-SLs show, that all sub-SLs exhibits a band gap in the region around 450 nm (figure 12.5 c). Against the expectations, the band gap around 850 nm does not stem from a sub-SL, but seems to be a characteristic of the $(ABAC)_n$ SL.

In contrast to SL I, SL II shows only one transmission minimum at a central wavelength of 567 nm. It is expected that this relatively broad transmission minimum has its origin in the refractive index mismatch within the PMMA-$BaTiO_3$ sub-SL and, at the same time, in the refractive index difference in the SiO_2-$BaTiO_3$ sub-SL. Both refractive index differences are in the same region, making the two band gaps overlap, resulting in one broad band gap. The absence of a second band gap could be cause due to the difference between the refractive indices of SiO_2 and $BaTiO_3$ is not strong enough to pronounce the ABAC periodicity, therefore this SL behaves like a $(AB)_n$ periodic SL. This hypothesis should be confirmed by calculations.

SL III shows a similar optical behaviour to SL I. Two band gaps can be identified, one at 457 nm, most probably caused by the PMMA-TiO_2, PMMA-$BaTiO_3$ and the TiO_2-$BaTiO_3$ sub-SLs and one at 965 nm most probably caused by the ABAC periodicity. This assumption needs to be clarified by a theoretical calculation of the dispersion relation of the SL and the sub-SLs. The reason why the band gaps where $BaTiO_3$ contributes to the optical contrast are not as intense as for SiO_2 or TiO_2 lies in the nature of the $BaTiO_3$ layer. Due to this layer is more porous and irregular than the other nanoparticle layers, and it is well known, that this kind of inhomogeneity causes losses in the intensity of the band gap.[4]

12.3 Summary

The fabrication of $(ABAC)_n$ SLs was successfully demonstrated and the optical properties were investigated. They show one or two band gaps, depending on the optical contrast between the building blocks of the SLs. The phononic behaviour was not yet characterized since the BLS technique for the measurements of the phonon propagation can only monitor phonons up to 50 GHz. Here, due to the different periodicity and the resulting high lattice constant phonons in a higher frequency range need to be measured as well. A pump probe technique[156] could be a suitable method for the characterization of the phononic properties of the $(ABAC)_n$ SLs.

Further, in first calculations the optical band structure was simulated and showed a good fit with the experimental data. The calculations of the two other SLs is in process.

12.4 Experimental Details

These superlattices were fabricated analog to the AB-type lattices as described in chapter 7. The PMMA solution had a concentration of 2.5 wt% in toluene and the SiO_2 nanoparticle solution had a concentration of 33.5 g/L and the TiO_2 and $BaTiO_3$ nanoparticle solutions had a concentration of 65 g/L and 20 g/L respectively. Spin coating parameters were: speed: 5000 rpm, time: 20 s, acceleration: 5000 rpm/s, heat treatment: 100 °C 15 min.

13 Superlattice with a $cSiO_2$ Defect Layer

13.1 Introduction

In this chapter the incorporation of colloidal SiO_2 ($cSiO_2$) into a PMMA-SiO_2 superlattice (SL) is investigated. A schematic image of the desired SL is given in figure13.1, a layer of $cSiO_2$ with an average size of 218 nm is added as a defect layer in the centre of the PMMA-SiO_2 SL. This geometry is interesting because $cSiO_2$ show acoustic eigenvibrations (f~1/d, d=diameter of the particles) in the gigahertz frequency range.[157] The acoustic eigenmodes of the $cSiO_2$ particles might interact the phononic band of the SL.

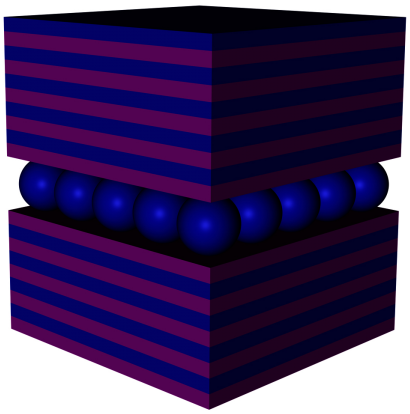

Fig. 13.1: Schematic sketch of the SL with a $cSiO_2$ defect layer.

On top of the interesting phonons propagation in such a SL, the experimental challenges for spin coating are demanding. The incorporation of bigger sized particles is difficult, because their spin coating behaviour differs in comparison to small nanoparticles. Particles with a size above 100 nm are heavy and do not easily stick on the surface. Further, the void space within a layer of $cSiO_2$ particles is tremendous higher than the void space in 10 nm sized particles. Indeed, the void space is bigger than the smaller particles and therefore the infiltration of polymer or nanoparticles is expected, and that could effect the homogeneity of the top layers strongly. Therefore a spin coating strategy for $cSiO_2$ needs to be developed and a fitting void-filling material for the $cSiO_2$ layer needs to be investigated.

13.2 Results and Discussion

13.2.1 Fabrication of the SL

$cSiO_2$ particles were synthesized following the synthesis strategy of Stoeber *et al.*[158] First tetramethyl orthosilicate was hydrolysed in a mixture of ammonium hydroxide and ethanol, then the mixture was stirred at room temperature. A TEM image of the resulting $cSiO_2$ particles is presented in figure 13.2, the particles show an average size of 218 nm, which is a fitting size with a sufficient size distribution for the inccoperation as a defect layer in SLs.

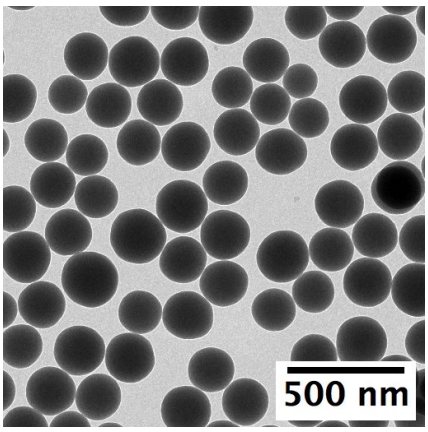

Fig. 13.2: TEM image of $cSiO_2$ particles.

For spin coating the coloidal particles, they were dissolved in a 14 % ammonium hydroxide solution. To optimise the spin coating conditions for the $cSiO_2$ layer, SLs built from just 4 bilayers were prepared starting with the following stacking order: PMMA-SiO_2 BL, PMMA-$cSiO_2$ and on top two PMMA-SiO_2 BLs. In a first experiment the pure $cSiO_2$ particles were spin coated into the SL, the results of this experiment is shown in figure 13.3.

The $cSiO_2$ particles are aggregated in some parts of the sample and build huge satellites, in other parts of the SL no $cSiO_2$ particles can be seen. The two PMMA and SiO_2 layers on top of the $cSiO_2$ layer are difficult to identify, it looks like the layers diffused into the underlying layer, only the top SiO_2 is well defined.

To suppress the agglomeration of $cSiO_2$ particles and at the same time suppress the diffusion of the top layers into the void space of the $cSiO_2$ layer different additives were tested.

The first additive chosen was PMMA. Adding different amounts of PMMA into the $cSiO_2$ solution makes it more viscose, so the particles can not aggregate and the PMMA could fill the void space at the same time. The spin coated SLs with different $cSiO_2$ to PMMA weight ratios are shown in figure 13.4. When using a 1:1 ratio of PMMA:$cSiO_2$ (figure 13.4a) the $cSiO_2$ particles are distributed much better in the layer than the pure $cSiO_2$. But still the top layers are effected by the $cSiO_2$ particles and show a non-homogeous coverage of the underlying layer because the big $cSiO_2$

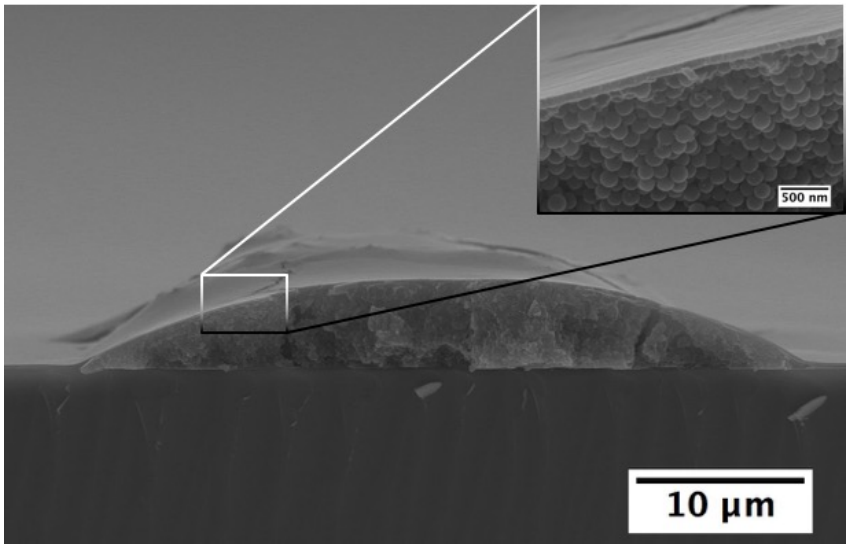

Fig. 13.3: Cross-sectional SEM image of a 3 BL PMMA-SiO_2 SL with a $cSiO_2$ defect layer.

particles tower into the top layers. When adding twice as much PMMA to the $cSiO_2$ solution, the amount of the PMMA is so high, that the $cSiO_2$ particles disappear within the polymer layer. When reducing the amount of PMMA to a $cSiO_2$:PMMA ratio of 2:1 the results are similar to the 1:1 PMMA:$cSiO_2$ ratio. This results lead us the the conclusion that PMMA as an additive helps to improve the quality of $cSiO_2$ layer a little, but the targeted quality of the SL could not be achieved.

The second approach to improve the quality of the SL was, adding Ludox SiO_2 particles to the $cSiO_2$ solution and at the same time to increase the concentration of the $cSiO_2$ particles from 28 mg/mL to 50 mg/mL. Unlike PMMA, the solubility of Ludox particles is identical to the solubility of $cSiO_2$, which makes it easy to mix the two particles. Furthermore, the small SiO_2 particles fill the void space between the huge $cSiO_2$ particles equally good. In figure 13.5 the SEM images of resulting SLs with different $cSiO_2$:SiO_2 ratios are presented.

The SEM image of the SL with a $cSiO_2$:SiO_2 weight ratio of 1:1 is given in figure 13.5a. In the defect layer mainly SiO_2 particles can be seen, this means that the $cSiO_2$ solution contains a too big amount of SiO_2, while the concentration of $cSiO_2$, with 50 g/L, is too small. By reducing the concentration of the SiO_2 particles down to half, the results look still similar (figure13.5b). In the next experiment the concentration of the $cSiO_2$ particles was doubled, and at the same time the relative amount of SiO_2 particles was tremendously decreased to a $cSiO_2$:SiO_2 ratio as high as 16:1. This yield in a continuous alignment of $cSiO_2$ particles into a layer, while the SiO_2 particles filled the void space well, so that the top layers were not damaged by the big $cSiO_2$ particles (figure13.5c). If the relative amount of $cSiO_2$ particles is further increased to 37:1, the $cSiO_2$ layers stay homogenous even so at the same time the absolute amount of $cSiO_2$ particles was reduced to 37 g/L (figure13.5d). The reduction of the concentration of the $cSiO_2$ particles is useful because it allows us to save material and still get equally good SLs. Thats why for the fabrication

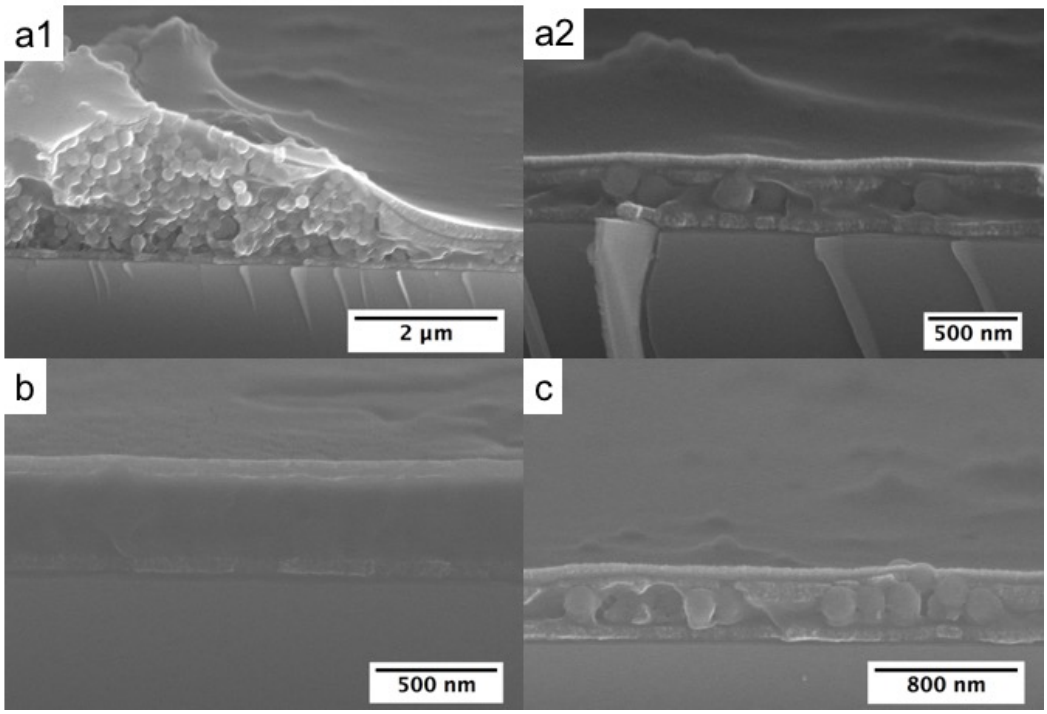

Fig. 13.4: Cross-sectional SEM images of PMMA-SiO_2-PMMA-$cSiO_2$-$(PMMA\text{-}SiO_2)_2$ SLs with different amounts of PMMA added to the $cSiO_2$ layer. a) $cSiO_2$:PMMA ratio 1:1, b) $cSiO_2$:PMMA ratio 1:2, c) $cSiO_2$:PMMA ratio 2:1.

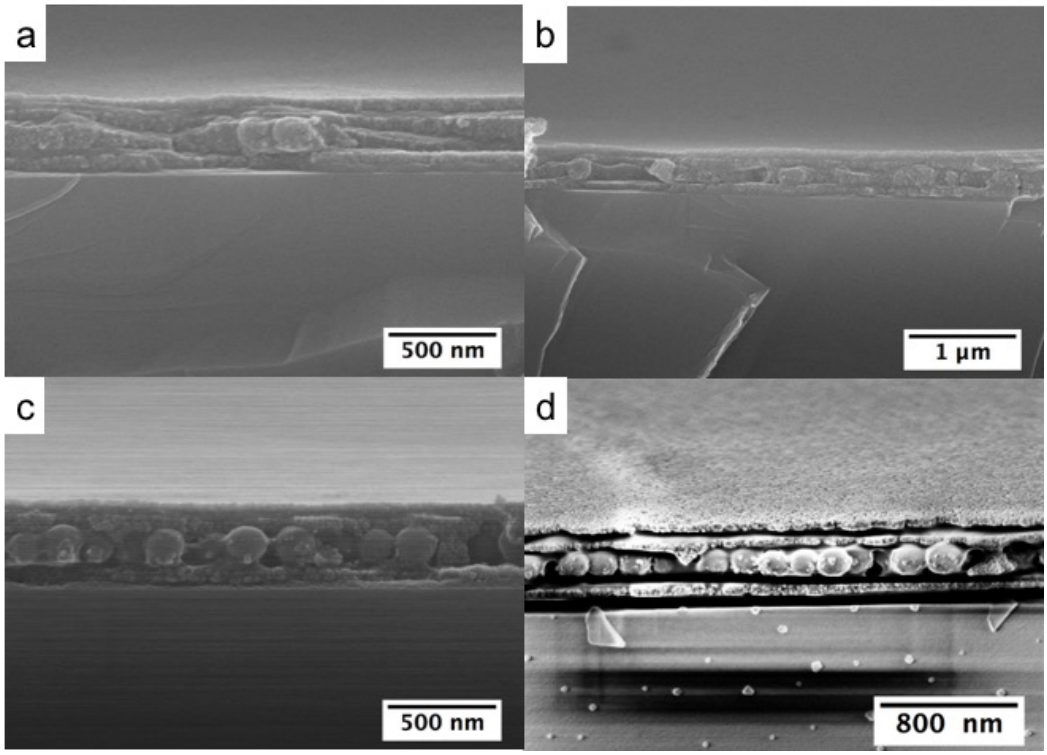

Fig. 13.5: Cross-sectional SEM images of PMMA-SiO_2-PMMA-$cSiO_2$-$(PMMA\text{-}SiO_2)_2$ SLs with different $cSiO_2$:SiO_2 weight ratios in the $cSiO_3$ layer, a) $cSiO_2$:Ludox 1:1, b) $cSiO_2$:Ludox 2:1, c) $cSiO_2$:Ludox 16:1, d) $cSiO_2$:Ludox 37:1.

of a 10 BL SL a $cSiO_2$ concentration of 37 g/L and a $cSiO_2$:SiO_2 ratio of 37:1 was chosen.

The SL shown in figure 13.6 was prepared by using this optimized spin coating parameters. With this condition it is possible to incorporate the huge colloidal SiO_2 particles into a hybrid polymer-nanoparticle SL without disturbing the delicate layer structure.

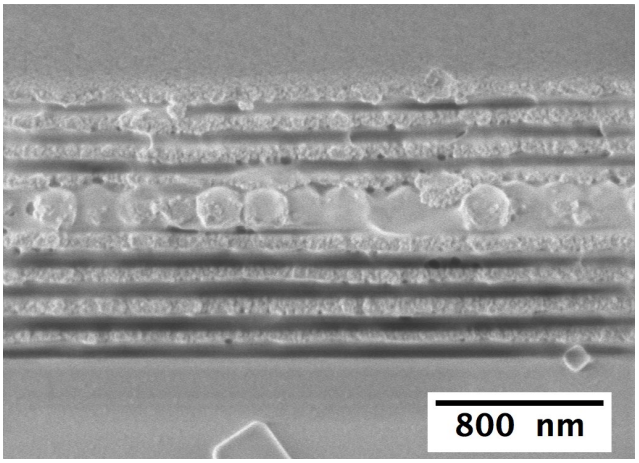

Fig. 13.6: Cross-sectional SEM images of $(PMMA\text{-}SiO_2)_4$-PMMA-$cSiO_2$-$(PMMA\text{-}SiO_2)_4$ SL with a $cSiO_2$:SiO_2 ratios of 37:1 in the defect layer.

The lattice parameter a of this SL is 137 nm with a PMMA layer thickness of 67 nm and a thickness of 70 nm for the SiO_2 layer. The $cSiO_2$ layer with 218 nm is identical to the diameter of the particles.

13.2.2 Characterisation of the SL using BLS

The phononic properties were investigated using BLS spectroscopy. The resulting phonon dispersion relation is given in figure 13.7 (the corresponding BLS spectra is given in figure 13.8 in the experimental section). The squares show experimental dispersion relation, while the black solid line gives the theoretical expected dispersion relation of a infinite PMMA-SiO_2 SL with a periodicity of 137 nm. The expected phononic band gap could not be found, instead, a continuous propagation was found. To fit the elastic anisotropy between the two orthogonal directions an effective refractive index of 1.4 was estimated, this was done thought the dependence of q_{perp} (n) and the assumption of a linear dispersion relation in both directions parallel and perpendicular to the substrate. This is low for a PMMA-SiO_2 SL and could be justified by the assumption of air voids (porosity), that relax the effective medium n. This is most likely the case, due to the huge $cSiO_2$ particle layer could include air into the SL and therefore reduce the effective refractive index to 1.4. The absence of a phononic band gap means that the hole SL acts as a effective medium and the periodicity of the SL seems not to influence the phonon propagation. A reason for such a behaviour could be that by breaking the symmetry of the SL through adding colloidal particles into the centre, the periodicity of the SL is not high enough

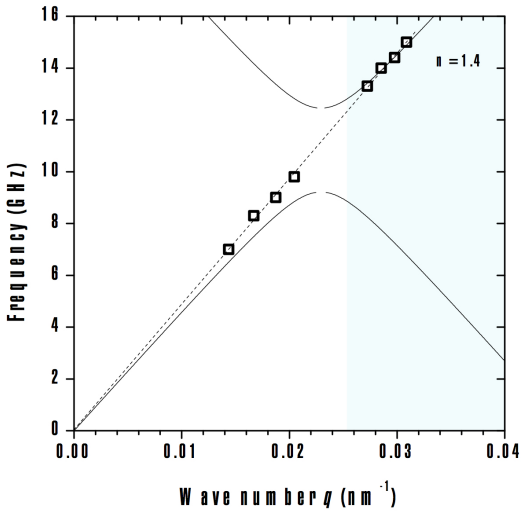

Fig. 13.7: Experimental dispersion relation (squares) acquired in plane (white area) and out of plane (blue area). The effective refractive index used is n = 1.4. The dashed line is a guide to the eye, and denotes the elastic anisotropy between the two orthogonal directions. The solid line is the predicted dispersion diagram for a infinite PMMA-SiO_2 SL, of 137 nm period.

to let the SL act as a periodic medium. An effect of the cSiO2 is not observed. To detect the eigenmodes of the $cSiO_2$ particles Still *et al.* used a larger amount of $cSiO_2$ particles as were induced within this SL, meaning the influence of the $cSiO_2$ particles is not detected because of its low concentration within this SL. A longer accumulation time for the BLS or a higher relative concentration of $cSiO_2$ particles could allow a detection of the eigenmodes of $cSiO_2$ particles. And to observe the SL acting as a periodic medium the periodicity of the PMMA-SiO_2 SL needs to be increase. Maybe an influence of the $cSiO_2$ particles could be observed if a multilayer of $cSiO_2$ particles is incorporated within a 20 BL SL of PMMA-SiO_2, because a 10 BL SL is known to act as a phononic crystal.[16] Further, the pump probe technique[156] seems to be promising for detecting eigenmodes of the colloidal layer, since the amplitude of the pumped modes would be much larger in comparison with the thermal phonons probed by BLS.

13.3 Summary and Outlook

The incorporation of colloidal silica particles into a SL was achieved by adding a defined amount SiO_2 nanoparticles as void filling materials into the colloidal particle mixture. Using this approach a homogenous layer of colloidal particles was spin coated in the middle of a PMMA-SiO_2 SL. It was not possible to monitor a coupling between the phonon propagation within the SL and the phonon eigenmodes of the colloidal particles. This could have different reasons. One possible explanation could be that the amount of colloidal particles was not sufficient and another explanation could be that the frequency range covered by BLS is not sufficient for the detection of the phonons here.

13.4 Experimental Details

13.4.1 Synthesis of Colloidal Silica Particles

In a typical synthesis 3 mL of tetramethyl orthosilicate was added drop wise to a solution of 5 mL water, 1.5 mL 25% ammonium hydroxide solution and 35 mL ethanol at room temperature. After stirring the solution for 10 min the transparent solution turned into a turbid solution. After one hour the stirring was stopped and a sample of the particles were collected for TEM imaging. A TEM sample was prepared by diluting the reaction mixture with ethanol and giving two drops of the diluted solution onto a carbon coated copper grid. The size was determined by measuring 50 particles and turned out to be 218 nm in average.[158]

13.4.2 Fabrication of the 10 BL SL

Alternating layers of PMMA and SiO_2 were spin coated from solution onto a 2x2 cm sized soda-lime glass substrate. A 2.5 mg/mL PMMA Solution was prepared by dissolving commercially purchased PMMA with a molecular of 35.000 g/mol in toluene. A 33.5 mg/mL concentrated silica particle solution was prepared by mixing 1000 µL 10 wt% SDS, 90.71 mL 14% ammonium hydroxide solution and 9.29 mL Ludox solution in a glass flask and stirring the solution for 2 h. Before spin coating, the silica solution was filtrated with a 0.45 µm syringe filter and the PMMA solution with a 0.2 µm syringe filter. The colloidal silica particles were synthesized as described above. And for spin coating the 10BL SL 112 mg of the colloidal particles were dissolved in 3 mL 14% ammonium hydroxide and 10 µL of Ludox and 30 µL of 10 wt% SDS solution in water were added to the solution. For the $cSiO_2$ solution containing different amounts of PMMA or Ludox the preparation protocol for the spin coating solutions are given in table 13.1.

Spin coating was carried out by spreading 400 µL of the PMMA solution (500 µL of the SiO_2 solution) onto the glass substrate and then the spin coater was started with an acceleration of 500 rpm/sec to as speed of 5000 rpm for 20 sec. After each spin coated step, the sample was heated to 100 °C for 15 min to make sure that all solvent is removed from the sample. The colloidal silica was spin coated in the same fashion, but at lower acceleration of 1000 rpm/sec and at a speed of 1000 rpm.

For the optimization of the amounts of PMMA or Ludox in the $cSiO_2$ solutions the same spin coating conditions and the same PMMA and SiO_2 solutions as described above were used and the $cSiO_2$ solutions were prepared as described in table 13.1.

Tab. 13.1: Preparation protocol of the different $cSiO_2$ solutions (*ethanol and 16.6 vol% acetone; $^+$ 14 vol% NH_3 and additional 10µL 10 wt% SDS solution).

Sample	$cSiO_2$ [mg]	PMMA [mg]	Ludox [µL]	Solvent [mL]
$cSiO_2$:PMMA 1:1	28	28	-	1*
$cSiO_2$:PMMA 1:2	28	56	-	1*
$cSiO_2$:PMMA 2:1	28	14	-	1*
$cSiO_2$:SiO_2 1:1	50	-	167	0.833^+
$cSiO_2$:SiO_2 2:1	50	-	83	0.917^+
$cSiO_2$:SiO_2 16:1	100	-	20.8	0.979^+
$cSiO_2$:SiO_2 37:1	37	-	3.3	0.997^+

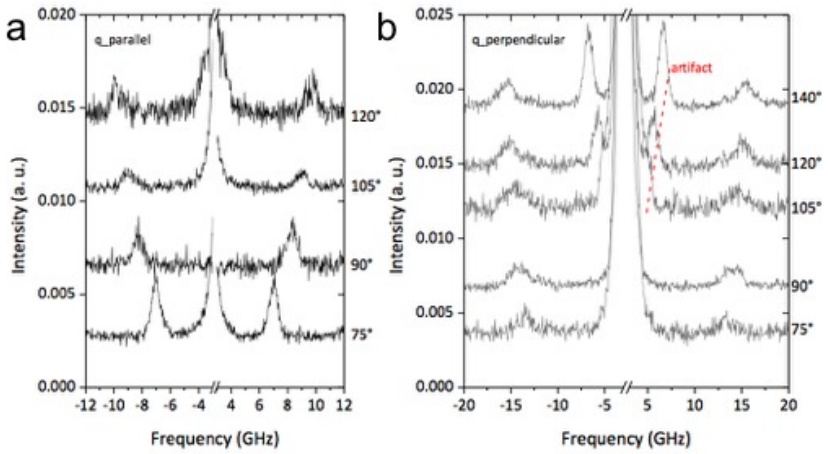

Fig. 13.8: BLS spectra acquired in plane (a) and out of plane (b).

14 Responsive Layers

14.1 Introduction

The idea to incorporate responsive layers in a super lattice opens up promising applications of SL as sensors. In the field of polymeric photonic crystals (PtC), it has been shown already that the colour of the PtC can be changed by water[6] or ionic liquid[159]. Kang and coworkers showed, that a block copolymer of polystyrene (PS) and poly(2-vinyl pyridine) (P2VP) self-assembles into a lamellar structured PtC. After quaternization and cross-linking of the P2VP layer with 1-bromoethane and 1,4-dibromobutane, the colour of the PtC could be changed by swelling the PtC in water. This change of band gap was reversible due to the fact that water could be withdrawn by adding ammonium chloride to the solution. The degree of swelling has been reported to be controlled by the ratio of cross-linking to quaternization of the P2VP layer. The less the sample was cross-linked, the stronger was the swelling. They reported a shift of the central band gap wavelength from 364 nm up to 1627 nm through the swelling of the PtC with water.[6]

A wavelength shift of the photonic band gap without cross-linking or quaternization of the P2VP block could be realised using ionic liquid (imidazole and imidazolium bis(trifluoromethanesulfonyl)imide)) as a swelling reagent. Like water in the work of Kang *et al.*, the ionic liquid diffuses into the P2VP block, which, therefore, swells. This process in non-reversible but the swollen films are stable fore more than 100 days due to the non-volatility of the ionic liquid.[159]

Thus our aim is to transfer the feature of *in situ* tunability of purely polymeric PtC to the hybrid SLs by using P2VP as a soft, low refractive index building block and as before, inorganic nanoparticles as hard, high refractive index building blocks.

14.2 Preliminary Experiments

14.2.1 Polymer Synthesis

The P2VP was synthesised using RAFT (reversible addition-fragmentation chain-transfer) polymerisation. We choose RAFT polymerisation, because it is a controlled radical polymerisation and yields polymers with a relatively low PDI (polydispersity index).[160] The mechanism of RAFT polymerisation is shown in figure 14.1, the RAFT equilibrium is the essential step for yielding to a narrow PDI. By reversible addition and fragmentation of the sulphur-containing chain-transfer agent (CTA) the polymerisation slows down leading to a narrow molecular weight distribution.

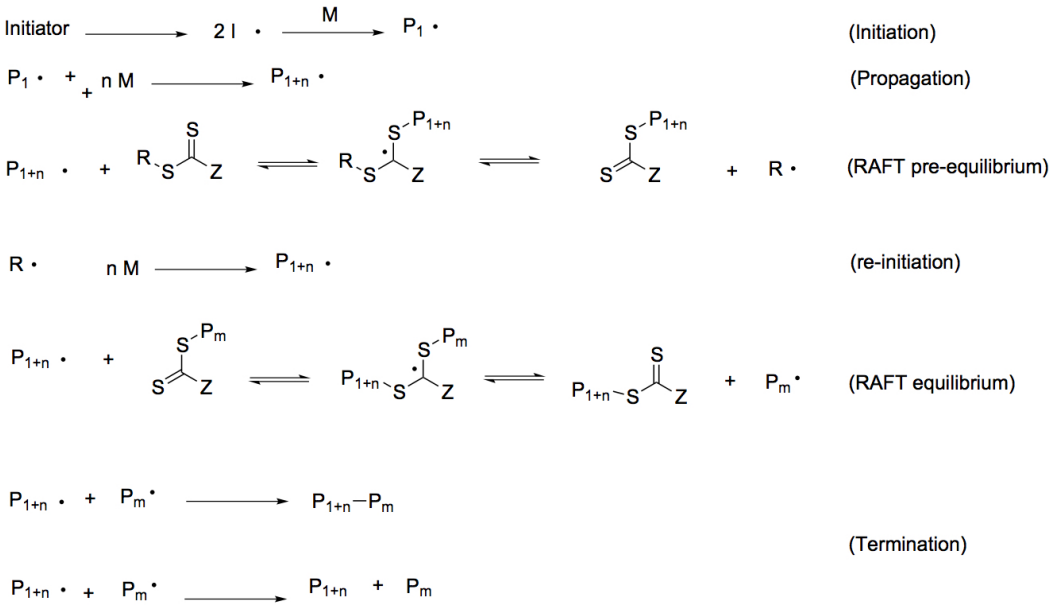

Fig. 14.1: Scheme of the reaction mechanism of the RAFT polymerisation.

For the polymerisation of 2-vinylpydrine, a benyl dithiobenzoate was used as CTA, AIBN as initiator and DMF as solvent. At a reaction temperature of 80 °C, the polymerisation was complete after 48 h (detailed reaction parameters are given below).

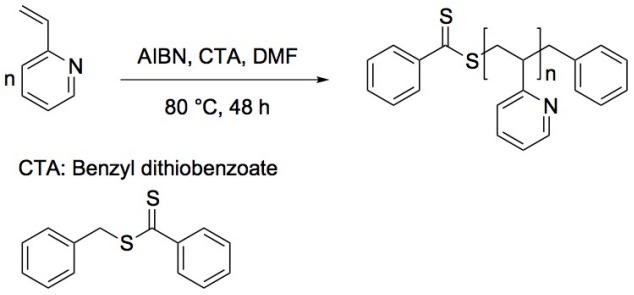

Fig. 14.2: Reaction scheme of P2VP synthesis.

For determination of molecular weight the conversion of the monomer using NMR spectroscopy. In the case of 2VP a conversion of 56.5 % was found after 48 h, which corresponds to a molecular weight of 20.7 kg/mol (NMR spectrum see figure 14.3).

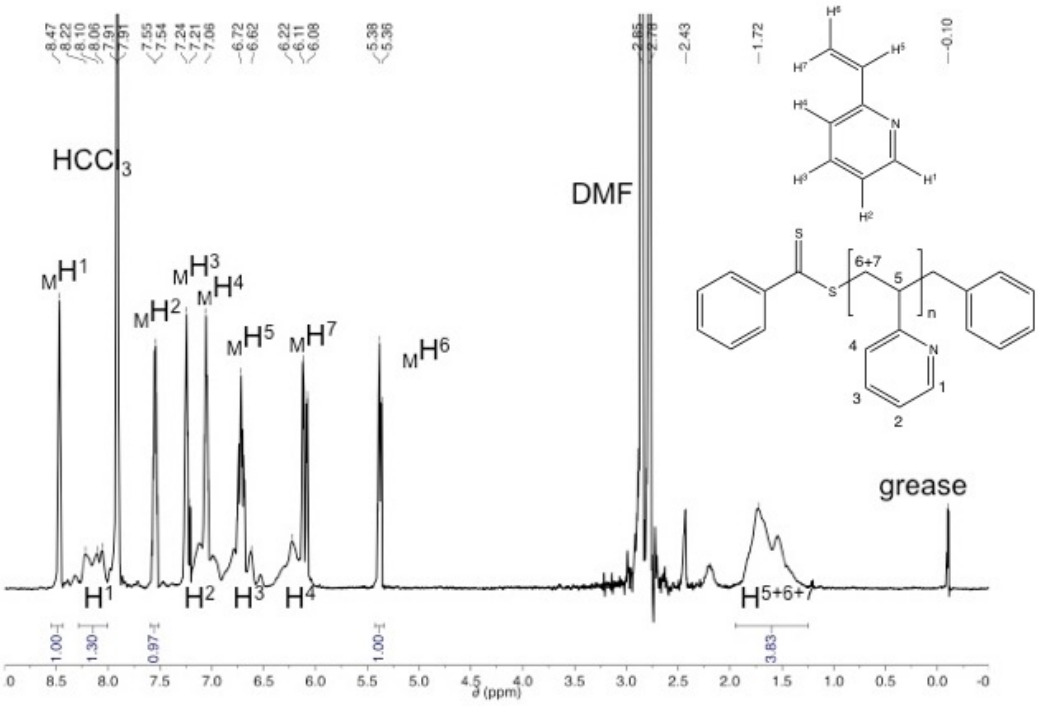

Fig. 14.3: NMR spectrum of the 2VP polymerisation reaction mixture after quenching the reaction to calculate the molecular weight.

To analyse the weight distribution of polymer Gel permeation chromatography (GPC) was conducted. The GPC results of the synthesized P2VP are shown in figure 14.4, showing a PDI of 1.20 for the polymer. This PDI is a good PDI for the use of P2VP as building block for the SLs.

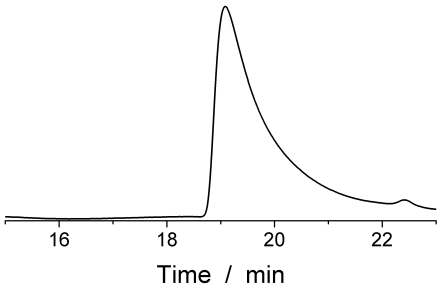

Fig. 14.4: GPC Elugramm of P2VP.

14.2.2 Spin Coating

For the spin coating of P2VP, different solvents were invested. The challenge was to find a solvent polar enough to dissolve P2VP but not too polar to dissolve the underlying nanoparticle layer. A well known good solvent for P2VP is THF, but spin coating of a layer P2VP in THF on a nanoparticle layer did not give a homogeneous layer. Toluene, which is known to be a good solvent for spin coating PMMA was not able to dissolve P2VP. The best result were obtained by using toluene as a solvent and add small amounts of THF for complete dissolution of the polymer. From this solvent mixture it was possible to spin coat well defined SL with a layer thickness of 52 nm and 58 nm for the P2VP and the TiO_2 layer respectively (see figure 14.5a).

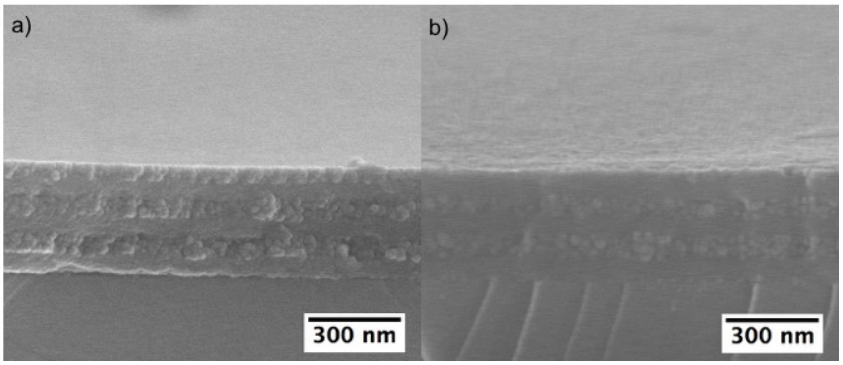

Fig. 14.5: a) Cross-sectional SEM image of a three-layered P2VP-TiO_2 superlattice. b) Cross-sectional SEM image of the same SL after quaternization.

14.2.3 Swelling

After the successful spin coating of the polymer into SLs, the next step was to quaternize and cross-link the amine groups in P2VP and invest the swelling behaviour of the SL. Here, the challenge was to swell the P2VP layer with water vapour, but at the same time, the P2VP layer needed to stay stable in the SL.

For quaternization and cross-linking of the P2VP layer, first, a drop casted P2VP film was quaternized by storing the film in a solution of 1,4-bromobutane and bromoethane in hexane for 48 h at 45 °C. To prove the successful reaction, a IR spectrum of a drop casted film of P2VP and a 70 % quaternized and 30 % cross-linked P2VP film was measured (see figure 14.6). The shift of the band at 1670 cm^{-1} to 1639 cm^{-1} proves that the reaction was successful.

The next step was the quaternization and cross-linking of the P2VP layer in a SL. The same procedure as for the drop casted film was conducted. A cross-sectional SEM image of a three-layered SL before (a) and after the quaternization/cross-linking (b) is shown in figure 14.5. It can be clearly seen that the SL is stable during the treatment in hexane. Even after keeping the SL in hexane for 48 h at 45 °C the lattice spacing stays the same (before: P2VP: 52 nm and TiO_2: 58 nm after: P2VP: 54 nm and TiO_2: 58 nm).

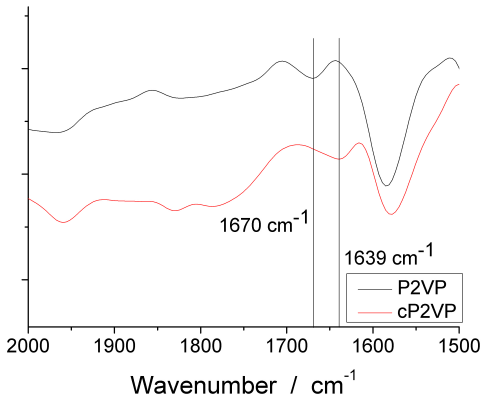

Fig. 14.6: IR spectra of the P2VP (black line) and the 70 % quaternized and 30 % cross-linked P2VP (red line) films.

To confirm the swelling behaviour of the synthesised P2VP in water vapour polymer films with a thickness of around 100 nm were spin coated onto a Si-wafer. The exact thickness of these films was measured using a filmetrics instrument (F20). This device measures the spectral reflectance of the films in comparison to the substrate to determine the film thickness. The thickness of individual P2VP films was measured as well as the thickness of a 70 % quaternized and 30 % cross-linked P2VP film before and after vapour annealing with ethanol and water. The results are given in table 14.1. The results show that the P2VP film does not significantly swell after the deposition of water vapour but swells when annealed in ethanol vapour.

After 20 h of ethanol vapour annealing, the P2VP film starts to disintegrate and an inhomogeneous film remains on the substrate. In case of the 70 % quaternized and 30 % cross-linked P2VP film, no significant swelling after the ethanol vapour annealing can be observed. In contrast to that, the vapour annealing for 2 h with water vapour results in a swelling of the film by 29 nm. The film did not swell further even after being stored for 20 h in water vapour.

Tab. 14.1: Results of the filmetrics measurements after vapour annealing.

Film Thickness	Atmosphere	Time	Thickness
P2VP	-	-	103 nm
	water	2 h	107 nm
		20 h	105 nm
	-	-	100 nm
	ethanol	2 h	127 nm
		20 h	88 nm
qP2VP	-	-	105 nm
	water	2 h	134 nm
		20 h	134 nm
	-	-	122 nm
	ethanol	2 h	127 nm
		20 h	129 nm

14.3 Summary and Outlook

First experiments on P2VP-containing SLs to build a responsive SL were successfully conducted. It could be demonstrated, that films from synthesized P2VP can be swollen in water vapour. Furthermore it was possible to spin coat SL from P2VP and nanoparticles. While Kang *et al.* swelled the PtC by depositing them directly into water, here, it was possible to swell the films by a vapour annealing step. This was an important improvement to us, because the used nanoparticles used to build up the SLs are dissolvable in water and therefore the SLs are not stable in water.

Moreover, it was possible to build up P2VP-containing SLs and a post fabrication modification of the P2VP layer in the SL was successfully preformed. It is possible to carry out a quaternization or cross-linking of the amine group of the P2VP within the SL.

In future experiments, it is needed to test wether the SL is stable in water vapour and wether the photonic and phononic band gap can be shifted by swelling the P2VP layers. One problem, which could arise is that usually the nanoparticle layers are spin coated from water solutions and that this layer might suffer from damage by being exposed to water vapour. It will be crucial to control the moisture for the swelling process very precisely for getting a ideal swelling and keeping the SLs stable at the same time.

Furthermore, the swelling of the P2VP layers in a full SL has to be confirmed. This could be done, by measuring the UV/Vis reflection spectrum of the SL, while exposing it to water vapour. The photonic band gap of the SL is the reflection minimum. If a successful swelling takes place, a bathochromic shift of the photonic band gap is expected to take place.

In addition, an interesting experiment for the future could be to swell the P2VP layer with ionic liquids. This would open the possibility to observe the swelling behaviour of the polymeric layer under the SEM. In that case, it is easier to control wether the SLs are stable or suffer from damage by the solvent. Because the swelling with IL is a non-reversible process, it is less interesting that the swelling with water vapour. Nevertheless, there are some questions remaining that need to be answered before it is possible to reversible swell inorganic organic hybrid SL and therefore build up responsive SLs.

14.4 Experimental Details

14.4.1 Polymer synthesis.

Tab. 14.2: Polymer synthesis

Chemicals	M_W [g/mol]	m [mg]	n [mmol]	eq.	volume
2VP	105.14	5040	47.94	350	5.17 mL
benzyl dithiobenzoate	244.38	39.6	0.137	1	39.6 µL
AIBN	164.21	2.4	0.0146	0.1	
DMF	73.09				5 mL

Before starting the polymerisation AIBN was recrystallised from diethyl ether and the monomer was purified using a cryogenic distillation. For the polymerisation the monomer, the CTA, AIBN and DMF were quickly filled into a schlenk tube and freeze pumped three times. Then vacuum was kept on the schlenk tube and the reaction mixture was transferred into a 80 °C preheated oil bath. After 48 h the schlenk tube was quickly cooled down to room temperature by quenching the tube under water. From the reaction mixture a sample for NMR measurement was taken. After 5 mL of DMF was added to the reaction mixture, it was added trop wise into a mixture of hexane and to precipitate the polymer. Afterwards the polymer was collected by filtration and dried in vacuum for two days. The purity of the polymer was confirmed by NMR spectroscopy.

14.4.2 Spin Coating

A 2.2 wt % solution of P2VP in a mixture of toluene and THF (1 mL of toluene 1 drop of THF) was prepared. And the TiO_2 nanoparticles (synthesis see chapter TiO_2) had a concentration of 60 g/L in 14% NH_3. The same spin coating parameters as usual were used: speed: 5000 rpm, acceleration: 5000 rpm/s, time: 20 s. After each layer the SL was heated to 100 °C for 15 min.

14.4.3 Quaternization and Cross-Linking

Tab. 14.3: Quaternization and cross-linking.

Chemicals	M_W [g/mol]	m [mg]	n [mmol]	eq.	V [µL]
1,4 dibromo butane	215.93	45.2	0.21	0.42	25
bromoethane	108.97	109.5	1.00	1	75
hexane	86.18				900

In a glass char 900 µL of hexane was mixed with 25 µL of 1,4 dibromobutane and 75 µL of bromoethane. The substrate with the polymer film or the SL was put into the glass char and heated to 45 °C for 48 h. Afterwards the substrate was removed from the reaction mixture and dried in the hood for 30 min.

Part IV

Summary & Outlook

15 Summary

The aim of this thesis was to develop and optimize the synthesis of titania and barium titanate nanoparticles to allow control over the morphology of the nano-material and optimize their properties for future applications.

First, the successful synthesis of cubic anatase nanoparticles, which can assemble into mesocrystals, was presented. This enables the fabrication of films with a very high density compared to spheres due to the reduction of void space within the film. Therefore, these cubes are promising candidates as high density layer materials in phononic crystals.

Further, building blocks from barium titanate were synthesised. The influence of oleic acid addition during the synthesis on the solubility as well as the morphology of the resulting particles was studied. It was possible to synthesize ferroelectric barium titanate nanorods and preliminary experiments showed that they could be oriented in an electric field.

Using these inorganic nanoparticles as building blocks, the fabrication and characterization of new hybrid superlattices (SLs) was achieved. First, the fabrication of homogenous inorganic and polymer layers was discussed, including a detailed description of the characterization methods, followed by the presentation of six novel SLs.

With the fabrication of the PMMA-TiO_2 SL, the first experimental realization of a 1D pho(X)onic crystal with a dual photonic and phononic band gap was accomplished. This SL showed a photonic band gap in the wavelength region between 315 and 360 nm and at the same time the widest hypersonic phononic band gap reported so far with a central frequency of 15 GHz.

Further, the geometry of the SL was changed by combining the layers presented above into a tandem SL built up from a SiO_2-PMMA and a $BaTiO_3$-PMMA SL with a defect SiO_2 layer in between the two SLs. Interestingly, this tandem SL exhibits an allowed mode within the photonic band gap. While the phononic behaviour is not fully understood yet, it seems that the SiO_2-PMMA sub-SL acts as a phononic crystal, while the $BaTiO_3$-PMMA sub-SL acts as effective medium.

A higher order of periodicity, was achieved by the fabrication of $(ABAC)_n$ ordered SLs. They showed an interesting photonic behaviour, due to their double periodic structure two band gaps at around 400–500 nm and around 850–1000 nm could be observes.

A detailed description of how to incorporate colloidal SiO_2 particles into a PMMA-SiO_2 SLs was given. The characterization of this SL using Brillouin light scattering

showed, that the expected interaction between the eigenmodes of $cSiO_2$ particles and the phonon propagation of the phononic PMMA-SiO_2 crystal could not be detected.

Finally, first experiments of the fabrication of a responsive SL were described. The swelling behaviour of quaternized P2VP films was promising and the fabrication conditions for three layered SLs was successfully established.

From the synthesis of inorganic building blocks to the fabrication of complex superlattices this work presented to new insights into the behaviour of 1D pho(X)onic crystals. These findings provide a deeper understanding of phononic materials on their way towards applications like sensors or devices for thermal management.

16 Outlook

With a new synthesis of TiO_2 nanocubes and their assembly into an highly ordered film an interesting building block for the formation of new TiO_2 films was established. Due to their functionalization with DHCA the nanoparticles are highly negatively charged, this charge plays an important role in the assembly of the nanocubes. The exact charge of a single nanocube is not known, but could be investigated by for example titration of the acid function. Knowing the exact charge allows to further control the interaction forces between the particles in the assembly. Using nanoindentation, the Young's modulus of the film could be determined to get a better understanding of the properties of the film. Further, the nano-structured film could be investigated using a small-angle scattering technique to determine the degree of order within the film. And finally, the performance of the nanocubes in solar cells could be in interesting topic, since the loss of excitons is known to be caused by the relatively high void space in TiO_2 films from spherical TiO_2 particles which causes an efficiency loss.

Furthermore, an optimization of the synthesis parameters could benefit the morphology control of the $BaTiO_3$ nanorods. A closer control of the size distribution would help to regulate the behaviour of the nanorods within the electric field. The Currie temperature of the nano-material needs to be determined to investigate the behaviour of the nanorods above and below the Currie temperature in the electric field. With such an experiment the origin of the orientation could be determinate The next steps could be the functionalization of the nanorods with polymers and the investigation of their performance as electro-responsive liquid crystals or switches.

The fabrication and characterization of hybrid superlattices built up from PMMA and inorganic oxide nanoparticles opened several questions on the topic of composite materials. Beside the nanoparticles composition, the surface molecules of the particles as well as the nature of the interaction of these surface ligands, the fabrication method and the resulting packing factor of the films influence the sound velocity of films tremendously. A systematic study of the dependance of the sound velocity on the packing factor would be a helpful tool to a facilitate characterisation of SL in the future.

Another open questions remains regarding the SLs containing $BaTiO_3$. The sound velocity and the refractive index measured by Brillouin light scattering for the $BaTiO_3$ layers is extremely low. To confirm the correctness of the BLS measurement the $BaTiO_3$ films should be characterized using a different method for the determination of the sound velocity and the refractive index, e.g. pump-probe spectroscopy. From this technique the phononic characterization of the $(ABAC)_n$ periodic SLs would

benefit as well, because it covers a broader frequency range than the BLS technique and therefore it could be a suitable technique for the detection of phonons within this lattices.

Furthermore, first experiments on the swelling behaviour of P2VP are promising and the further characterization of P2VP containing SLs could lead to interesting applications of 1D phononic crystals as sensors.

Bibliography

[1] S. Berthier, E. Charron, A. Da Silva, „Determination of the cuticle index of the scales of the iridescent butterfly Morpho menelaus“, *Opt. Commun.* **2003**, *228*, 349.

[2] J. Teyssier, S. V. Saenko, D. van der Marel, M. C. Milinkovitch, „Photonic crystals cause active colour change in chameleons“, *Nat. Commun.* **2015**, *6*, 6368.

[3] P. Vukusic, J. R. Sambles, „Photonic structures in biology“, *Nature* **2003**, *424*, 852.

[4] J. D. Joannaopoulos, S. G. Johnson, J. N. Winn, R. D. Made, *Photonic Crystals Molding the Flow of Light*, Princeton, **2008**.

[5] L. D. Bonifacio, B. V. Lotsch, D. P. Puzzo, F. Scotognella, G. Ozin, „Stacking the Nanochemistry Deck: Structural and Compositional Diversity in One-Dimensional Photonic Crystals“, *Adv. Mater.* **2009**, *21*, 1641.

[6] Y. Kang, J. J. Walish, T. Gorishnyy, E. L. Thomas, „Broad-wavelength-range chemically tunable block-copolymer photonic gels.“, *Nat. Mater.* **2007**, *6*, 957.

[7] J. Yoon, W. Lee, J. M. Caruge, et al., „Defect-mode mirrorless lasing in dye-doped organic/inorganic hybrid one-dimensional photonic crystal“, *Appl. Phys. Lett.* **2006**, *88*, 15.

[8] Y.-R. Huang, J. T. Park, J. H. Prosser, J. H. Kim, D. Lee, „Multifunctional all-TiO2 Bragg stacks based on blocking layer-assisted spin coating“, *J. Mater. Chem. C* **2014**, *2*, 3260.

[9] H.-g. Park, C. J. Barrelet, Y. Wu, et al., „A wavelength-selective photonic-crystal waveguide coupled to a nanowire light source“, *Nat. Photonics* **2008**, *2*, 622.

[10] J. J. Wierer, A. David, M. M. Megens, „III-nitride photonic-crystal light-emitting diodes with high extraction efficiency“, *Nat. Photonics* **2009**, *3*, 163.

[11] S. Matsuo, A. Shinya, T. Kakitsuka, et al., „High-speed ultracompact buried heterostructure photonic-crystal laser with 13 fJ of energy consumed per bit transmitted“, *Nat. Photonics* **2010**, *4*, 648.

[12] S. Furumi, „Self-assembled organic and polymer photonic crystals for laser applications“, *Polym. J.* **2012**, *45*, 579.

[13] P. H. M. S. Kushwaha, B. D.-R. L. Dobrzynski, „Acoustic Band Structure of Periodic Elastic Composites“, *Phys. Rev. Lett.* **1993**, *71*, 2022.

[14] M. Sigalas, E. N. Economou, „Band structure of eleastic waves in two dimensional systems“, *Solid State Commun.* **1993**, *86*, 141.

[15] N. Gomopoulos, D. Maschke, C. Y. Koh, et al., „One-dimensional hypersonic phononic crystals.“, *Nano Lett.* **2010**, *10*, 980.

[16] D. Schneider, F. Liaqat, E. H. El Boudouti, et al., „Engineering the hypersonic phononic band gap of hybrid Bragg stacks.“, *Nano Lett.* **2012**, *12*, 3101.

[17] D. Schneider, F. Liaqat, E. H. El Boudouti, et al., „Defect-Controlled Hypersound Propagation in Hybrid Superlattices“, *Phys. Rev. Lett.* **2013**, *111*, 164301.

[18] R. Martinez-Sala, J. Sancho, J. Sanchez, V. Gomez, J. Llinares, „Sound attenuation by sculpture“, *Nature* **1995**, *378*, 241.

[19] Z. Liu, X. Zhang, Y. Mao, et al., „Locally Resonant Sonic Materials“, *Science* **2000**, *289*, 1734.

[20] J.-H. Lee, C. Y. Koh, J. P. Singer, et al., „Ordered Polymer Structures for the Engineering of Photons and Phonons.“, *Adv. Mater.* **2014**, *26*, 532.

[21] M. Maldovan, E. Thomas, „Simultaneous complete elastic and electromagnetic band gaps in periodic structures“, *Appl. Phys. B* **2006**, *83*, 595.

[22] Y. Pennec, B. D. Rouhani, E. H. El Boudouti, et al., „Simultaneous existence of phononic and photonic band gaps in periodic crystal slabs.“, *Opt. Express* **2010**, *18*, 14301.

[23] Y. Pennec, B. D. Rouhani, C. Li, et al., „Band gaps and cavity modes in dual phononic and photonic strip waveguides“, *AIP Adv.* **2011**, *1*, 0419011.

[24] M. Eichenfield, J. Chan, R. M. Camacho, K. J. Vahala, O. Painter, „Optomechanical crystals.“, *Nature* **2009**, *462*, 78.

[25] A. V. Akimov, Y. Tanaka, A. B. Pevtsov, et al., „Hypersonic modulation of light in three-dimensional photonic and phononic band-gap materials“, *Phys. Rev. Lett.* **2008**, *101*, 033902 1.

[26] A. H. Safavi-Naeini, O. Painter, „Design of optomechanical cavities and waveguides on a simultaneous bandgap phononic-photonic crystal slab.“, *Opt. Express* **2010**, *18*, 14926.

[27] A. H. Safavi-Naeini, J. T. Hill, S. Meenehan, et al., „Two-Dimensional Phononic-Photonic Band Gap Optomechanical Crystal Cavity“, *Phys. Rev. Lett.* **2014**, *112*, 153603.

[28] I. Psarobas, N. Papanikolaou, N. Stefanou, et al., „Enhanced acousto-optic interactions in a one-dimensional phoxonic cavity“, *Phys. Rev. B* **2010**, *82*, 1.

[29] G. M. Whitesides, B. Grzybowski, „Self-assembly at all scales.“, *Science* **2002**, *295*, 2418.

[30] L. Bergström, E. V. Sturm (née Rosseeva), G. Salazar-Alvarez, H. Cölfen, „Mesocrystals in biominerals and colloidal arrays“, *Acc. Chem. Res.* **2015**, *48*, 1391.

[31] M. P. Pileni, „Self-assembly of inorganic nanocrystals: Fabrication and collective intrinsic properties“, *Acc. Chem. Res.* **2007**, *40*, 685.

[32] D. V. Talapin, J.-S. Lee, M. V. Kovalenko, E. V. Shevchenko, „Prospects of Colloidal Nanocsrystals for Electronic and Optoelectronic Applications“, *Chem. Rev.* **2010**, *110*, 389.

[33] M. G. Panthani, B. A. Korgel, „Nanocrystals for Electronics“, *Annu. Rev. Chem. Biomol. Eng.* **2012**, *3*, 287.

[34] D. V. Talapin, „Nanocrystal solids: A modular approach to materials design“, *MRS Bull.* **2012**, *37*, 63.

[35] H. M. Jaeger, S. R. Nagel, R. P. Behringer, „The Physics of Granular Materials“, *Phys. Today* **1996**, *4*, 32.

[36] B. M. Quinn, I. Prieto, S. K. Haram, A. J. Bard, „Electrochemical Observation of a Metal / Insulator Transition by Scanning Electrochemical Microscopy“, *J. Phys. Chem. B* **2001**, *105*, 7474.

[37] S. Maier, M. Brongersma, P. Kik, H. Atwater, „Observation of near-field coupling in metal nanoparticle chains using far-field polarization spectroscopy“, *Phys. Rev. B* **2002**, *65*, 1.

[38] J. Fang, B. Ding, H. Gleiter, „Mesocrystals: syntheses in metals and applications.“, *Chem. Soc. Rev.* **2011**, *40*, 5347.

[39] M. Graetzel, R. A. J. Janssen, D. B. Mitzi, E. H. Sargent, „Materials interface engineering for solution-processed photovoltaics.“, *Nature* **2012**, *488*, 304.

[40] D. B. Mitzi, M. Yuan, W. Liu, et al., „Hydrazine-based deposition route for device-quality CIGS films“, *Thin Solid Films* **2009**, *517*, 2158.

[41] F. Liaqat, M. N. Tahir, H. Huesmann, et al., „Ultrastrong composites from dopamine modified-polymer-infiltrated colloidal crystals“, *Mater. Horiz.* **2015**, *2*, 434.

[42] F. Natalio, T. P. Corrales, M. Panthöfer, et al., „Flexible Minerals: Self-Assembled Calcite Spicules with Extreme Bending Strength“, *Science* **2013**, *339*, 1298.

[43] L. Zhou, D. Smyth-boyle, P. O. Brien, „A Facile Synthesis of Uniform NH4 TiOF3 Mesocrystals and Their Conversion to TiO2 Mesocrystals“, *J. Am. Chem. Soc.* **2008**, *130*, 1309.

[44] C. Desvaux, C. Amiens, P. Fejes, et al., „Multimillimetre-large superlattices of air-stable iron–cobalt nanoparticles“, *Nat. Mater.* **2005**, *4*, 750.

[45] A. Ahniyaz, Y. Sakamoto, L. Bergström, „Magnetic field-induced assembly of oriented superlattices from maghemite nanocubes.“, *Proc. Natl. Acad. Sci. U. S. A.* **2007**, *104*, 17570.

[46] J. Zhang, Z. Luo, B. Martens, et al., „Reversible Kirkwood Alder Transition Observed in Pt 3 Cu 2 Nanoctahedron Assemblies under Controlled Solvent Annealing/ Drying Conditions“, *J. Am. Chem. Soc.* **2012**, *134*, 14043.

[47] N. V. Dziomkina, G. J. Vancso, „Colloidal crystal assembly on topologically patterned templates“, *Soft Matter* **2005**, *1*, 265.

[48] H. Cölfen, M. Antonietti, *Mesocrystals and Nonclassical Crystallization*, John Wiley & Sons, **2008**.

[49] S.-J. Liu, J.-Y. Gong, B. Hu, S.-H. Yu, „Mesocrystals of Rutile TiO2: Mesoscale Transformation, Crystallization, and Growth by a Biologic Molecules-Assisted Hydrothermal Process“, *Cryst. Growth Des.* **2009**, *9*, 203.

[50] D. Zhang, G. Li, F. Wang, J. C. Yu, „Green synthesis of a self-assembled rutile mesocrystalline photocatalyst“, *CrystEngComm* **2010**, *12*, 1759.

[51] J. Ye, W. Liu, J. Cai, et al., „Nanoporous anatase TiO2 mesocrystals: Additive-free synthesis, remarkable crystalline-phase stability, and improved lithium insertion behavior“, *J. Am. Chem. Soc.* **2011**, *133*, 933.

[52] P. Tartaj, „Sub-100 nm TiO2 mesocrystalline assemblies with mesopores: preparation, characterization, enzyme immobilization and photocatalytic properties.“, *Chem. Commun. (Camb).* **2011**, *47*, 256.

[53] J. Cai, J. Ye, S. Chen, et al., „Antireflective structures based on mesocrystalline rutile TiO2 nanorod arrays“, *Struct. Chem.* **2012**, 1.

[54] Z. Bian, T. Tachikawa, T. Majima, „Superstructure of TiO2 crystalline nanoparticles yields effective conduction pathways for photogenerated charges“, *J. Phys. Chem. Lett.* **2012**, *3*, 1422.

[55] Q. Chen, W. Ma, C. Chen, H. Ji, J. Zhao, „Anatase TiO2 mesocrystals enclosed by (001) and (101) facets: Synergistic effects between Ti3+ and facets for their photocatalytic performance“, *Chem. - A Eur. J.* **2012**, *18*, 12584.

[56] L. Zhou, J. Chen, C. Ji, L. Zhou, P. O'Brien, „A Facile Solid Phase Reaction to Prepare TiO2 Mesocrystals with Exposed {001} Facets and High Photocatalytic Activity“, *CrystEngComm* **2013**, *15*, 5012.

[57] X. Chen, S. Shen, L. Guo, S. S. Mao, „Semiconductor-based Photocatalytic Hydrogen Generation.“, *Chem. Rev.* **2010**, *110*, 6503.

[58] M. Gratzel, „Photoelectrochemical cells“, *Nature* **2001**, *414*, 338.

[59] Z. Yang, J. Zhang, M. C. W. Kintner-meyer, et al., „Electrochemical energy storage for green grid“, *Chem. Rev.* **2011**, *111*, 3577.

[60] T. Tachikawa, M. Fujitsuka, T. Majima, „Mechanistic insight into the TiO2 photocatalytic reactions: Design of new photocatalysts“, *J. Phys. Chem. C* **2007**, *111*, 5259.

[61] J. P. Gonzalez-Vazquez, V. Morales-Florez, J. A. Anta, „How important is working with an ordered electrode to improve the charge collection efficiency in nanostructured solar cells?“, *J. Phys. Chem. Lett.* **2012**, *3*, 386.

[62] Y. Park, W. Kim, D. Monllor-Satoca, et al., „Role of interparticle charge transfers in agglomerated photocatalyst nanoparticles: Demonstration in aqueous suspension of dye-sensitized TiO2“, *J. Phys. Chem. Lett.* **2013**, *4*, 189.

[63] S. Tirosh, T. Dittrich, A. Ofir, L. Grinis, A. Zaban, „Influence of ordering in porous TiO2 layers on electron diffusion“, *J. Phys. Chem. B* **2006**, *110*, 16165.

[64] S. D. Burnside, V. Shklover, C. Barbe, et al., „Self-Organization of TiO2 Nanoparticles in Thin Films“, *Chem. Mater.* **1998**, *10*, 2419.

[65] L. Liu, X. Gu, Z. Ji, et al., „Anion-assisted synthesis of TiO2 nanocrystals with tunable crystal forms and crystal facets and their photocatalytic redox activities in organic reactions“, *J. Phys. Chem. C* **2013**, *117*, 18578.

[66] N. Roy, Y. Park, Y. Sohn, K. T. Leung, D. Pradhan, „Green Synthesis of Anatase TiO2 Nanocrystals with Diverse Shapes and their Exposed Facets-Dependent Photoredox Activity“, *ACS Appl. Mater. Interfaces* **2014**, *6*, 16468.

[67] C. G. Pierpont, „Studies on charge distribution and valence tautomerism in transition metal complexes of catecholate and semiquinonate ligands“, *Coord. Chem. Rev.* **2001**, *216-217*, 99.

[68] H. C. Choi, Y. M. Jung, S. B. Kim, „Size effects in the Raman spectra of TiO2 nanoparticles“, *Vib. Spectrosc.* **2005**, *37*, 33.

[69] F. Liaqat, M. N. Tahir, E. Schechtel, et al., „High-Performance TiO2 Nanoparticle/ DOPA- Polymer Composites“, *Macromol. Rapid Commun.* **2015**, *36*, 1129.

[70] R. F. Howe, M Gratzel, „EPR study of hydrated anatase under UV irradiation“, *J. Phys. Chem.* **1987**, *91*, 3906.

[71] N. D. Abazović, M. I. Comor, M. D. Dramićanin, et al., „Photoluminescence of anatase and rutile TiO2 particles.“, *J. Phys. Chem. B* **2006**, *110*, 25366.

[72] B. Santara, P. K. Giri, K. Imakita, M. Fujii, „Evidence of oxygen vacancy induced room temperature ferromagnetism in solvothermally synthesized undoped TiO2 nanoribbons.“, *Nanoscale* **2013**, *5*, 5476.

[73] A. Coelho, Topas Academic, Brisbane, **2007**.

[74] R. W. Cheary, A. Coelho, „Fundamental parameters approach to x-ray line-profile fitting“, *J. Appl. Crystallogr.* **1992**, *25*, 109.

[75] K. Yoshida, T. Kawai, T. Nambara, et al., „Direct observation of oxygen atoms in rutile titanium dioxide by spherical aberration corrected high-resolution transmission electron microscopy“, *Nanotechnology* **2006**, *17*, 3944.

[76] C. Xu, K. Xu, H. Gu, et al., „Dopamine as a robust anchor to immobilize functional molecules on the iron oxide shell of magnetic nanoparticles“, *J. Am. Chem. Soc.* **2004**, *126*, 9938.

[77] M. N. Tahir, P. Theato, P. Oberle, et al., „Facile Synthesis and Characterization of Functionalized , Monocrystalline Rutile TiO2 Nanorods“, *Langmuir* **2006**, *22*, 5209.

[78] F. Scotognella, D. P. Puzzo, A. Monguzzi, et al., „Nanoparticle one-dimensional photonic-crystal dye laser“, *Small* **2009**, *5*, 2048.

[79] E. Alonso-Redondo, H. Huesmann, E.-H. El Boudouti, et al., „Phoxonic Hybrid Superlattice.“, *ACS Appl. Mater. Interfaces* **2015**, *7*, 12488.

[80] W. Kossel, „Zur Energetik von Oberflächenvorgängen“, *Ann. Phys.* **1934**, *21*, 457.

[81] J. W. Mullin, *Crystallization*, Butterworth Heinemann, 4th, **2001**.

[82] F. X. Redl, C. T. Black, G. C. Papaefthymiou, et al., „Magnetic, electronic, and structural characterization of nonstoichiometric iron oxides at the nanoscale“, *J. Am. Chem. Soc.* **2004**, *126*, 14583.

[83] C. Lausser, D. Zahn, H. Cölfen, „Barium titanate nanoparticie self-organization in an external electric field“, *J. Mater. Chem.* **2011**, *21*, 16978.

[84] A. Yella, M. N. Tahir, S. Meuer, et al., „Synthesis, characterization, and hierarchical organization of tungsten oxide nanorods: Spreading driven by Marangoni flow“, *J. Am. Chem. Soc.* **2009**, *131*, 17566.

[85] Y. Min, M. Akbulut, K. Kristiansen, Y. Golan, J. Israelachvili, „The role of interparticle and external forces in nanoparticle assembly.“, *Nat. Mater.* **2008**, *7*, 527.

[86] L. Huang, Z. Jia, I. Kymissis, S. O'Brien, „High K Capacitors and OFET Gate Dielectrics from Self-Assembled BaTiO3 and (Ba,Sr)TiO3 Nanocrystals in the Superparaelectric Limit“, *Adv. Funct. Mater.* **2010**, *20*, 554.

[87] J. Li, J. Claude, L. E. Norena-franco, S. I. Seok, Q. Wang, „Electrical Energy Storage in Ferroelectric Polymer Nanocomposites Containing Surface-Functionalized BaTiO3 Nanoparticles“, *Chem. Mater.* **2008**, *20*, 6304.

[88] M. R. Darla, S. Hegde, S. Varghese, „Effect of BaTiO3 Nanoparticle on Electro-Optical Properties of Polymer Dispersed Liquid Crystal Displays“, *J. Cryst. Process Technol.* **2014**, *4*, 60.

[89] M. Wöhlecke, V. Marrello, a. Onton, „Refractive index of BaTiO3 and SrTiO3 films“, *J. Appl. Phys.* **1977**, *48*, 1748.

[90] R. Ashiri, A. Nemati, M. Sasani Ghamsari, S. Sanjabi, M. Aalipour, „A modified method for barium titanate nanoparticles synthesis“, *Mater. Res. Bull.* **2011**, *46*, 2291.

[91] S. O. Brien, L. Brus, C. B. Murray, „Synthesis of Monodisperse Nanoparticles of Barium Titanate: Toward a Generalized Strategy of Oxide Nanoparticle Synthesis“, *J. Am. Chem. Soc.* **2001**, *123*, 12085.

[92] M. Niederberger, G. Garnweitner, N. Pinna, M. Antonietti, „Nonaqueous and halide-free route to crystalline BaTiO3, SrTiO3, and (Ba,Sr)TiO3 nanoparticles via a mechanism involving C-C bond formation.“, *J. Am. Chem. Soc.* **2004**, *126*, 9120.

[93] S. Ohara, A. Kondo, H. Shimoda, et al., „Rapid mechanochemical synthesis of fine barium titanate nanoparticles“, *Mater. Lett.* **2008**, *62*, 2957.

[94] H.-W. Lee, S. Moon, C.-H. Choi, D. K. Kim, „Synthesis and Size Control of Tetragonal Barium Titanate Nanopowders by Facile Solvothermal Method“, *J. Am. Ceram. Soc.* **2012**, *95*, (Ed.: S.-J. Kang), 2429.

[95] E. K. Nyutu, C.-H. Chen, P. K. Dutta, S. L. Suib, „Effect of Microwave Frequency on Hydrothermal Synthesis of Nanocrystalline Tetragonal Barium Titanate“, *J. Phys. Chem. C* **2008**, *112*, 9659.

[96] M. Inada, N. Enomoto, K. Hayashi, J. Hojo, S. Komarneni, „Facile synthesis of nanorods of tetragonal barium titanate using ethylene glycol“, *Ceram. Int.* **2015**, *41*, 5581.

[97] B. S. J. Limmer, S. Seraji, Y. Wu, et al., „Template-Based Growth of Various Oxide Nanorods by Sol-Gel Electrophoresis“, *Adv. Funct. Mater.* **2002**, *12*, 59.

[98] J. H. Wei, J. Shi, Z. Y. Liu, J. B. Wang, „Polymer-assisted synthesis of BaTiO3 nanorods“, *J. Mater. Sci.* **2006**, *41*, 3127.

[99] S. Zhang, F. Jiang, G. Qu, C. Lin, „Synthesis of single-crystalline perovskite barium titanate nanorods by a combined route based on sol–gel and surfactant-templated methods“, *Mater. Lett.* **2008**, *62*, 2225.

[100] J. J. Urban, W. S. Yun, Q. Gu, H. Park, „Synthesis of single-crystalline perovskite nanorods composed of barium titanate and strontium titanate.“, *J. Am. Chem. Soc.* **2002**, *124*, 1186.

[101] D. Caruntu, T. Rostamzadeh, T. Costanzo, S. Salemizadeh Parizi, G. Caruntu, „Solvothermal Synthesis and Controlled Self-Assembly of Monodisperse Titanium-Based Perovskite Colloidal Nanocrystals“, *Nanoscale* **2015**, 12955.

[102] B. Hou, Z. Li, Y. Xu, D. Wu, Y. Sun, „Solvothermal Synthesis of Single-crystalline BaTiO3 Nanocubes in a Mixed Solution“, *Chem. Lett.* **2005**, *34*, 1040.

[103] Q. Liu, Z. Yan, G. Sun, W. Zheng, „Solvothermal Preparation and Characterization of Barium Titanate Nanocubes“, *Chem. Lett.* **2007**, *36*, 458.

[104] T. Yan, Z.-G. Shen, J.-F. Chen, et al., „Synthesis of Well-isolated Barium Titanium Trioxide Nanocubes“, *Chem. Lett.* **2005**, *34*, 1196.

[105] K. Mimura, K. Kato, H. Imai, et al., „Piezoresponse properties of orderly assemblies of BaTiO3 and SrTiO3 nanocube single crystals“, *Appl. Phys. Lett.* **2012**, *101*, 012901.

[106] S. Wada, A. Nozawa, M. Ohno, et al., „Preparation of barium titanate nanocube particles by solvothermal method and their characterization“, *J. Mater. Sci.* **2009**, *44*, 5161.

[107] C. Bogicevic, G. Thorner, F. Karolak, P. Haghi-Ashtiani, J.-M. Kiat, „Morphogenesis mechanisms in the solvothermal synthesis of BaTiO3 from titanate nanorods and nanotubes.“, *Nanoscale* **2015**, *7*, 3594.

[108] C. Lausser, D. Zahn, H. Cölfen, „Barium titanate nanoparticle self-organization in an external electric field“, *J. Mater. Chem.* **2011**, *21*, 16978.

[109] T. Fischer, „Synthese von Bariumtitanatnanostäbchen und Ausrichtung der Stäbchen im elektrischen Feld Bachelorarbeit“, *Bachelorarbeit* **2015**.

[110] F. C. Krebs, „Fabrication and processing of polymer solar cells: A review of printing and coating techniques“, *Sol. Energy Mater. Sol. Cells* **2009**, *93*, 394.

[111] M. E. Calvo, O. Sanchez-Sobrado, S. Colodrero, H. Miguez, „Control over the Structual an Optical Features of Nanoparticle-Based One-Dimensional Photonic Crystals“, *Langmuir* **2009**, 2443.

[112] D. G. Maschke, „A New Class of Bragg Stacks and Its Principle Application“, *PhD Thesis* **2010**.

[113] F. Iskandar, „Nanoparticle processing for optical applications - A review“, *Adv. Powder Technol.* **2009**, *20*, 283.

[114] C. J. Lawrence, „The mechanics of spin coating of polymer films“, *Phys. Fluids* **1988**, *31*, 2786.

[115] A. Münch, C. P. Please, B. Wagner, „Spin coating of an evaporating polymer solution“, *Phys. Fluids* **2011**, *23*, 10.

[116] Y. Mouhamad, P. Mokarian-Tabari, N. Clarke, R. a. L. Jones, M. Geoghegan, „Dynamics of polymer film formation during spin coating“, *J. Appl. Phys.* **2014**, *116*, 123513.

[117] P. Jiang, M. J. McFarland, „Large-scale fabrication of wafer-size colloidal crystals, macroporous polymers and nanocomposites by spin-coating“, *J. Am. Chem. Soc.* **2004**, *126*, 13778.

[118] W. W. Flack, D. S. Soong, A. T. Bell, D. W. Hess, „Mathematical Model for Spin Coating of Polymer Resists.“, *J. Appl. Phys.* **1984**, *56*, 1199.

[119] C. Sanchez, C. Boissière, D. Grosso, C. Laberty, L. Nicole, „Design, Synthesis, and Properties of Inorganic and Hybrid Thin Films Having Periodically Organized Nanoporosity“, *Chem. Mater.* **2008**, *20*, 682.

[120] T. Still, „High frequency acoustics in colloid-based meso- and nanostructures by spontaneous Brillouin light scattering“, *PhD Thesis* **2009**.

[121] D Schneider, „Hypersonic phonon propagation in mesoscopic systems by Brillouin spectroscopy“, *PhD Thesis* **2013**.

[122] D. L. Vezie, E. L. Thomas, W. Adams, „Low-voltage, high-resolution scanning electron microscopy: a new characterization technique for polymer morphology“, *Polymer (Guildf).* **1995**, *36*, 1761.

[123] J. H. Butler, D. C. Joy, G. F. Bradley, S. J. Krause, „Low-voltage scanning electron microscopy of polymers“, *Polymer (Guildf).* **1995**, *36*, 1781.

[124] R. Lucklum, M. Ke, M. Zubtsov, „Two-dimensional phononic crystal sensor based on a cavity mode“, *Sensors Actuators B Chem.* **2012**, *171-172*, 271.

[125] I. Savic, D. Donadio, F. Gygi, G. Galli, I. Savic, „Dimensionality and heat transport in Si-Ge superlattices“, *Appl. Phys. Lett.* **2013**, *102*, 073113.

[126] A. Z. C. W. Chang, D. Okawa, Majumdar, „Solid-State Thermal Rectifier“, *Science* **2006**, *314*, 1121.

[127] M. Maldovan, „Sound and heat revolutions in phononics.“, *Nature* **2013**, *503*, 209.

[128] A. Urbas, R. Sharp, Y. Fink, et al., „Tunable Block Copolymer / Homopolymer Photonic Crystals“, *Adv. Mater.* **2000**, 812.

[129] V. A. Piunova, G. M. Miyake, C. S. Daeffler, R. a. Weitekamp, R. H. Grubbs, „Highly ordered dielectric mirrors via the self-assembly of dendronized block copolymers“, *J. Am. Chem. Soc.* **2013**, *135*, 15609.

[130] P. M. Walker, J. S. Sharp, a. V. Akimov, a. J. Kent, „Coherent elastic waves in a one-dimensional polymer hypersonic crystal“, *Appl. Phys. Lett.* **2010**, *97*, 91.

[131] T. Ogata, R. Yagi, N. Nakamura, Y. Kuwahara, S. Kurihara, „Modulation of polymer refractive indices with diamond nanoparticles for metal-free multilayer film mirrors“, *ACS Appl. Mater. Interfaces* **2012**, *4*, 3769.

[132] S. Narayanan, J. Choi, L. Porter, M. R. Bockstaller, „Flexible transparent metal/polymer composite materials based on optical resonant laminate structures“, *ACS Appl. Mater. Interfaces* **2013**, *5*, 4093.

[133] L. C. Parsons, G. T. Andrews, „Off-axis phonon and photon propagation in porous silicon superlattices studied by Brillouin spectroscopy and optical reflectance“, *J. Appl. Phys.* **2014**, *116*, 033510.

[134] M Trigo, A. Bruchhausen, A. Fainstein, B. Jusserand, V. Thierry-Mieg, „Confinement of acoustical vibrations in a semiconductor planar phonon cavity.“, *Phys. Rev. Lett.* **2002**, *89*, 227402.

[135] H. J. Trodahl, P. V. Santos, G. V. M. Williams, A. Bittar, „Raman scattering from surface and bulk acoustic phonons in capped superlattices“, *Phys. Rev. B* **1989**, *40*, 8577.

[136] N.-W. Pu, J. Bokor, „Study of surface and bulk acoustic phonon excitations in superlattices using picosecond ultrasonics.“, *Phys. Rev. Lett.* **2003**, *91*, 076101.

[137] M. Trigo, T. A. Eckhause, M. Reason, R. S. Goldman, R. Merlin, „Observation of surface-avoiding waves: A new class of extended states in periodic media“, *Phys. Rev. Lett.* **2006**, *97*, 1.

[138] C. G. Hou, V. L. Zhang, H. S. Lim, et al., „Band structures of surface acoustic waves in nanostructured phononic crystals with defects“, *Appl. Phys. Lett.* **2014**, *105*, 243104.

[139] G. Saini, „Pulsed laser characterization of multicomponent polymer acoustic and mechanical properties in the sub-GHz regime“, *J. Mater. Res.* **2007**, *22*, 719.

[140] W. Cheng, R. Sainidou, P. Burgardt, et al., „Elastic Properties and Glass Transition of Supported Polymer Thin Films“, *Society* **2007**, *40*, 7283.

[141] N. Gomopoulos, W. Cheng, M. Efremov, P. F. Nealey, G. Fytas, „Out-of-plane longitudinal elastic modulus of supported polymer thin films“, *Macromolecules* **2009**, *42*, 7164.

[142] R. S. Bandhu, X. Zhang, R. Sooryakumar, K. Bussmann, „Acoustic vibrations in free-standing double layer membranes“, *Phys. Rev. B - Condens. Matter Mater. Phys.* **2004**, *70*, 1.

[143] B. D. Rouhani, J. Sapriel, „Effective dielectric and photoelastic tensors of superlattices in the long-wavelength regime“, *Phys. Rev. B* **1986**, *34*, 7114.

[144] M. Chirita, R. Sooryakumar, R. Venugopal, J. Wan, M. Melloch, „Acoustic barriers and observation of guided elastic waves in GaN-AlN structures by Brillouin scattering“, *Phys. Rev. B* **2001**, *63*, 1.

[145] B. Hillebrands, S. Lee, G. I. Stegeman, et al., „Evidence for the existence of guided longitudinal acoustic phonons in ZnSe films on GaAs“, *Phys. Rev. Lett.* **1988**, *60*, 832.

[146] A. B. Wood, *A Textbook of Sound*, Neil & Co., Edinburgh U.K., **1930**.

[147] J. Cuffe, E. Chávez, A. Shchepetov, et al., „Phonons in slow motion: Dispersion relations in ultrathin Si membranes“, *Nano Lett.* **2012**, *12*, 3569.

[148] P. Yeh, *Optical Waves in Layered Media*, WILEY-VCH GmbH, New York, 2ed, **2005**.

[149] R. D. Joannopoulos, J. D.; Johnson, S. G.; Winn, J. N.; Meade, *Photonic Crystals: Molding the Flow of Light*, Princeton University Press, Princeton, NJ, **2008**.

[150] N. Papanikolaou, I. E. Psarobas, N. Stefanou, et al., „Light modulation in phoxonic nanocavities“, *Microelectron. Eng.* **2012**, *90*, 155.

[151] A. Martínez, „Phoxonic Crystals: Tailoring the Light-Sound Interaction at the Nanoscale“, *Proc. SPIE* **2013**, *No. 8632OW*, 8632.

[152] M. C. George, A. Mohraz, M. Piech, et al., „Direct laser writing of photoresponsive colloids for microscale patterning of 3D porous structures“, *Adv. Mater.* **2009**, *21*, 66.

[153] A. Ayouch, X. Dieudonne, G. Vaudel, et al., „Elasticity of an assembly of disordered nanoparticles interacting via either Van der Waals-bonded or covalent-bonded coating layers“, *ACS Nano* **2012**, *6*, 10614.

[154] T. Goto, a. Dorofeenko, a. Merzlikin, et al., „Optical Tamm States in One-Dimensional Magnetophotonic Structures“, *Phys. Rev. Lett.* **2008**, *101*, 113902.

[155] I. Quotane, E. H. El Boudouti, B. Djafari-Rouhani, Y. El Hassouani, V. R. Velasco, „Bulk and surface acoustic waves in solid-fluid Fibonacci layered materials“, *Ultrasonics* **2015**, *61*, 40.

[156] P. Ruello, V. E. Gusev, „Physical mechanisms of coherent acoustic phonons generation by ultrafast laser action“, *Ultrasonics* **2015**, *56*, 21.

[157] T Still, M Mattarelli, D Kiefer, G Fytas, M Montagna, „Eigenvibrations of Submicrometer Colloidal Spheres“, *J. Phys. Chem. Lett.* **2010**, *1*, 2440.

[158] W. Stöber, A. Fink, „Controlled growth of monodisperse silica spheres in the micron size range“, *J. Colloid Interface Sci.* **1968**, *26*, 62.

[159] A. Noro, Y. Tomita, Y. Shinohara, et al., „Photonic Block Copolymer Films Swollen with an Ionic Liquid“, *Macromolecules* **2014**, *47*, 4103.

[160] M. Zamfir, C. S. Patrickios, F. Montagne, et al., „Styrene-vinyl pyridine diblock copolymers: Synthesis by RAFT polymerization and self-assembly in solution and in the bulk“, *J. Polym. Sci. Part A Polym. Chem.* **2012**, *50*, 1636.

List of Figures

1.1 a) One, b) two and c) thee dimensional PtC 3
1.2 Images of the male *Morpho menelaus* butterfly 4
1.3 Photo of a Marine poychaete worm *Aphrodita*. 4
1.4 Image of the male panther chameleon in the relaxed state and the excited state. 5

2.1 a) SEM image of 1D PnC built from PMMA-SiO_2 SL. b) Phonon dispersion relation of that PnC.[16] 7
2.2 a) Photo of the kinematic sculpture by Eusebio Sempre. b) Sound attenuation vs. sound frequency diagram of the kinematic sculpture.[18] 8
2.3 a) Cross-sectional image of a coated lead sphere. b) Sonic crystal formed from assembly of 8x8x8 spheres. c) Calculated (solid line) and measured (circles) amplitude transmission coefficient for the PnC and d) its calculated band structure.[19] 8

3.1 Unit cell of the snowflake PnC. 11

5.1 Characterization of the anatase nanocubes. 21
5.2 TiO_2 particles synthesized at a TMAOH concentration of a) 5 %; b) 10 %; c) 20 %; d) 25 % (inserts: size distribution). 22
5.3 TEM micrographs of anatase nanocrystals autoclaved at (a) 170, (b) 195, and (c) 225 °C in aqueous solution containing 15 wt% of TMAOH. Size distributions are shown in the insets. 23
5.4 TEM images of the TiO_2 nanoparticles synthesized in methanolic TMAOH, insert size distribution. 24
5.5 Self-assembled oriented superlattice from anatase nanocubes. 25
5.6 Raman spectrum of the self-assembled anatase nanocube superlattice. 28
5.7 UV-Vis spectra of the DHCA functionalized nanocubes (black line) and non-functionalized particles (red line), and photographs of the DHCA functionalized nanocubes (left) and non-functionalized particles (right). 28
5.8 Photoluminescence spectrum of the nanocubes with an excitation wavelength of 365 nm. 29
5.9 X-ray diffractogram of the TiO_2 nanocubes. 29
5.10 Zeta potential of the nanocubes as a function of the pH. 30
5.11 SEM image of the assembled nanocube film. 30
5.12 Defects of growing nanocube mesocrystal after Kossel's model. 31

6.1 TEM image of spherical $BaTiO_3$ particles in different magnification. . 35
6.2 X-ray diffraction pattern of $BaTiO_3$ nanospheres. 35

6.3 A laser microscope image (A) and a TEM image of the $BaTiO_3$ nanorods. 37
6.4 TEM images of the $BaTiO_3$ nanorods 37
6.5 Systematic scheme of the electrical cell. 39
6.6 Light microscope image of the $BaTiO_3$ nanorods in the electric cell while an electric field is applied. 39
6.7 SEM image of the oriented nanorods (top view). 40
6.8 EDX of the $BaTiO_3$ nanorods. 42

7.1 Schematic image of the rotating unit of a spin coater. 45
7.2 Molecular structure of 3,4-dihydroxy hydrocinnamic acid. 48
7.3 Scheme of 3,4-dihydroxy hydrocinnamic acid at the surface of nanoparticles. 49
7.4 Cross-sectional SEM image of a 10 BL PMMA-$BaTiO_3$ SL containing satellites. 49

8.1 A systematic image of the BLS process. 51
8.2 Scheme of the experimental setup of the BLS experiment.[121] 52
8.3 The two different scattering geometries used for BLS measurements. . 53
8.4 SEM sample preparation. 54
8.5 Cros-sectionalSEM images of a PMMA-$BaTiO_3$ SL. 55
8.6 Systematic sketch of the Gemini column. 56
8.7 Photo of the 75°-tiled sample holder for cross-sectional SEM imaging. 56

9.1 a) Cross-sectional SEM micrograph of the 10-bilayer PMMA-TiO_2 superlattice. b) Schematic of the SL. The two cavity defects are noted as c_1 and c_2. 60
9.2 a) Cross-sectional SEM image of the TiO_2-infiltrated film. b) Linear (acoustic) dispersion, frequency vs wave vector, for the longitudinal phonon in the TiO_2-infiltrated film, TiO_2-drop casted and PMMA. . . 60
9.3 BLS spectra recorded parallel to the substrate (normal to the periodicity) at three wave vectors $q_{\parallel}$ as indicated in the plot. 62
9.4 BLS spectra recorded perpendicular to the substrate (parallel to the periodicity) at three wave vectors $q_{\perp}$ and Dispersion relation for phonon propagation along the two orthogonal directions. 63
9.5 Theoretical dispersion relation of an infinite SL. 64
9.6 a) UV/vis spectrum of the ten bilayer PMMA/TiO_2 SL, b) Calculated band structure of the infinite SL. 66
9.7 TEM Image of the TiO_2 nanoparticles used for spin coating the SL. . 69
9.8 Sound velocity of TiO_2-PMMA blends as a function of the TiO_2 weight fraction. 71
9.9 SEM image of the TiO_2 PMMA blend with a TiO_2 weight fraction of 0.3. 71
9.10 SEM image of the TiO_2 PMMA blend with a TiO_2 weight fraction of 0.7. 71

10.1 a) Cross-sectional SEM images of the PMMA-$BaTiO_3$ SL A, b) UV/Vis absorption of the PMMA-$BaTiO_3$ SL A. 74
10.2 Dispersion relation of the PMMA-$BaTiO_3$ SL A. 75

10.3 Cross-sectional SEM images and UV/Vis absorption of the PMMA-$BaTiO_3$ SL B. 75
10.4 Dispersion relation of the PMMA-$BaTiO_3$ SL B. 76
10.5 Phase velocity ($2\pi f/q$) as a function of q, the dispersion of the modes in plane is revealed. 77
10.6 Characterization of a $BaTiO_3$ film. 78
10.7 Blot of the sound velocity vs. volume fraction of the PMMA-$BaTiO_3$ blends. 79

11.1 Systematic image of an $(AB)_5A(CB)_5$ tandem superlattice. 81
11.2 Cross-sectional SEM images of the tandem SL. 82
11.3 Experimental UV/Vis absorption (red line) and transmission (blue line) spectra and simulated transmission spectrum (black line) of the tandem SL. 83
11.4 Cross-sectional SEM images of the tandem SL with the spatial localization of the mode at 493.56 nm (black line). 84
11.5 Calculated transmission spectra and dispersion curves of the two sub-SLs. 84
11.6 Phonon dispersion of the tandem SL. 85
11.7 BLS spetra of the tandem-SL 87

12.1 Systematic image of an $(ABAC)_n$ superlattice (purple: PMMA, blue and yellow: inorganic nanoparticles). 89
12.2 Cross-sectional SEM images of the three $(ABAC)_n$ SLs. 91
12.3 UV/Vis absorption and transmission spectra of a) SLI, b) SLII, c) SLIII 92
12.4 The experimental and calculated UV/Vis absorption and transmission spectra of SLI. 93
12.5 Calculated transmission spectra of the SL I with 20 repeating units. (b) Calculated dispersion curve of an infinite SL I. (c) Dispersion curves of infinite PMMA-SiO_2 (blue), PMMA-TiO_2 (red) and a SiO_2-TiO_2 (green) SLs. 93

13.1 Schematic sketch of the SL with a $cSiO_2$ defect layer. 97
13.2 TEM image of $cSiO_2$ particles. 98
13.3 Cross-sectional SEM image of a 3 BL PMMA-SiO_2 SL with a $cSiO_2$ defect layer. 99
13.4 Cross-sectional SEM images of PMMA-SiO_2-PMMA-$cSiO_2$-(PMMA-SiO_2)$_2$ SLs with different amounts of PMMA in the $cSiO_2$ layer. . . . 100
13.5 Cross-sectional SEM images of PMMA-SiO_2-PMMA-$cSiO_2$-(PMMA-SiO_2)$_2$ SLs with different $cSiO_2$:SiO_2 weight ratios. 100
13.6 Cross-sectional SEM images of (PMMA-SiO_2)$_4$-PMMA-$cSiO_2$-(PMMA-SiO_2)$_4$ SL. 101
13.7 Experimental dispersion relation (squares) acquired in plane (white area) and out of plane (blue area). 102
13.8 BLS spectra acquired in plane (a) and out of plane (b). 104

14.1 Scheme of the reaction mechanism of the RAFT polymerisation. . . . 106
14.2 Reaction scheme of P2VP synthesis. 106

14.3 NMR spectrum of the 2VP polymerisation reaction mixture after quenching the reaction to calculate the molecular weight. 107
14.4 GPC Elugramm of P2VP. 107
14.5 a) Cross-sectional SEM image of a three-layered P2VP-TiO_2 superlattice. b) Cross-sectional SEM image of the same SL after quaternization. 108
14.6 IR spectra of the P2VP (black line) and the 70 % quaternized and 30 % cross-linked P2VP (red line) films. 109

List of Tables

7.1 Nanoparticle concentrations used for a layer thickness of about 50 nm. 50

9.1 Physical quantities of the 10-Bilayer PMMA-TiO_2 superlattice constituents and substrate used in the theoretical calculations. 61

9.2 Mixing protocol for the fabrication of the TiO_2 PMMA blends (* a 2.2 wt% PMMA solution in ACN was used). 72

11.1 Refractive indices and layer thickness ($*$ values used in the theoretical calculation). 82

12.1 Lattice parameter for SL I-III and the refractive indices of the layer material, the values in brackets are being used for the calculation. . . 90

13.1 Preparation protocol of the different $cSiO_2$ solutions. 104

14.1 Results of the filmetrics measurements after vapour annealing. 110

14.2 Polymer synthesis 112

14.3 Quaternization and cross-linking. 112

List of acronyms

AAO Anodic Aluminium Oxide

AFM Atom Force Microscopy

BE Backscattered Electrons

BL Bilayer

BG Band Gap

BLS Brillouin Light Scattering

DHCA Dihydro 3,4-Dihydroxycinnamic Acid

DOS Density of States

EPR Electron Paramagnetic Resonance

FEA Finite Element Analysis

FEG Field Emission Gun

FCC Face-centered cubic

FPI Fabry-Perot Interferometer

GPC Gel Permeation Chromatography

IR Infrared

LVSEM Low Voltage Scanning Electron Microscopy

NMR Nuclear Magnetic Resonance

NC Nanocubes

NP Nanoparticle

P2VP poly(2-vinyl pyridine)

PDI Polydispersity Index

PL Photoluminescence

PnC Phononic Crystal

PS Polysytrene

PtBG Photonic Band Gap

PtC Photonic Crystal

PXC Pho(X)onic Crystal

SC Spin coating

SDS sodium dodecyl sulfate

SE Secondary Electrons

SEM Scanning Electron Microscopy

SL Superlattice

TMAOH Tetramethylammonium Hydroxide

TEM Tunnelling Electron Microscopy

UV Ultra Violett